12-14-2018

Finite Nuclei in Covariant Density Functional Theory: A Global View with an Assessment of Theoretical Uncertainties

Sylvester E. Agbemava

Finite nuclei in covariant density functional theory:

a global view with an assessment of theoretical uncertainties.

By

Sylvester E. Agbemava

A Dissertation
Submitted to the Faculty of
Mississippi State University
in Partial Fulfillment of the Requirements
for the Degree of Doctor of Philosophy
in Engineering Physics
in the Department of Physics and Astronomy

Mississippi State, Mississippi

December 2018

Finite nuclei in covariant density functional theory:

a global view with an assessment of theoretical uncertainties.

By

Sylvester E. Agbemava

Approved:

Anatoli Afanasjev
(Major Professor)

Dipangkar Dutta
(Committee Member)

Gautam Rupak Lan Tai Moong
(Committee Member)

Jeffry A. Winger
(Committee Member)

Yaroslav Koshka
(Committee Member)

Hendrik F. Arnoldus
(Graduate Coordinator)

Jason M. Keith
Dean
Bagley College of Engineering

Name: Sylvester E. Agbemava

Date of Degree: December 14, 2018

Institution: Mississippi State University

Major Field: Engineering Physics

Major Professor: Anatoli Afanasjev

Title of Study: Finite nuclei in covariant density functional theory: a global view with an assessment of theoretical uncertainties.

Pages of Study: 192

Candidate for Degree of Doctor of Philosophy

Covariant density functional theory (CDFT) is a modern theoretical tool for the description of nuclear structure phenomena. Different physical observables of the ground and excited states in even-even nuclei have been studied within the CDFT framework employing three major classes of the state-of-the-art covariant energy density functionals. The global assessment of the accuracy of the description of the ground state properties and systematic theoretical uncertainties of atomic nuclei have been investigated. Large-scale axial relativistic Hartree-Bogoliubov (RHB) calculations are performed for all $Z \leq 106$ even-even nuclei between the two-proton and two-neutron drip lines. The sources of theoretical uncertainties in the prediction of the two-neutron drip line are analyzed in the framework of CDFT. We concentrate on single-particle and pairing properties as potential sources of these uncertainties. The major source of these uncertainties can be traced back to the differences in the underlying single-particle structure of the various CEDFs. A systematic search for axial octupole deformation in the actinides and superheavy nuclei

with proton numbers $Z = 88 - 126$ and neutron numbers from two-proton drip line up to $N = 210$ has been performed in CDFT. The nuclei in the $Z \sim 96, N \sim 196$ region of octupole deformation have been investigated in detail and their systematic uncertainties have been quantified. The structure of superheavy nuclei has been reanalyzed with inclusion of quadrupole deformation. Theoretical uncertainties in the predictions of inner fission barrier heights in superheavy elements have been investigated in a systematic way. The correlations between global description of the ground state properties and nuclear matter properties have been studied. It was concluded that the strict enforcement of the constraints on the nuclear matter properties (NMP) defined in Ref. [1] will not necessary lead to the functionals with good description of ground state properties. The different aspects of the existence and stability of hyperheavy nuclei have been investigated. For the first time, we demonstrate the existence of three regions of spherical hyperheavy nuclei centered around ($Z \sim 138, N \sim 230$), ($Z \sim 156, N \sim 310$) and ($Z \sim 174, N \sim 410$) which are expected to be reasonably stable against spontaneous fission.

Key words: covariant density functional theory, drip lines, triaxiality, octupole deformation, superheavy elements, hyperheavy elements, fission barriers, theoretical uncertainties

DEDICATION

This work is dedicated to my parents, David Agbemava and Vida Acquah, who have loved me unconditionally and also taught me the value of education.

ACKNOWLEDGEMENTS

Completion of this doctoral dissertation was possible with the support of several people. First and foremost I wish to thank my advisor, Prof. Anatoli Afanasjev. I appreciate all his contributions of time, ideas and the provision of research assistantship for the entire duration of my Ph.D. programme. This help make my Ph.D. experience productive and stimulating. On a personal level, Prof. Afanasjev inspired me by his hardworking and passionate attitude. To summarize, I could not have imagined having a better advisor and mentor for my Ph.D. study. My sincere thanks also goes to my dissertation committee members (Prof. Dipangkar Dutta, Prof. Jeffry Winger, Prof. Gautam Rupak and Prof. Yaroslav Koshka) for their great support and invaluable advice. I thank Prof. Peter Ring (Technical University of Munich, Germany) and Prof. Takashi Nakatsukasa (Center for Computational Sciences, University of Tsukuba) for their valuable suggestions and concise comments on some of the research papers of this dissertation. I would like also to acknowledge past and present group members that I have had the pleasure to work with or alongside of (Dr. Debisree Ray, Dr. Hazem Abusara, Abhinaya Gyawali, Ahmad Taninah and Saja Teeti).

I would like to thank my family for all their love and encouragement. I owe a lot to my parents, who encouraged and helped me at every stage of my personal and academic life. Their support has been unconditional all these years; they have given up many things for me

to be who I am today. I also thank my brother (Cornelius Agbemavah) and sisters (Fidelia and Dzigbordi Agbemavah) for supporting me both spiritually and physically throughout these years. And most of all for my loving, supportive, encouraging, and patient wife Irene Assan and my son Elikem Abeiku Agbemava. Thank you.

I must thank all the Department of Physics and Astronomy Professors, staff and colleagues whom I have worked with over the last six years for showing me what it means to be dedicated, each in their own unique way. To my friend Kofi Tutu Assumin-Gyimah, thank you for listening, offering me advice and supporting me through this entire process. Special thanks to my friends: Daniel Odei Okyere and Samuel Agyei Sefa.

I also extend my thankfulness towards all the funding agencies which include but are not limited to Department of Energy (DOE), National Nuclear Security Administration (NNSA) and the Department of Physics and Astronomy (for Teaching Assisstant).

Above all, I owe it all to the Almighty God for granting me the wisdom, health and strength to undertake this research task and enabling me to its completion.

TABLE OF CONTENTS

DEDICATION ii

ACKNOWLEDGEMENTS iii

LIST OF TABLES viii

LIST OF FIGURES ix

LIST OF SYMBOLS xiii

CHAPTER

I. INTRODUCTION 1

1.1 Purpose of this work 4
1.2 Dissertation outline 4

II. FORMALISM: THE ENERGY DENSITY FUNCTIONAL 7

2.1 Basic features of covariant density functional theory 7
2.2 Covariant Energy Density Functionals 8
2.2.1 Meson-exchange model 8
2.2.2 Point coupling model 14
2.2.3 The fitting protocols 15
2.3 Pairing correlation 16
2.4 The effective pairing interaction 19

III. GLOBAL PERFORMANCE OF COVARIANT ENERGY DENSITY FUNCTIONALS: GROUND STATE OBSERVABLES OF EVEN-EVEN NUCLEI AND THE ESTIMATE OF SYSTEMATIC THEORETICAL UNCERTAINTIES 23

3.1 Introduction 23
3.2 Details of numerical calculation 25
3.3 Binding energies 28

3.4 Separation energies . . . 34
3.5 Two-proton drip line. . . . 37
3.6 Two-neutron drip line. . . . 41
3.7 Deformations . . . 47
3.8 Charge radii and neutron skin thickness. . . . 52
3.9 Concluding remarks. . . . 60

IV. NEUTRON DRIP LINE: SINGLE-PARTICLE DEGREES OF FREEDOM AND PAIRING PROPERTIES AS SOURCES OF THEORETICAL UNCERTAINTIES . . . 64

4.1 Introduction . . . 64
4.2 Pairing properties: a global view . . . 66
4.3 The impact of pairing properties on the position of two-neutron drip line using Rn isotopes as an example . . . 70
4.4 Shell structure and single-particle energies at the two-neutron drip line. . . . 73
4.5 Concluding remarks . . . 77

V. OCTUPOLE DEFORMATION IN THE GROUND STATES OF EVEN-EVEN NUCLEI: A GLOBAL ANALYSIS WITHIN THE COVARIANT DENSITY FUNCTIONAL THEORY . . . 79

5.1 Introduction . . . 79
5.2 Details of the theoretical calculations . . . 81
5.3 Octupole deformation in actinides . . . 84
5.3.1 Discussion: theory versus experiment for Ra isotopes . . . 85
5.4 Octupole deformation in lanthanides . . . 90
5.4.1 Ba isotopes. . . . 90
5.5 Octupole deformation in superheavy region . . . 91
5.6 Global analysis . . . 99
5.7 Concluding remarks . . . 101

VI. SUPERHEAVY NUCLEI: GROUND STATE PROPERTIES AND FISSION BARRIERS . . . 105

6.1 Introduction . . . 105
6.2 Numerical details . . . 106
6.3 The impact of deformation on the properties of superheavy nuclei 109
6.4 The systematics of the deformations . . . 111
6.5 Masses and separation energies . . . 115
6.6 α-decay properties . . . 116
6.7 Fission barriers of superheavy nuclei . . . 121

6.7.1 Global investigation of inner fission barriers and related systematic theoretical uncertainties in the axial RHB calculations 121
6.7.2 Systematic theoretical uncertainties in the description of inner fission barriers for triaxial RHB calculations 124
6.8 Concluding remarks 129

VII. COVARIANT ENERGY DENSITY FUNCTIONALS: NUCLEAR MATTER CONSTRAINTS 131

7.1 Introduction 131
7.2 Brief outline of the details of theoretical framework 133
7.3 The impact of nuclear matter properties of the functionals on the predictions of binding energies of known and neutron-rich nuclei . 134
7.4 Concluding remarks 139

VIII. HYPERHEAVY NUCLEI: EXISTENCE AND STABILITY 142

8.1 Introduction 142
8.2 Axial calculations: general structure of potential energy surfaces. 144
8.3 Triaxial calculations: the drop of stability via triaxial plane. . . . 153
8.4 Metastable spherical shapes: fission barriers and their dependence on the functionals. 160
8.5 Concluding remarks 164

IX. CONCLUSIONS 167

REFERENCES 171

LIST OF TABLES

2.1 The parameters of NL3*, DD-ME2 and DD-MEδ CEDF's. 13

2.2 The parameters of the DD-PC1 CEDF 15

3.1 The rms deviations $\Delta E_{\rm rms}$, $\Delta(S_{2n})_{\rm rms}$, and $\Delta(S_{2p})_{\rm rms}$. 28

3.2 Properties of symmetric nuclear matter at saturation for the EDFs used in Fig.3.9. 45

3.3 Two-proton and two-neutron drip lines. 46

3.4 The rms-deviations $\Delta r_{ch}^{\rm rms}$ between calculated and experimental charge radii. 55

3.5 Neutron skin thicknesses $r_{\rm skin}$ in ^{48}Ca and ^{208}Pb obtained in calculations with the indicated CEDF's. 57

5.1 Calculated effect of reflection asymmetry on nuclear ground state properties. 94

6.1 rms-deviations $\Delta E_{\rm rms}$, $\Delta(S_{2n})_{\rm rms}$ and $\Delta(S_{2p})_{\rm rms}$ between calculated and experimental data. 117

6.2 Same as Table 6.1 but for $\Delta(Q_\alpha)_{rms}$ and $\Delta(\tau_\alpha)_{rms}$. In the last column, the deviations are given in terms of orders of magnitude. 122

7.1 Input data for fitting protocols of different CEDFs. 135

7.2 Properties of symmetric nuclear matter at saturation. 139

8.1 The heights of the fission barriers along the fission paths from different minima obtained in axial and triaxial RHB calculations. 159

LIST OF FIGURES

2.1 The nuclei (solid squares) used in the fit of indicated CDFT parametrizations. 16

3.1 The difference between theoretical and experimental masses. 29

3.2 The same as in Fig. 3.1 but with DD-MEδ. 30

3.3 The same as in Fig. 3.1 but with DD-PC1. 30

3.4 The binding energy spreads $\Delta E(Z,N)$ as a function of proton and neutron number. 33

3.5 Two-neutron separation energies $S_{2n}(Z,N)$ given for different isotopic chains as a function of neutron number. 34

3.6 Two-proton separation energies $S_{2p}(Z,N)$ given for different isotonic chains as a function of proton number. 35

3.7 The calculated two-proton drip lines versus experimental data. 37

3.8 The comparison of the uncertainties in the definition of two-proton and two-neutron drip lines obtained in CDFT and SDFT. 40

3.9 Two-neutron drip-lines obtained in state-of-the-art DFT calculations. The regions of well defined localization of the two-neutron drip-line are encircled. 41

3.10 The same as in Fig. 3.9 but with the four most neutron-rich two-neutron drip lines shown in color and the rest in black. 42

3.11 Charge quadrupole deformations β_2 obtained in the RHB calculations with DD-PC1. 49

3.12 Proton quadrupole deformation spreads $\Delta\beta_2(Z,N)$ as a function of proton and neutron number. 51

3.13 Experimental and theoretical charge radii as a function of neutron number. 53

3.14 Charge radii spread $\Delta r_{\rm ch}(Z,N)$ as a function of proton and neutron number. 56

3.15 Neutron skin thicknesses obtained in RHB calculations with DD-PC1. . . . 58

3.16 Neutron skin thickness spreads $\Delta r_{\rm skin}(Z,N)$ as a function of proton and neutron number. 60

4.1 The uncertainties in the location of the two-proton and two-neutron drip lines. 65

4.2 Neutron pairing energies $E_{\rm pairing}$ obtained in the RHB calculations with DD-PC1 CEDF. 66

4.3 Neutron pairing gaps $\Delta_{\rm uv}$ and pairing energies $E_{\rm pairing}$ of Yb nuclei. 68

4.4 The evolution of the λ_n, β_2, $\Delta_{\rm uv}$ and $E_{\rm pairing}$ 70

4.5 Neutron single-particle states at spherical shape in the indicated nuclei. . . 76

4.6 Neutron shell gaps $\Delta E_{\rm gap}$ for the nuclei under study. 77

5.1 Potential energy surfaces of the ^{218}Ra isotopes in the (β_2,β_3) plane calculated with the CEDF DD-PC1. 86

5.2 The same as in Fig. 5.1 but for ^{224}Ra. 87

5.3 The same as in Fig. 5.1 but for ^{230}Ra. 87

5.4 The calculated equilibrium β_2 and β_3 deformations as well as the ΔE^{oct} quantities for Ra isotope chain. 88

5.5 The same as in Fig. 5.4 but for Ba isotope chain. 89

5.6 Octupole deformed nuclei in the nuclear chart. Only nuclei with non vanishing ΔE^{oct} are shown by squares. 101

5.7 The same as in Fig. 5.6 but for NL3* CDFT. 102

5.8 The same as in Fig. 5.6 but for $Z = 88 - 110$ with DD-ME2 CDFT. 102

5.9 The same as in Fig. 5.8 but with PC-PK1 CDFT, and the dash line represent the neutron drip line for NL3*. 103

6.1 Deformation energy curves for the chain of $Z = 120$ isotopes obtained in axial RHB calculations. 108

6.2 Charge quadrupole deformations β_2 obtained with PC-PK1 CEDF. 112

6.3 Same as Fig. 6.2 but with DD-PC1 CEDF. 113

6.4 Proton quadrupole deformation spreads $\Delta\beta_2$ as a function of proton and neutron number. 114

6.5 The comparison of experimental and calculated Q_α values for even-even superheavy nuclei. 118

6.6 Experimental and calculated half-lives for α-decays of even-even superheavy nuclei. 119

6.7 The heights of inner fission barriers (in MeV) with DD-ME2 CEDF. 121

6.8 Same as Fig. 6.7 but with DD-MEδ CEDF. 122

6.9 The spreads ΔE^B of the heights of inner fission barriers as a function of proton and neutron number. 124

6.10 Potential energy surfaces of the $^{300}120$ nucleus as obtained in the calculations with indicated CEDFs. 126

6.11 The spreads ΔE^S of the energies of axial saddles for a selected set of the $Z = 112 - 120$ nuclei as a function of proton and neutron number. 127

6.12 Same as Fig .6.11 but for TRHB calculations. 127

7.1 The binding energy spread $\Delta E(Z, N)$ as a function of proton and neutron number. 135

7.2 Binding energy spreads $\Delta E(Z, N)$ for the pairs of indicated functionals. . 140

8.1 Deformation energy curves of ^{208}Pb and selected even-even hyperheavy nuclei. 145

8.2 Neutron density distributions at the local minimum with $\beta_2 = 2.30, \beta_4 = +1.5, \gamma = 60^\circ$ in the $^{354}134$ nucleus. 148

8.3 The same as Fig. 8.2 but for the local minimum with $\beta_2 = 2.50, \beta_4 = -4.4, \gamma = 60^\circ$. 149

8.4 Neutron density distributions of the $^{466}156$ nucleus. 150

8.5 Charge quadrupole deformations β_2 of the lowest in energy particle bound minima obtained in axial RHB calculations. 152

8.6 Potential energy surfaces (PES) of indicated nuclei obtained in the RHB calculations. 156

8.7 Potential energy surfaces of the $^{354}134$ nucleus obtained in the RMF+BCS calculations. 159

8.8 The heights of the fission barriers [in MeV] around spherical states. 166

LIST OF SYMBOLS

Following are the technical abbreviations and special nomenclature used in this dissertation.

CDFT Covariant Density Functional Theory

CEDF Covariant Energy Density functional

CRMF Cranked Relativistic Mean Field

DFT Density Functional Theory

EDF Energy Density Functional

LEMAS Lowest in energy minima for axial symmetry

MM microscopic+macroscopic

NMP nuclear matter property

PES Potential Energy Surface

RHB relativistic Hartree-Bogoliubov

SDFT Skyrme Density Functional Theory

SHE Super Heavy Element

rms root-mean-square

TRHB Triaxial relativistic Hartree-Bogoliubov

CHAPTER I

INTRODUCTION

Atomic nuclei are self-bound systems with translational invariance. Their constituents (protons and neutrons) have spin and isospin degrees of freedom which play an important role in the nucleon-nucleon interaction. At present, the physics of unstable nuclei is at the forefront of low energy nuclei physics research. Significant experimental and theoretical efforts are focused on this direction.

There are a lot of theoretical approaches for solving the nuclear many- body problem such as the *ab-initio* no-core shell model [14] for very light nuclei, the shell model approach [15] for light to medium mass nuclei and many others. All these models have limitations with respect to the region of the nuclear chart where they can be deployed. The density functional theory is the only theoretical framework which at present can be applied to the entire nuclear chart.

Density functional theories (DFT) are built on a series of theorems by Kohn and Sham [16, 17]. Using these theories the properties of many-body systems can be determined by solving a system of equations characteristic of independent particle system. It has been applied with great success for many years in Coulombic systems [16, 17], where they are, in principle, exact and where the functional can be derived without any phenomenologi-

cal adjustments directly from the Coulomb interaction. This approach was later extended to nuclear physics [18]. Nuclear DFT is a reformulation of the traditional self-consistent mean-field theory of nuclear structure. Although the exact form of the energy density functional for nuclear systems is not known, phenomenological energy functionals have been built by fitting the parameters to experimental data, and they have been very successful in the reproduction of the properties of finite nuclei.

Among the nuclear DFTs, the relativistic variant of DFT namely, covariant density functional theory (CDFT) is one of the most attractive. This is because it exploits the properties of quantum chromodynamics (QCD) at low energies, such as symmetries and the separation of scales [19]. It has been employed as widely as the the non-relativistic DFT in the studies of nuclear structure. The CDFT provides a consistent treatment of the spin degrees of freedom, it includes the complicated interplay between the large Lorentz scalar and vector self-energies induced on the QCD level by the in-medium changes of the scalar and vector quark condensates [20]. The time-odd components of the mean field are entirely fixed by the Lorentz covariance, while the counterparts in the non-relativistic models have significant ambiguities in their definition [21].

At present, all attempts to derive these functionals directly from the bare forces [22, 23, 24, 25] do not reach the required accuracy. Recently, modern phenomenological covariant density functionals have been derived [26, 27, 28] which provide an excellent description of ground and excited states all over the nuclear chart [29, 30] with a high predictive power. Modern versions of these forces derive the density dependence of the vertices from state-

of-the-art ab-initio calculations and use only the remaining few parameters for a fine tuning of experimental masses in finite spherical [28] or deformed [27] nuclei.

Every physical object in macroworld can be described by its size, color, shape and many other physical attributes associated with it. Similarly, every atomic nucleus is uniquely defined by its mass, radius, deformation etc. These properties provide important information about the internal structure of the nucleus and the forces which form it.

Significant amount of experimental data exist on the properties of stable and radioactive nuclei in the ground state or/and at low excitation energies. The masses, charge radii, and decay modes etc, have been studied extensively for a large number of isotopes and are, in general, well known near the β-stability line. As we move away from the stability line towards the borderline of known nuclei, our experimental information becomes scarce. This has made it difficult or impossible to predict the exact limits of stability. Nuclear masses contain basic information about nuclear structure, and with data on masses we are able to calculate separation energies and Q-values for the calculation of α-decay, half-lives etc. These data will help in the determination of the so called r-process path. But because of the problem of extrapolation to nuclei with large isospin, many of nuclei with larger Z and N values will never be studied experimentally.

In the region of heavy and superheavy nuclei, various decay modes co-exist, such as the α-decay, β-decays, and spontaneous fission. Fission is a process in which a nucleus splits in two or sometimes three or more fragments, its mechanism is very complicated Nuclear fission is the main reason for the instability of heavy nuclei due to the Coulomb

repulsive force. This implies that a better understanding of the fission mechanism will lead to a more precise definition of the limits on the existence of nuclei with a high-Z number.

Considerable progress in the experimental synthesis of heaviest nuclei has been achieved. The heaviest superheavy element (SHE) identified has proton number $Z = 118$ [31, 32] and dedicated experimental facilities such as the Dubna Superheavy Element Factory will hopefully allow to extend the region of SHEs up to $Z = 120$ and for a wider range of neutron numbers at lower Z values.

The stability of superheavy elements is defined by the fission barriers. Also, the experimental studies of SHEs are only based on the observation of α-decays and as a result only SHEs with spontaneous fission half-lives τ_{SF} longer than the half-lives τ_α of the α-decays could be observed in experiment. It must be also noted that only α-decays longer than 10 μs can be observed in experiment. Therefore, it is of great importance to study the fission barriers in SHEs.

1.1 Purpose of this work

The aims of this work are: (i) to investigate ground state properties (masses, deformations, neutron skins, charge radii etc) of finite nuclei on a global scale and (ii) to study fission barriers on superheavy nuclei and their systematic theoretical uncertainties using the current generations of the covariant energy density functionals (CEDFs).

1.2 Dissertation outline

This dissertation is organized as follows:

- In Chapter 2, I present the basic features of the covariant density functional theory (CDFT). The second part of this chapter is dedicated to the explanation of the state-of-the-art covariant energy density functionals (CEDF) used in this dissertation.

- In Chapter 3, the global description of the ground state observables for $Z \leq 106$ even-even nuclei is presented. The aim of this project is to assess the accuracy of the description of the ground state properties of even-even nuclei and to evaluate the theoretical uncertainties in the description of physical observables in known regions of the nuclear chart and their propagation towards the neutron drip line. The results for binding energies, separation energies, charge quadrupole deformations, charge radii, neutron skin thicknesses and the positions of the two-proton and two-neutron drip lines will be shown. The theoretical uncertainties discussed in this chapter are the systematic uncertainties which emerge from the underlying theoretical approximations about the form of the functional.

- Chapter 4 is devoted to the effects of single-particle energies and the pairing properties on the position of the two-neutron drip line. The first part of this chapter is dedicated to the question of the impact of pairing and its strength on the two-neutron drip line. The second part of this chapter deals with the shell structure and single-particle energies at the two-neutron drip line.

- Chapter 5 discusses the octupole deformation in the ground states of even-even nuclei. A global survey of octupole deformed and octupole soft nuclei in the CEDF framework across the full nuclear landscape and the analysis of related theoretical

uncertainties have been performed. For the first time, this chapter also compares octupole deformations in the actinides and lanthanides with experimental results.

- The impact of deformation on the properties of superheavy nuclei and in addition the fission barriers of superheavy nuclei are analysed in chapter 6. This chapter reanalyzes the structure of superheavy nuclei using both the full set of available experimental data on SHEs and the new generation of energy density functionals. The first part of this chapter is devoted to the accuracy of the description of known SHEs with the new generation of covariant energy density functionals. It also addresses the question on whether existing experimental data allows to distinguish the predictions of different functionals for nuclei beyond the known region of SHEs. The second part is dedicated to the evaluation of systematic theoretical uncertainties in the regions of SHEs located beyond the presently known region.

- Chapter 7 is devoted to the impact of nuclear matter properties of the functionals on the predictions of binding energies of known and neutron-rich nuclei.

- The study of the existence and stability of nuclei with $Z \geq 126$ (hyperheavy nuclei) is presented in chapter 8.

- Finally, chapter 9 summarizes the main results obtained in this work.

CHAPTER II

FORMALISM: THE ENERGY DENSITY FUNCTIONAL

2.1 Basic features of covariant density functional theory

Theoretical approaches based on covariant density functional theory (CDFT) remain undoubtedly among the most successful for the descriptions of nuclear structure. The CDFT approaches are obtained from a Lorentz invariant density functional which connects in a consistent way the spin and spatial degrees of freedom in the nucleus. In CDFT a nucleus is described as a system of Dirac nucleons interacting via the exchange of effective mesons with finite masses leading to a finite range interaction. Three classes of covariant density functional models have been used in this dissertation. These are the nonlinear meson-nucleon coupling model (NL), the density-dependent meson-exchange model (DD-ME) and the density-dependent point-coupling model (DD-PC). The main differences between them are in the treatment of the range of the interaction, the mesons and the density dependence of the interaction. The interaction in the first two classes has a finite range that is determined by the mass of the mesons. For fixed density it is of Yukawa type and the range is given by the inverse of the meson masses. For large meson masses, i.e. for small ranges, the meson propagator can be expanded in terms of this range. In zeroth order we obtain δ-forces and higher order derivative terms. This leads to the third class of density functionals, the point coupling models. There is no meson in this type of model, therefore

the interaction is of zero-range. The density dependence is explicit in the last two models. They are taken into account by density dependent meson-nucleon vertices in the DD-ME and DD-PC models. In nonlinear meson nucleon coupling model the density dependence is introduced through the powers of the σ-meson. Each of these classes is represented by the energy density functionals considered to be state-of-the-art. They are NL3* [33] for the NL-models, DD-ME2 [26] and DD-MEδ [28] for the DD-ME models, and by DD-PC1 [27] for the point coupling models. The DD-MEδ model is different from the DD-ME2 by the presence of an extra (δ) meson in the DD-MEδ model.

2.2 Covariant Energy Density Functionals

2.2.1 Meson-exchange model

The nucleus is described in meson-exchange models [33, 26, 28], as a system of Dirac nucleons interacting via the exchange of mesons with finite masses leading to finite-range interactions. The starting point of covariant density functional theory (CDFT) for these two models is a standard Lagrangian density [34]

$$\begin{aligned}\mathcal{L} = & \bar{\psi}\left[\gamma\cdot(i\partial - g_\omega\omega - g_\rho\vec{\rho}\,\vec{\tau} - eA) - m - g_\sigma\sigma - g_\delta\vec{\tau}\vec{\delta}\right]\psi \\ & + \frac{1}{2}(\partial\sigma)^2 - \frac{1}{2}m_\sigma^2\sigma^2 + \frac{1}{2}(\partial\vec{\delta})^2 - \frac{1}{2}m_\delta^2\vec{\delta}^2 \\ & - \frac{1}{4}\Omega_{\mu\nu}\Omega^{\mu\nu} + \frac{1}{2}m_\omega^2\omega^2 - \frac{1}{4}\vec{R}_{\mu\nu}\vec{R}^{\mu\nu} + \frac{1}{2}m_\rho^2\vec{\rho}^2 \\ & - \frac{1}{4}F_{\mu\nu}F^{\mu\nu}\end{aligned} \tag{2.1}$$

which contains nucleons described by the Dirac spinors ψ with the mass m and several effective mesons characterized by the quantum numbers of spin, parity, and isospin. They create effective fields in a Dirac equation, which corresponds to the Kohn-Sham equa-

tion [16] of non-relativistic density functional theory. The Lagrangian (2.1) contains as parameters the meson masses m_σ, m_ω, m_δ, and m_ρ and the coupling constants g_σ, g_ω, g_δ, and g_ρ. e is the charge of the protons and it vanishes for neutrons. This linear model has first been introduced by Walecka [35, 36]. However, it was realized that this simple model failed to describe the surface properties of realistic nuclei. Especially, the resulting incompressibility of infinite nuclear matter is much too large [37] and nuclear deformations are too small [34]. An effective density dependence was introduced by Boguta and Bodmer [37] by replacing the term $\frac{1}{2}m_\sigma^2\sigma^2$ in Eq. (2.1) with the quartic potential

$$U(\sigma) \;=\; \frac{1}{2}m_\sigma^2\sigma^2 + \frac{1}{3}g_2\sigma^3 + \frac{1}{4}g_3\sigma^4. \tag{2.2}$$

The nonlinear meson-coupling models are represented by the parameter set NL3* [33] (see Table 2.1), which is a modern version of the widely used parameter set NL3 [38]. Both contain no δ-meson. Apart from the fixed values for the masses m, m_ω and m_ρ, there are six phenomenological parameters m_σ, g_σ, g_ω, g_ρ, g_2, and g_3 which have been fitted in Ref. [33] to a set of experimental data in spherical nuclei: 12 binding energies, 9 charge radii, and 4 neutron skin thicknesses.

The density-dependent meson-nucleon coupling model has an explicit density dependence for the meson-nucleon vertices. There are no non-linear terms for the σ meson, i.e. $g_2 = g_3 = 0$. For the form of the density dependence the Typel-Wolter ansatz [39] has been used:

$$g_i(\rho) = g_i(\rho_{\rm sat})f_i(x) \quad \text{for} \quad i = \sigma, \omega, \delta, \rho \tag{2.3}$$

where the density dependence is given by [39, 26, 28]

$$f_i(x) = a_i \frac{1 + b_i(x + d_i)^2}{1 + c_i(x + e_i)^2}. \tag{2.4}$$

$x = \rho/\rho_{\rm sat}$, ρ and $\rho_{\rm sat}$ are the baryonic density at a specific location and the baryonic density at saturation in symmetric nuclear matter, respectively. The eight real parameters in Eq. (2.4) are not independent, but constrained as follows: $f_i(x = 1) = 1$, $f_\sigma''(x = 1) = f_\omega''(x = 1)$, and $f_i''(x = 0) = 0$. In addition, the following constraints $d_\sigma = e_\sigma$ and $d_\omega = e_\omega$ are used. This reduces the number of independent parameters for the density dependence. The density-dependent meson-nucleon coupling model is represented by the CEDF's DD-ME2 [26] and DD-MEδ [28]. DD-MEδ is selected in order to understand the role of the extra (δ) meson in this model. In the case of DE-ME2 we have no δ-meson and the density dependence of Eq. (2.4) is used only for the σ and ω mesons. For the ρ meson we have an exponential density dependence

$$f_\rho(x) = \exp(-a_\rho(x - 1)) \tag{2.5}$$

in DD-ME2.

The parameters of the NL3*, DD-ME2 and DD-MEδ CEDF's are tabulated in the Table 2.1 . The masses are given in MeV and the dimension of g_2 in NL3* is fm^{-1}. All other parameters are dimensionless. Note that $g_\sigma = g_\sigma(\rho_{\rm sat})$, $g_\omega = g_\omega(\rho_{\rm sat})$, $g_\delta = g_\delta(\rho_{\rm sat})$ and $g_\rho = g_\rho(\rho_{\rm sat})$ in the case of the DD-ME2 and DD-MEδ CEDF's.

The major difference between the functional NL3* and other functionals considered in this work is related to the fact that NL3* has no non-linearities in the isovector channel. Therefore, in infinite nuclear matter, the isovector fields are proportional to the isovector

density, which are given by $N - Z$. This leads to a very stiff symmetry energy as a function of the density and to relatively large values for the symmetry energy J and its slope L at saturation (see Table IV in the Ref. [40]). The fits of other above-mentioned non-linear meson coupling functionals have tried to reduce this value. However, because of the stiffness of the linear ansatz this is possible only to a certain extent. Although these functionals are very successful for static CDFT close to the valley of stability [33], their common feature is that the neutron skin thicknesses are larger than those of successful Skyrme EDF's and DD CEDF's.

The masses m, m_ω and m_ρ of the DD-ME2 [26] functional are kept at fixed values. As discussed above the density dependence of the coupling constants $f_i(x)$ $i = \sigma, \omega, \rho$ is given by four independent parameters. Therefore, together with the four parameters m_σ, $g_\sigma(\rho_{\rm sat})$, $g_\omega(\rho_{\rm sat})$, and $g_\rho(\rho_{\rm sat})$ DD-ME2 contains eight independent parameters which have been fitted in Ref. [26] to a set experimental data in spherical nuclei:12 binding energies, 9 charge radii, and 3 neutron skin thicknesses.

The functional DD-MEδ [28] differs from the earlier DD-ME functionals also in the fitting strategy. It tries to use only a minimal number of free parameters adjusted to the data in finite nuclei and to use ab-initio calculations to determine the density dependence of the meson-nucleon vertices. Relativistic ab-initio calculations [23, 24] show clearly that the isovector scalar self-energy, i.e. the field of the δ-meson, is not negligible. Therefore, the functional DD-MEδ differs also from the other functionals by including the δ-meson, which leads to a different effective Dirac mass for protons and neutrons:

$$m^*_{n,p} = m + g_\sigma \sigma \pm g_\delta \delta. \tag{2.6}$$

As a consequence, the splittings of the spin-orbit doublets with large orbital angular momentum *l* are slightly different in the models with and without a δ-meson. However, this effect is too small to be seen in present experiments [28]. All the other effects of the δ-meson on experimental isovector properties of nuclear structure at densities below and slightly above saturation can be completely absorbed by a renormalization of the ρ-meson-nucleon vertex [28]. Therefore, successful phenomenological CEDF's do not need to include the δ-meson. However, the effects of the δ-meson are important for a proper description of the nuclear equation of state (EoS) at higher densities (see Ref. [28] and references given there) which play a role in heavy-ion reactions and in astrophysics.

In the earlier parameters sets DD-ME1 [41] and DD-ME2 [26], all eight independent parameters were adjusted to experimental data in finite nuclei, whereas for DD-MEδ only the four independent parameters m_σ, $g_\sigma(\rho_{\rm sat})$, $g_\omega(\rho_{\rm sat})$, and $g_\rho(\rho_{\rm sat})$ have been adjusted to experimental data in finite nuclei. This data set includes 161 binding energies and 86 charge radii of spherical nuclei. The parameter $g_\delta(\rho_{\rm sat})$ and the density dependence $f_i(x)$ have been fitted to parameter-free *ab-initio* calculations of infinite nuclear matter of various densities, as for instance the equations of state (EoS) for symmetric nuclear matter and pure neutron matter, and the difference in the effective Dirac masses $m_p^* - m_n^*$. Thus, the functional DD-MEδ is the most microscopically justified CEDF among functionals used in the investigation.

Table 2.1

The parameters of NL3*, DD-ME2 and DD-MEδ CEDF's.

Parameter	**NL3***	**DD-ME2**	**DD-MEδ**
m	939	939	939
m_σ	502.5742	550.1238	566.1577
m_ω	782.600	783.000	783.00
m_δ			983.0
m_ρ	763.000	763.000	763.0
g_σ	10.0944	10.5396	10.3325
g_ω	12.8065	13.0189	12.2904
g_δ			7.152
g_ρ	4.5748	3.6836	6.3128
g_2	-10.8093		
g_3	-30.1486		
a_σ		1.3881	1.3927
b_σ		1.0943	0.1901
c_σ		1.7057	0.3679
d_σ		0.4421	0.9519
e_σ		0.4421	0.9519
a_ω		1.3892	1.4089
b_ω		0.9240	0.1698
c_ω		1.4620	0.3429
d_ω		0.4775	0.9860
e_ω		0.4775	0.9860
a_δ			1.5178
b_δ			0.3262
c_δ			0.6041
d_δ			0.4257
e_δ			0.5885
a_ρ		0.5647	1.8877
b_ρ			0.0651
c_ρ			0.3469
d_ρ			0.9417
e_ρ			0.9737

2.2.2 Point coupling model

The Lagrangian for the density-dependent point coupling model [42, 27] is given by

$$\begin{aligned}\mathcal{L} = & \bar{\psi}\left(i\gamma\cdot\partial - m\right)\psi - \frac{1}{4}F_{\mu\nu}F^{\mu\nu} - e\bar{\psi}\gamma\cdot A\psi \\ & - \frac{1}{2}\alpha_S(\rho)\left(\bar{\psi}\psi\right)\left(\bar{\psi}\psi\right) - \frac{1}{2}\alpha_V(\rho)\left(\bar{\psi}\gamma^\mu\psi\right)\left(\bar{\psi}\gamma_\mu\psi\right) \\ & - \frac{1}{2}\alpha_{TV}(\rho)\left(\bar{\psi}\vec{\tau}\gamma^\mu\psi\right)\left(\bar{\psi}\vec{\tau}\gamma_\mu\psi\right) - \frac{1}{2}\delta_S\left(\bar{\psi}\psi\right)\Box\left(\bar{\psi}\psi\right).\end{aligned} \tag{2.7}$$

In addition to the free-nucleon part, and the point coupling interaction terms, there is also the coupling of the proton to the electromagnetic field. The derivative term in (2.7) with the D'Alembert operator $\Box$ accounts for the leading effects of finite-range interaction that are important for the quantitative description of nuclear density distribution. In analogy to the successful meson-exchange models, this model contains isoscalar-scalar (S), isoscalar-vector (V) and isovector-vector (TV) four-fermion interactions. The coupling constants $\alpha_i(\rho)$ are density dependent.

The Lagrangian (2.7) in this work represents the parametrization DD-PC1 [27] given in Table 2.2.

$$\alpha_i(\rho) = a_i + (b_i + c_i x)e^{-d_i x}, \quad \text{for } i = S, V, TV \tag{2.8}$$

is used for the functional form of the couplings, where $x = \rho/\rho_{\text{sat}}$ denotes the nucleon density in units of the saturation density of symmetric nuclear matter. In the isovector channel a pure exponential dependence is used, i.e. $a_{TV} = 0$ and $c_{TV} = 0$. The remaining set of 10 constants, a_S, b_S, c_S, d_S, a_V, b_V, c_V, d_V, b_{TV}, and d_{TV} that control the strength and density dependence of the interaction Lagrangian, was adjusted in a multistep parameter fit exclusively to the experimental masses of 64 axially deformed nuclei.

Table 2.2

The parameters of the DD-PC1 CEDF

Parameter	**DD-PC1**
m	939
a_S	-10.04616
b_S	-9.15042
c_S	-6.42729
d_S	1.37235
a_V	5.91946
b_V	8.86370
d_V	0.65835
b_{TV}	1.83595
d_{TV}	0.64025

2.2.3 The fitting protocols

The fitting protocols used for the derivation of the various CEDF's differ in the number and the type of experimental data. Figure 2.1 shows the nuclei which were used in the fits of the different CEDF's. NL3*, DD-ME2, DD-MEδ and DD-PC1 respectively. NL3*, DD-ME2, and DD-MEδ were fitted to spherical nuclei. Only 12 spherical nuclei were used in the fitting protocols of NL3* and DD-ME2. DD-MEδ was fitted to 161 spherical nuclei, while 64 deformed nuclei were used in the fitting for DD-PC1. Magic shell closures are shown by dashed lines in Fig. 2.1. In all these fitting protocols, the binding energies were used. In addition, the charge radii were employed in the fitting of NL3*, DD-ME2 and DE-MEδ. The number of independent parameters in the NL3*, DD-ME2, DD-MEδ and DD-PC1 CEDF is 6, 8, 14, and 10, respectively. Note, however, that in the case of DD-MEδ, only the 4 parameters are fitted to the properties of finite nuclei and additional 10 parameters are fitted to pseudo-data obtained from *ab initio* calculations of nuclear matter.

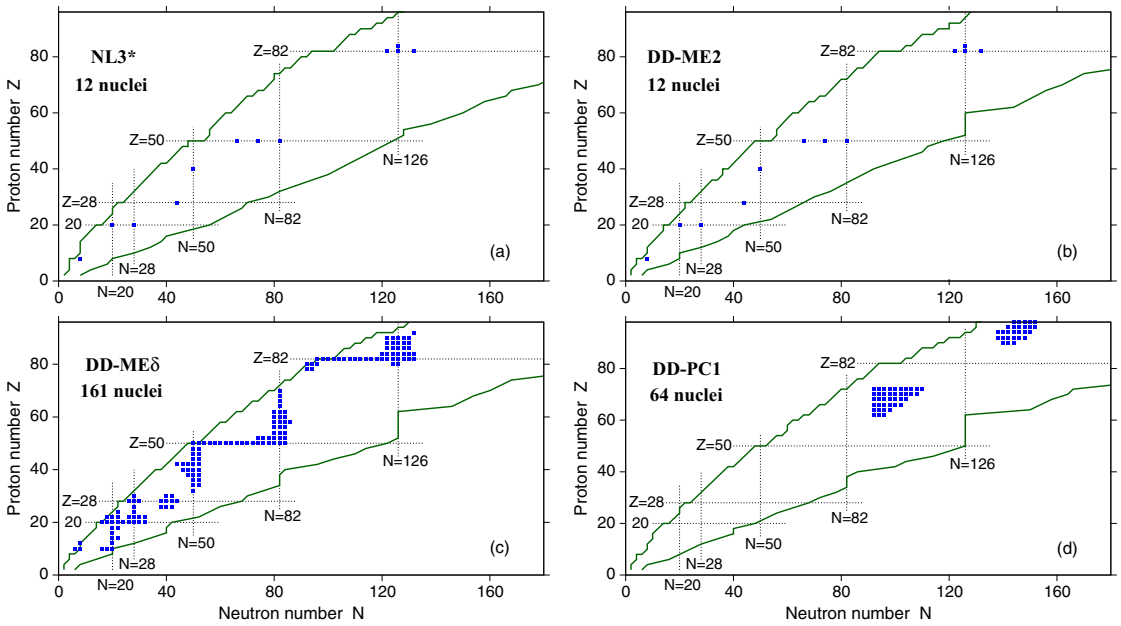

Figure 2.1

The nuclei (solid squares) used in the fit of indicated CDFT parametrizations.

2.3 Pairing correlation

Pairing plays an important role in our understanding of all nuclei with open shells. Without pairing, the relativistic theory can be only applied to few doubly magic nuclei or to nuclei at very large angular momenta, where pairing is considerably quenched [43]. In all other cases pairing correlations have to be taken into account in the constant gap approximation. On the mean field level they are taken into account by Bardeen-Cooper-Schrieffer (BCS) or Hartree-Fock-Bogoliubov (HFB) theory and in the relativistic case by Relativistic Hartree-Bogoliubov(RHB) theory [44, 43, 45]. Nuclear energy density functionals depend on two densities, the normal density

$$\rho_{n_1 n_2} = \langle \Phi | c^{\dagger}_{n_2} c_{n_1} | \Phi \rangle, \tag{2.9}$$

and the anomalous density

$$\kappa_{n_1 n_2} = \langle \Phi | c_{n_2} c_{n_1} | \Phi \rangle \tag{2.10}$$

also called the pairing tensor. $|\Phi\rangle$ is the RHB wave function, a generalized Slater determinant [46] and, therefore, the density ρ as well as κ depend on the pairing correlations. In particular, the density matrix ρ is no longer a projector on the subspace of occupied states:

$$\rho^2 - \rho = \kappa\kappa^*. \tag{2.11}$$

In the relativistic form the nuclear energy functional is usually given by

$$E_{RHB}[\rho, \kappa] = E_{RMF}[\rho] + E_{pair}[\kappa], \tag{2.12}$$

where $E_{RMF}[\rho]$ has the same functional form as the CEDF's discussed in the last section, but it is now a functional of the density ρ in Eq. (2.9) depending on the RHB wave function $|\Phi\rangle$. The pairing energy[1]. is given by

$$E_{pair}[\kappa] = \frac{1}{4} \sum_{n_1 n_2, n_1' n_2'} \kappa^*_{n_1 n_2} \langle n_1 n_2 | V^{pp} | n_1' n_2' \rangle \kappa_{n_1' n_2'} \tag{2.13}$$

The Dirac equation for fermion fields $\psi(r)$ is replaced by the RHB equation. The RHB framework with finite range pairing and its separable limit are used for a systematic study of ground state properties of all even-even nuclei from the proton to neutron drip line. It has the proper coupling to the continuum at the neutron drip line. This allows a correct description of weakly bound nuclei that are close to the neutron drip line. Also nuclear halo phenomena can be described by this method, if a proper basis is used, such as the coordinate space [47, 48] or a Woods-Saxon basis [49].

[1]The details for the treatment of pairing are presented in Sec. 2.4

The RHB equations for the fermions are given by [45]

$$\begin{pmatrix} \hat{h}_D - \lambda & \hat{\Delta} \\ -\hat{\Delta}^* & -\hat{h}_D^* + \lambda \end{pmatrix} \begin{pmatrix} U(r) \\ V(r) \end{pmatrix}_k = E_k \begin{pmatrix} U(r) \\ V(r) \end{pmatrix}_k \tag{2.14}$$

Here, $\hat{h}_D$ is the Dirac Hamiltonian for the nucleons with mass m; λ is the chemical potential defined by the constraints on the average particle number for protons and neutrons; $U_k(r)$ and $V_k(r)$ are quasiparticle Dirac spinors [44, 43, 45] and E_k denotes the quasiparticle energies. The Dirac Hamiltonian

$$\hat{h}_D = \boldsymbol{\alpha}(\boldsymbol{p} - \boldsymbol{V}) + V_0 + \beta(m + S). \tag{2.15}$$

contains an attractive scalar potential

$$S(r) = g_\sigma \sigma(r), \tag{2.16}$$

a repulsive vector potential

$$V_0(r) \;=\; g_\omega \omega_0(r) + g_\rho \tau_3 \rho_0(r) + eA_0(r), \tag{2.17}$$

and a magnetic potential

$$V(r) \;=\; g_\omega \omega(r) + g_\rho \tau_3 \rho(r) + eA(r). \tag{2.18}$$

The last term breaks time-reversal symmetry and induces currents. Time-reversal symmetry is broken when the time-reversed orbitals are not occupied pairwise. This takes place in odd-mass nuclei [50]. In the Dirac equation, the space-like components of the vector mesons $\omega(r)$ and $\rho(r)$ have the same structure as the space-like component $A(r)$ generated by the photons. Since $A(r)$ is the vector potential of the magnetic field, by analogy the

effect due to presence of the vector field $V(r)$ is called *nuclear magnetism* [51]. It affects the properties of odd-mass nuclei [50]. Thus, the spatial components of the vector mesons are properly taken into account for such nuclei. This is done only for the study of odd-even mass staggerings as it has been successfully done earlier for the studies of single-particle [52, 53] and pairing [54] properties of deformed nuclei. Nuclear magnetism, i.e. currents and time-odd mean fields, plays no role in the studies of even-even nuclei.

2.4 The effective pairing interaction

The pair field $\hat{\Delta}$ in RHB theory is given by

$$\hat{\Delta} \equiv \Delta_{n_1 n_2} \;=\; \frac{1}{2}\sum_{n_1' n_2'} \langle n_1 n_2 | V^{pp} | n_1' n_2' \rangle \kappa_{n_1' n_2'} \tag{2.19}$$

It contains the pairing tensor κ of Eq.(2.10)

$$\kappa = V^* U^T \tag{2.20}$$

and the effective interaction V^{pp} in the particle-particle channel.

Two types of realistic effective pairing interaction have been used in this investigation. Both of them have finite range and, therefore, provide an automatic cutoff of high-momentum components. These are as follows:

- The Brink-Booker part of phenomenological non-relativistic D1S Gogny-type finite range interaction

$$V^{pp}(1,2) \;=\; f\sum_{i=1,2} e^{-[(r_1-r_2)/\mu_i]^2}(W_i + B_i P^\sigma - H_i P^\tau - M_i P^\sigma P^\tau) \tag{2.21}$$

  The motivation for such an approach to the description of pairing is given in Refs. [55, 45]. In Eq. (2.21), μ_i, W_i, B_i, H_i and M_i $(i = 1, 2)$ are the parameters of the

force and P^σ and P^τ are the exchange operators for the spin and isospin variables. The D1S parametrization of the Gogny force [56, 57] is used here. Note that a scaling factor f is introduced in Eq. (2.21). Its role is discussed below.

- A separable pairing interaction of finite range introduced by Tian et al [58]. Its matrix elements in r-space have the form

$$V(r_1, r_2, r_1', r_2') \;=\; -f\, G\delta(R - R')P(r)P(r')\frac{1}{2}(1 - P^\sigma) \tag{2.22}$$

with $R = (r_1 + r_2)/2$ and $r = r_1 - r_2$ being the center of mass and relative coordinates. The form factor $P(r)$ is of Gaussian shape,

$$P(r) = \frac{1}{(4\pi a^2)^{3/2}} e^{-r^2/4a^2}. \tag{2.23}$$

The parameters of this interaction have been derived by a mapping of the ^{1}S$_0$ pairing gap of infinite nuclear matter to that of the Gogny force D1S. The resulting parameters are: $G = 738$ fm^3 and $a = 0.636$ fm [58]. The scaling factor f is the same as in Eq. (2.21).

Both in theory and in experiment the strength of pairing correlations is usually accessed via the three-point indicator [59]

$$\Delta^{(3)}(N) = \frac{\pi_N}{2}\left[B(N-1) + B(N+1) - 2B(N)\right], \tag{2.24}$$

which quantifies the odd-even staggering (OES) of binding energies. Here $\pi_N = (-1)^N$ is the number parity and $B(N)$ is the (negative) binding energy of a system with N particles. In Eq. (2.24), the number of protons Z is fixed, and N denotes the number of neutrons,

i.e. this indicator gives the neutron OES. The factor depending on the number parity π_N is chosen so that the OES centered on even and odd neutron number N will both be positive. An analogous proton OES indicator $\Delta^{(3)}(Z)$ is obtained by fixing the neutron number N and replacing N by Z in Eq. (2.24).

As discussed in Ref. [54], in many applications of RHB theory with the pairing force D1S the same scaling factor f has been used across the nuclear chart. However, it was found a decade ago that a proper description of rotational properties in actinides [52] requires weaker pairing as compared with the rare-earth region [60, 45]. Subsequent systematic studies of pairing (via the three-point indicator $\Delta^{(3)}$) and rotational properties of actinides confirmed this observation in Refs. [54, 61]. The investigation of odd-even mass staggerings in spherical nuclei in Ref. [62] also confirms the need for a scaling factor f which depends on the region in the nuclear chart. The studies of Refs. [52, 54, 62] show also a weak dependence of the scaling factor f on the CDFT parametrization. We therefore introduce in Eqs. (2.21) and (2.22) a scaling factor f for a fine tuning of the effective pairing force.

The scaling factor f used in the present investigation has been selected based on the results of a comparison between experimental moments of inertia and those obtained in cranked RHB calculations with the CEDF NL3*. As verified in the actinides in Ref. [54], the strengths of pairing defined by means of the moments of inertia and by the three-point indicators $\Delta^{(3)}$ strongly correlate in deformed nuclei. Following the results obtained in Ref. [54], the scaling factor has been fixed at $f = 1.0$ in the $Z \geq 88$ actinides and superheavy nuclei. The analysis of the moments of inertia in the rare-earth region [63]

leads to a scaling factor of $f = 1.075$ for the $56 \leq Z \leq 76$ rare-earth nuclei. For $Z \leq 44$ nuclei, the scaling factor was fixed at $f = 1.12$ [63]. The scaling factor gradually changes with Z in between of these regions. Since the strength parameter G of the separable force has been determined in Ref. [58] by a direct mapping to the Gogny force D1S, the same scaling factors are also used in the following RHB calculations with separable pairing.

CHAPTER III

GLOBAL PERFORMANCE OF COVARIANT ENERGY DENSITY FUNCTIONALS: GROUND STATE OBSERVABLES OF EVEN-EVEN NUCLEI AND THE ESTIMATE OF SYSTEMATIC THEORETICAL UNCERTAINTIES

3.1 Introduction

Theoretical description of ground state properties of nuclei is important for our understanding of their structure. It is also important for nuclear astrophysics, where we are facing the problem of an extrapolation to the nuclei with large isospin. Many of such nuclei will not be studied experimentally even with the next generation of facilities. Thus, it is important to answer two questions, namely, how well the existing nuclear EDF's describe available experimental data, and how well do they extrapolate to the region of unknown nuclei.

The answer to the first question is not possible for the majority of nuclear EDF's since their global performance is not known. This is especially true for the covariant energy density functionals (CEDF's). Very few of them were confronted with experimental data on a global scale. Even the new generation of CEDF's such as NL3* [33], DD-ME2 [26], DD-MEδ [28] and DD-PC1 [27] have not passed this critical test before our studies. This is because only limited sets of nuclei, usually located in the region of nuclei used in the fitting protocol, were confronted with calculations. Thus, it is not known how well they

describe ground state properties on a global scale and what are their strong and weak points in that respect.

The answer on the question "How well a given CEDF extrapolates towards neutron-rich nuclei?" is well connected with the answer to the first question. This is because one can estimate its reliability for the description of nuclei far away from the region of known nuclei only by assessing its global performance on existing experimental data. A good performance in known nuclei is a necessary condition and one has to be very careful with extrapolations of models where this good performance has been achieved with a large number of phenomenological parameters.

It was suggested in Refs. [64, 5, 65] to use the methods of information theory and to define the uncertainties in the EDF parameters. These uncertainties come from the selection of the form of EDF as well as from the fitting protocol details, such as the selection of the nuclei under investigation, the physical observables etc. Some of them are called *statistical errors* and can be calculated from a statistical analysis during the fit, others are systematic errors. On the basis of these statistical errors and under certain assumptions on the independence of the form of many EDF's one hopes to be able to deduce in this way *theoretical error bars* for the prediction of physical observables [64, 5, 65]. It is very difficult to perform the analysis of statistical errors on a global scale since the properties of transitional and deformed nuclei have to be calculated repeatedly for different variations of original CEDF. Hence, such statistical analysis has been performed mostly for spherical nuclei [64, 66] or selected isotopic chains of deformed nuclei [5].

Even though such analysis has its own merits, at present, it does not allow to fully estimate theoretical uncertainties in the description of physical observables. This is because they originate not only from the uncertainties in model parameters, but also from the definition and the limitations of the model itself. The later uncertainties are difficult to estimate. Hence, any analysis of theoretical uncertainties contains a degree of arbitrariness related to the choice of the model and fitting protocol.

Because of these difficulties, we concentrate on the uncertainties related to the present choice of energy density functionals which can be relatively easily deduced globally. The *theoretical systematic uncertainties* is defined for a given physical observable by the spread of theoretical predictions within the four CEDF's

$$\Delta O(Z,N) = |O_{\max}(Z,N) - O_{\min}(Z,N)| \tag{3.1}$$

where $O_{\max}(Z,N)$ and $O_{\min}(Z,N)$ are the largest and smallest values of the physical observable $O(Z,N)$ obtained with the four employed CEDF's for the (Z,N) nucleus. In our study, we used state-of-the-art CEDF of different classes: these are NL3*, DD-ME2, DD-MEδ and DD-PC1. The word *spread* is used for these theoretical systematic uncertainties for the CEDF's.

3.2 Details of numerical calculation

The systematic investigations of even-even nuclei are performed within the axial RHB computer code outlined below. As the absolute majority of nuclei are known to be axially and reflection symmetric in their ground states, we consider only axial and parity-

conserving intrinsic states and solve the RHB-equations in an axially deformed harmonic oscillator basis [34, 67].

We have developed a parallel version of the axial RHB computer code starting from a considerably modified version of the computer code DIZ [67]. This code is based on an expansion of the Dirac spinors and the meson fields in terms of harmonic oscillator wave functions with cylindrical symmetry. The calculations are performed by successive diagonalizations using the method of quadratic constraints [46]. The parallel version allows simultaneous calculations for a significant number of nuclei and deformation points in each nucleus. For each nucleus, we minimize

$$E_{RHB} + \frac{C_{20}}{2}(\langle \hat{Q}_{20} \rangle - q_{20})^2 \tag{3.2}$$

where E_{RHB} in Eq. (2.12) is the total energy and $\langle \hat{Q}_{20} \rangle$ denotes the expectation value of the mass quadrupole operator,

$$\hat{Q}_{20} = 2z^2 - x^2 - y^2 \tag{3.3}$$

q_{20} is the constrained value of the multipole moment, and C_{20} the corresponding stiffness constant [46]. In order to provide the convergence to the exact value of the desired multipole moment we use the method suggested in Ref. [68]. Here the quantity q_{20} is replaced by the parameter q_{20}^{eff}, which is automatically modified during the iteration in such a way that we obtain $\langle \hat{Q}_{20} \rangle = q_{20}$ for the converged solution. This method works well in our constrained calculations. The details of the calculational scheme are as follows:

- Three classes of covariant density functional models are used throughout this thesis: the nonlinear meson-nucleon coupling model (NL), the density-dependent meson-

exchange model (DD-ME) and the density-dependent point-coupling model (DD-PC). The main differences between them lay in the treatment of the range of the interaction and in the density dependence. They are represented by four CEDFs NL3* [33], DD-ME2 [26], DD-MEδ [28] and DD-PC1 [27]. The details have been discussed in the preceeding chapter of this dissertation.

- The truncation of the basis is performed in such a way that all states belonging to the major shells up to $N_F = 20$ fermionic shells and up to $N_B = 20$ bosonic shells are taken into account. The comparison with the results obtained with $N_F = 26$ and $N_B = 26$ shows that this truncation scheme provides sufficient numerical accuracy for the description of weakly bound nuclei in the vicinity of the neutron drip line and of superheavy nuclei.

- The potential energy curve for each nucleus is calculated in a large deformation range from $\beta_2 = -0.4$ up to $\beta_2 = 1.0$ by means of the constraint on the quadrupole moment q_{20}. The lowest in energy minimum is defined from the potential energy curve. After which the unconstrained calculations are performed in this minimum and the correct ground state configuration and its energy are determined.

- In axial reflection-symmetric calculations for superheavy nuclei with $Z \geq 106$, the superdeformed minimum is mostly lower in energy than the normal deformed one [69, 70]. As long as triaxial [70] and octupole [69, 70] deformations are not included, this minimum is stabilized by the presence of an outer fission barrier. Including such deformations, however, it often turns out that this minimum becomes a saddle point,

unstable against fission [69, 70]. Since these deformations are not included in the present calculations, we restrict our consideration to spherical or normal deformed ground states in nuclei with $Z \leq 104$.

The aims of the present study are as follow: (i) the assessment of global performance of the state-of-the-art NL3*, DD-ME2, DD-MEδ, and DD-PC1 CEDF's for even-even nuclei within the relativistic Hartree-Bogoliubov (RHB) framework [44, 55], (ii) the estimation of differences in the description of various physical observables on a global scale and (iii) the comparison of the drip lines obtained in relativistic and non-relativistic DFT.

3.3 Binding energies

Table 3.1

The rms deviations $\Delta E_{\rm rms}$, $\Delta(S_{2n})_{\rm rms}$, and $\Delta(S_{2p})_{\rm rms}$.

EDF	**measured**	**measured+estimated**		
	$\Delta E_{\rm rms}$	$\Delta E_{\rm rms}$	$\Delta(S_{2n})_{\rm rms}$	$\Delta(S_{2p})_{\rm rms}$
NL3*	2.96	3.00	1.23	1.29
DD-ME2	2.39	2.45	1.05	0.95
DD-MEδ	2.29	2.40	1.09	1.09
DD-PC1	2.01	2.15	1.16	1.03

In Table 3.1 we list the rms deviations $\Delta E_{\rm rms}$, $\Delta(S_{2n})_{\rm rms}$, and $\Delta(S_{2p})_{\rm rms}$ between theoretical and experimental binding energies E and two-neutron(-proton) separation energies S_{2n} (S_{2p}) for the global RHB calculations with the different CEDF's investigated in this chapter of the dissertation. The masses given in the AME2012 mass evaluation [12]

can be separated into two groups. One represents nuclei with masses defined only from experimental data, the other contains nuclei with masses depending in addition on either interpolation or extrapolation procedures. The masses of the nuclei in the first and second groups as called measured and estimated, respectively. There are 640 measured and 195 estimated masses of even-even nuclei in the AME2012 mass evaluation. It can be seen in Table 3.1 that the extension to include also estimated masses leads to a slight decrease of the accuracy in the description of experimental data.

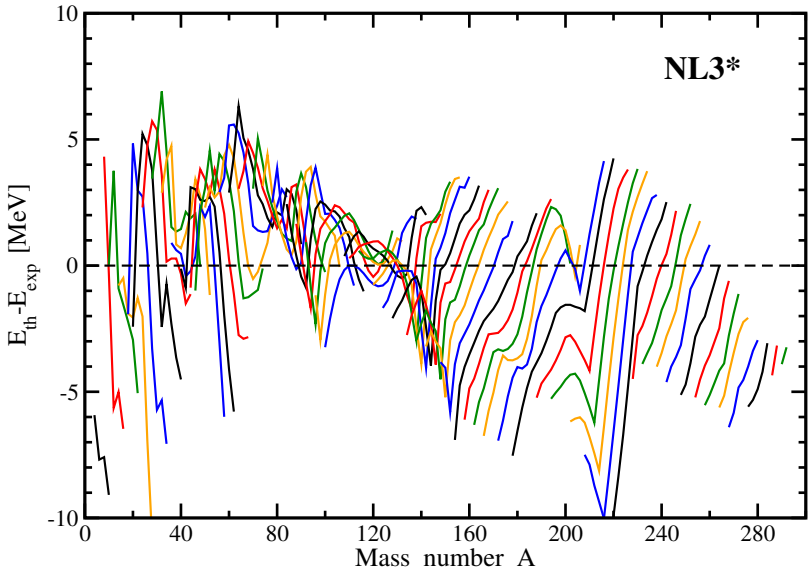

Figure 3.1

The difference between theoretical and experimental masses.

Figure 3.1 is the difference between theoretical and experimental masses of 835 even-even nuclei investigated in RHB calculations with NL3*. If $E_{th} - E_{exp} < 0$, the nucleus is more bound in the calculations than in experiment.

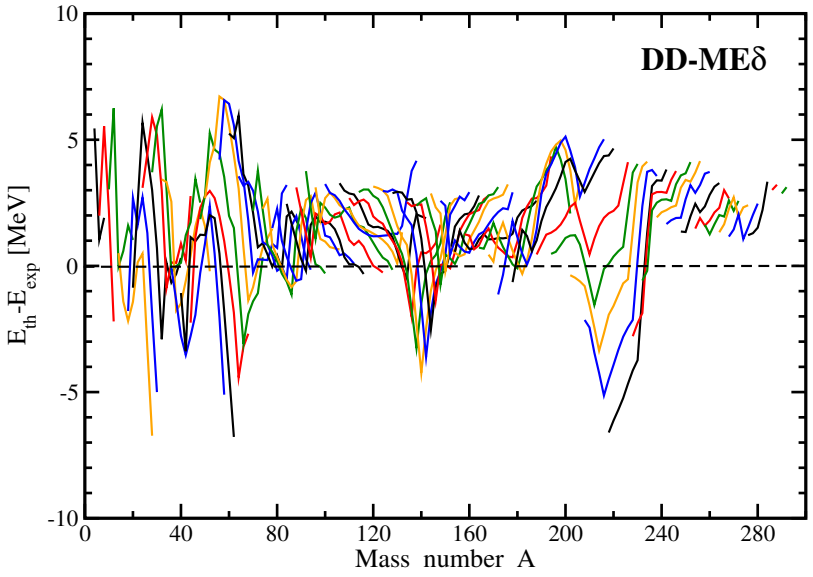

Figure 3.2

The same as in Fig. 3.1 but with DD-MEδ.

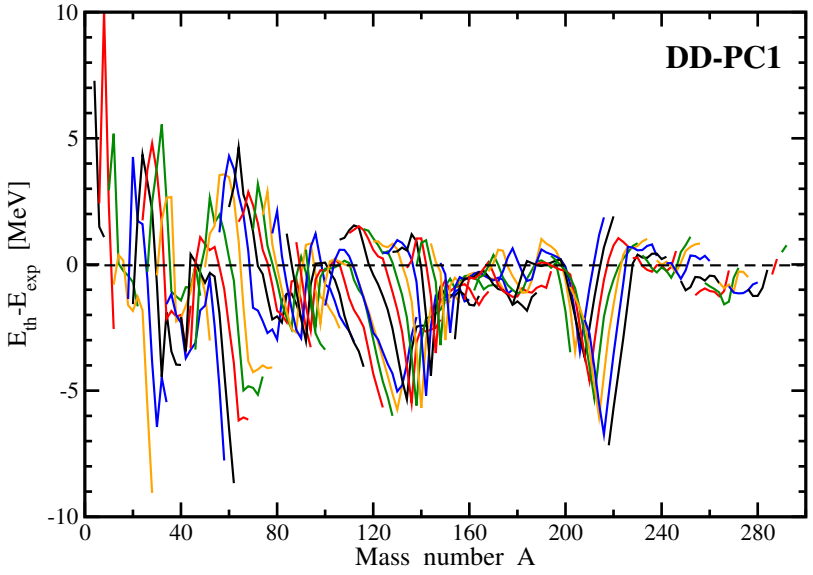

Figure 3.3

The same as in Fig. 3.1 but with DD-PC1.

To our knowledge, for relativistic density functionals, reliable[1] global comparisons of experimental and theoretical masses have been performed so far only for the parametrizations NL3 [38], FSUGold [76], BSR4 [77] and TM1 [78] in the RMF+BCS approach using the constant gap approximation in Ref. [75] and for PC-PK1 [79] in the RMF+BCS approach with density-dependent pairing in Ref. [80]. Apart of BSR4 and PC-PK1 these CEDF's were fitted more than ten years ago. The rms-errors for the masses found for these CEDF's are 3.8 MeV for NL3, 6.5 MeV for FSUGold, 2.6 MeV for BSR4, 5.9 MeV for TM1 and 2.6 MeV for PC-PK1 (at the mean field level).

One can see that the CEDF's NL3*, DD-MEδ, and DD-PC1 investigated in this chapter provide an improved description of masses across the nuclear chart. The rms deviations for the binding energies presented in Table 3.1 are more statistically significant than those of Refs. [75] and [80] since they are defined for 835 even-even nuclei. On the contrary, rms deviations for binding energies for the NL3, FSUGold, BSR4 and TM1 CEDF's are defined only for 513 (575 for PC-PK1) even-even nuclei in Refs. [75] and [80]. The extension of the experimental database to 835 nuclei may lead to further deterioration of the rms-deviations for these CEDF's.

The accuracy of the description of the masses of heavy nuclei is comparable with or even better than that of medium-mass and light nuclei (Figs. 3.1, 3.2, and 3.3). The large

[1]The masses were globally studied earlier in the RMF [71] or RMF+BCS [72, 73] formalisms. However, the pairing correlations have been completely ignored in the studies of Ref. [71]. The treatment of pairing via the BCS approximation in Refs. [72, 73] has to be taken with care in the region of the drip line since this approximation does not take into account the continuum properly and leads to the formation of a neutron gas [74] in nuclei near neutron drip line. In addition, these calculations use at most 14 fermionic shells for the harmonic oscillator basis, which according to our study and the one of Ref. [75] is not sufficient for a correct description of binding energies of actinides and superheavy nuclei and the nuclei in the vicinity of neutron drip line.

deviation peaks seen in Figs. 3.1, 3.2, and 3.3 are located in the vicinity of the doubly magic shell closures. For such nuclei, medium polarization effects associated with surface and pairing vibrations have a substantial effect on the binding energies [81]

Previous estimates of the rms deviations for binding energies with these CEDF's have been obtained only with restricted sets of experimental data. For example, the RHB(NL3*) results were compared with approximately 180 experimental even-even nuclei in Ref. [33]. But, no rms deviations for binding energies were presented for this set. An rms-deviation of 2.4 MeV has been obtained in the analysis of 161 nuclei in the RMF+BCS calculations with DD-MEδ using monopole pairing [28]. Note, however, that the binding energies of these nuclei were used in the fit of DD-MEδ. 93 deformed nuclei calculated in the RMF+BCS approach with DD-PC1 CEDF were compared with experiment in Ref. [27]. The binding energies of most of these nuclei deviate from experiment by less than 1 MeV, which is not surprising considering that 64 of these nuclei were used in the fit of the corresponding CEDF. However, much larger deviations have been reported for this CEDF in spherical nuclei [27]. DD-PC1 is the only CEDF exclusively fitted to deformed nuclei.

Comparing these rms deviations with the ones presented in Table 3.1, it can be seen that the increase of the size of experimental data set leads to a deterioration of the average description of the binding energies. This suggests that the experimental data sets used in the fits of the CEDF's are not sufficiently large to provide an optimal localization of the model parameters in the parameter space and reliable extrapolation properties of the CEDF's with respect to binding energies. To the best of our knowledge, no attempt to create a "mass table" quality CEDF based on a fit to the full set of available experimental masses has been

undertaken in CDFT. This is contrary to non-relativistic models where mass tables based on an extensive use of experimental data were generated in the macroscopic+microscopic model [6], the Skyrme [82] and the Gogny [83] DFT.

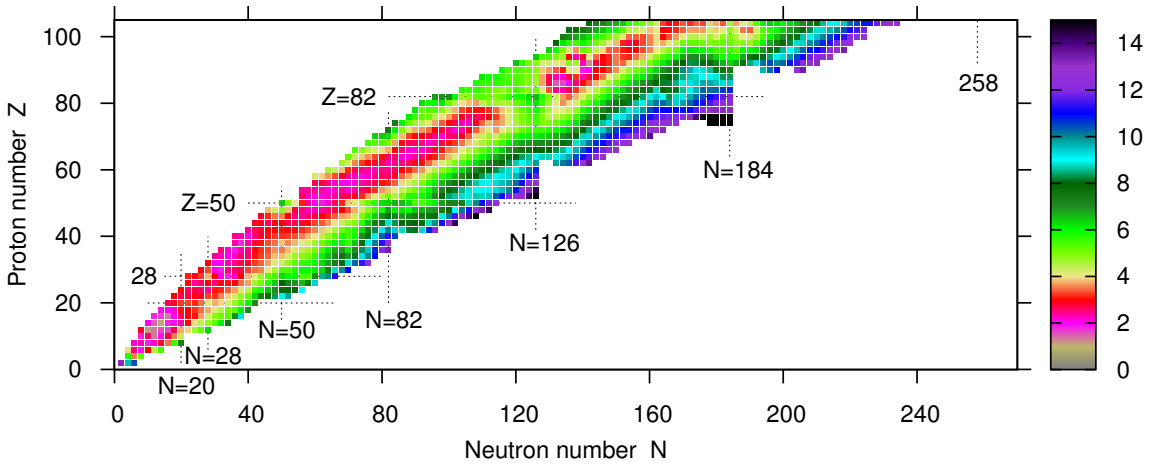

Figure 3.4

The binding energy spreads $\Delta E(Z,N)$ as a function of proton and neutron number.

In Fig. 3.4 we show the binding energy spreads $\Delta E(Z,N)$ as a function of proton and neutron number $\Delta E(Z,N) = |E_{\max}(Z,N) - E_{\min}(Z,N)|$, where $E_{\max}(Z,N)$ and $E_{\min}(Z,N)$ are the largest and the smallest binding energies for each (N,Z) nucleus obtained with the four CEDF's used in this investigation. The comparison of this figure with Fig. 1 in Ref. [84] shows that the spreads in the predictions of binding energies stay within 5-6 MeV for the known nuclei. These spreads are even smaller (typically around 3 MeV) for the nuclei in the valley of beta-stability. However, the theoretical systematic uncertainties for the masses increase drastically when approaching the neutron-drip line and in

some nuclei they reach 15 MeV. This is a result of the poorly defined isovector properties of many CEDF's.

3.4 Separation energies

Since our investigation is restricted to even-even nuclei, we only consider two-neutron $S_{2n} = B(Z, N-2) - B(Z, N)$ and two-proton $S_{2p} = B(Z-2, N) - B(Z, N)$ separation energies. $B(Z, N)$ stands for the binding energy of a nucleus with Z protons and N neutrons. The accuracy of the description of separation energies depends on the accuracy of the description of mass differences. As a result, not always the functional which provides the best description of masses gives the best description of two-particle separation energies.

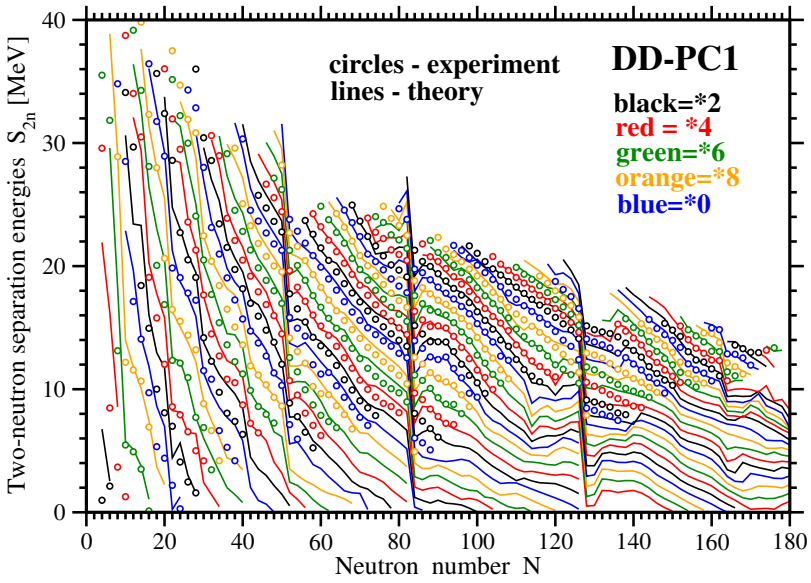

Figure 3.5

Two-neutron separation energies $S_{2n}(Z, N)$ given for different isotopic chains as a function of neutron number.

In Fig. 3.5 we show the two-neutron separation energies $S_{2n}(Z,N)$ given for different isotopic chains as a function of neutron number. To facilitate the comparison between theory and experiment, five different colors are used periodically as a function of neutron number. Black, red, green, orange and blue colors are used for isotope chains with proton numbers ending with 2, 4, 6, 8 and 0, respectively.

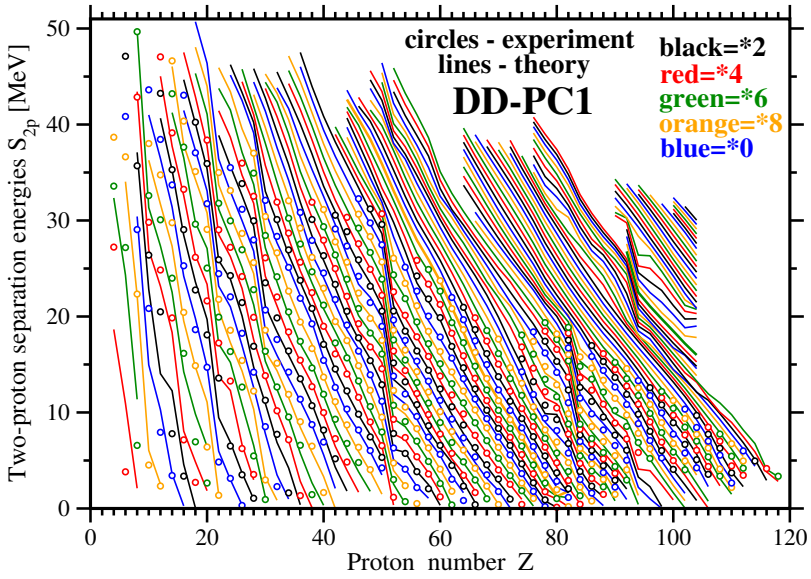

Figure 3.6

Two-proton separation energies $S_{2p}(Z,N)$ given for different isotonic chains as a function of proton number.

In Fig. 3.6 we show the two-proton separation energies $S_{2p}(Z,N)$ given for different isotonic chains as a function of proton number. To facilitate the comparison between theory and experiment, five different colors are used periodically as a function of proton number. Black, red, green, orange and blue colors are used for isotonic chains with neutron numbers ending with 2, 4, 6, 8 and 0, respectively.

The accuracy of the description of two-neutron and two-proton separation energies is illustrated for different isotopic and isotonic chains on the example of RHB calculations with DD-PC1 in Figs. 3.5 and 3.6. Similar results were obtained also in the calculations with NL3*, and DD-MEδ. It can be seen that the two-proton separation energies are better described than the two-neutron separation energies (see also Table 3.1). In part, this is a consequence of the behavior of the calculated S_{2n} curves in the vicinity of spherical shell gaps. The experimental S_{2n} curves are smooth as a function of neutron number between shell gaps (Fig. 3.5). For a given isotope chain, the calculations rather well reproduce this behavior of experimental S_{2n} curves in the regions of a few neutrons away from shell closures. However, the situation is different in the vicinity of the $N = 82$ and 126 shell closures. Here, the calculations overestimate (underestimate) experimental S_{2n} values for a few nuclei before (after) the shell closure in a number of isotopic chains with $Z \geq 40$.

Such problems do not exist for two-proton separation energies (Fig. 3.6). The origin of these problems is most likely related to the relative impact of proton and neutron shell closures. Fig. 3.11 shows that the band of nuclei with spherical or near-spherical deformations (gray area in the figures) is wider around $N = 82$ and $N = 126$ as compared with the one around $Z = 50$ and $Z = 82$. Thus, the transition from spherical shapes to well-deformed shapes (where the mean field description is justified) proceeds faster (in terms of particle number) for the proton subsystem than for the neutron subsystem. In contrast, the transitional shapes requiring a beyond mean field description are expected for a wider range of nuclei around the $N = 82$ and $N = 126$ shell closures. The neglect of these beyond mean field correlations is most likely source for the above mentioned discrepan-

cies between experimental and calculated S_{2n} values in the vicinity of the $N = 82$ and $N = 126$ shell closures.

3.5 Two-proton drip line.

The particle stability of a nuclide is specified by its separation energy. If the two-neutron and the two-proton separation energies are positive, the nucleus is stable against two-nucleon emission. Conversely, if one of these separation energies is negative, the nucleus is unstable. Thus, the two-neutron or the two-proton drip line is reached when $S_{2n} \leq 0$ or $S_{2p} \leq 0$, respectively.

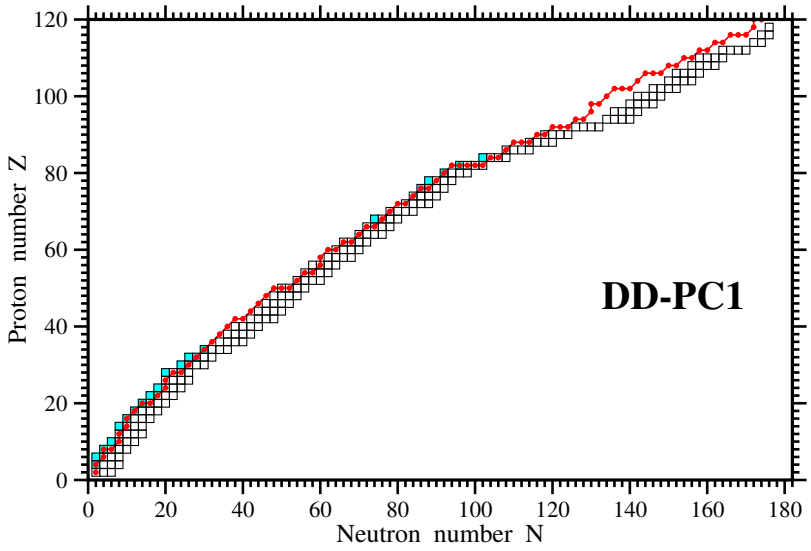

Figure 3.7

The calculated two-proton drip lines versus experimental data.

The proton drip line has been studied extensively more than a decade ago in the RHB framework with the finite range Gogny pairing force D1S in Refs. [85, 86, 87, 88, 89, 90,

91]. However, the main emphasis was put on the one-proton drip line, for which, at the time of these studies, experimental data was more available than that for the two-proton drip line. In addition, only the NL3 parametrization [38] has been used in these studies. Therefore, no estimate of theoretical errors in the predictions of one- and two-proton drip lines are available. These gaps in our knowledge of the CDFT performance have been filled by us in Ref. [84], where the two-proton drip lines were studied with NL3*, DD-ME2, DD-PC1 and DD-MEδ. Theoretical uncertainties in the definition of two-proton drip line have been deduced.

Here, we present a detailed comparison of the RHB results with the experiment. Fig. 3.7 compares experimental data with calculated two-proton drip line obtained with DD-PC1. The experimental two-proton drip line is delineated firmly or tentatively up to $Z = 84$. The red line with small solid circles shows the calculated two-proton drip line. Nuclei to the left of this line are proton unstable in the calculations. Nuclei which are proton unstable in experiment are shown by solid cyan squares. In the following discussions we concern with isotope chains containing proton unstable nuclei since this provides the most reliable experimental information on the position of two-proton drip line. One can see that with DD-PC1, proton unbound $Z = 4$, 8, 16, 18, 20, 32, 34, 76, 80, and 82 nuclei are predicted to be proton bound in the calculations and the two-proton drip line is predicted too early for this parametrization for the $Z = 56$ isotopes. Similar analysis has been done for NL3*, DD-ME2, and DD-MEδ (see Ref. [40] for details).

In general, the results of the calculations are very close to experimental data. This is because the proton-drip line lies close to the valley of stability, hence extrapolation errors

towards it are small. Another reason is the fact that the Coulomb barrier provides a rather steep potential reducing considerably the coupling to the proton continuum. This leads to a relatively low density of the single-particle states in the vicinity of the Fermi level.

Since this density is comparable with the one for the nuclei away from two-proton drip line, the slope of the two-proton separation energy S_{2p} as a function of proton number for a given isotonic chain remains almost unchanged on approaching the two-proton drip line (Fig. 3.6). As a consequence, theoretical uncertainties for the two-proton drip line are rather small for $Z \leq 86$ but somewhat larger for higher Z (see Fig. 2 in Ref. [84]) due to the increase of the single-particle level density and the related decrease of the slope of S_{2p} as a function of proton number (Fig. 3.6).

According to Fig. 2 of Ref. [84], theoretical uncertainties in the predictions of the position of two-proton drip line are either very small (2 neutrons) or non-existent for isotope chains with $Z \leq 86$. These small uncertainties may be a source of observed discrepancies between calculations and experiment for a number of isotope chains. However, in a number of the cases (for example, in the $Z = 32$ and 34 isotopes chains) there is no uncertainty in the predicted position of two-proton drip line (Fig. 2 in Ref. [84]). Thus, the observed discrepancies between theory and experiment may be due to the limitations of the model description on the mean field level. Indeed, it is well known that the Ge ($Z = 32$) [92] and Se ($Z = 34$) [93, 94] isotopes show prolate-oblate shape coexistence and/or γ-softness near the proton-drip line. A similar shape coexistence is also observed in heavier Kr [95, 96, 97, 98] and Rb [99] nuclei as well as in the $Z \sim 82$ proton-drip line nuclei [100, 101]. By ignoring the correlations beyond mean field, we may introduce an

error in the predicted position of two-proton drip line. The uncertainties in the definition of the two-proton drip lines obtained with the CDFT and SDFT are shown in Fig. 3.8.

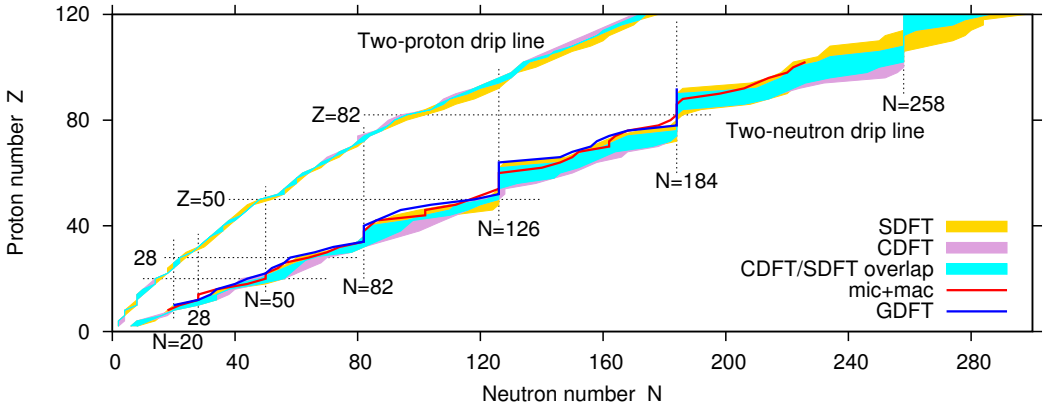

Figure 3.8

The comparison of the uncertainties in the definition of two-proton and two-neutron drip lines obtained in CDFT and SDFT.

In Figure 3.8 we show the comparison of the uncertainties in the definition of two-proton and two-neutron drip lines obtained in CDFT and SDFT. The shaded areas are defined by the extremes of the predictions of the corresponding drip lines obtained with different parametrizations. The blue shaded area shows the area where the CDFT and SDFT results overlap. Non-overlapping regions are shown by dark yellow and plum colors for SDFT and CDFT, respectively. The results of the SDFT calculations are taken from the supplement to Ref. [5]. The two-neutron drip lines obtained by microscopic+macroscopic (FRDM [6]) and Gogny D1S DFT [7] calculations are shown by red and blue lines, respectively.

3.6 Two-neutron drip line.

As discussed in Refs. [5, 84], the situation is different for the two-neutron drip line. Fig. 3.9 presents the compilation of known calculated two-neutron drip lines obtained with the state-of-the-art relativistic and non-relativistic EDF's. They include four two-neutron drip lines obtained in the CDFT calculations of Ref. [84], which are tabulated in Table 3.3. Non-relativistic results are represented by two-neutron drip lines obtained with the Gogny functional D1S [7] and with eight functionals of Skyrme type [5, 102]. In addition, the two-neutron drip line from the microscopic+macroscopic calculations of Ref. [6] is also shown. It can be seen that with the exception of two encircled regions, the theoretical differences in the location of two-neutron drip line are much larger than the ones for the two-proton drip line.

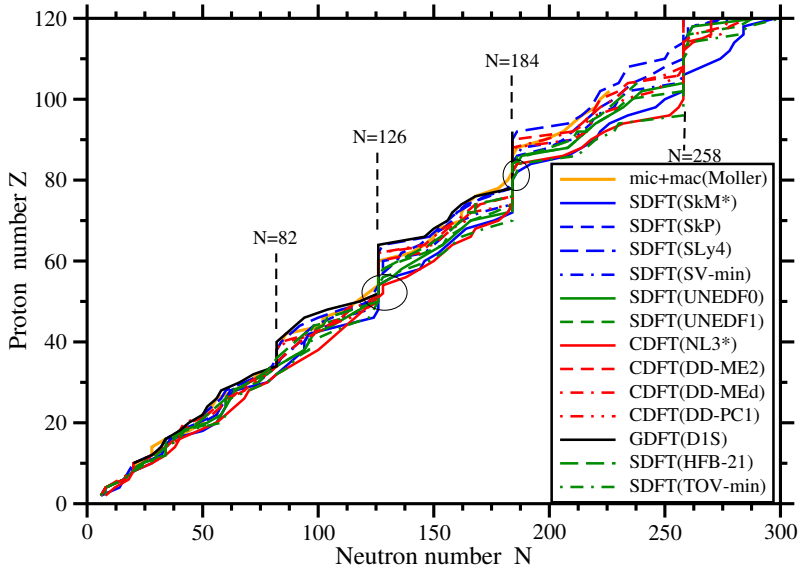

Figure 3.9

Two-neutron drip-lines obtained in state-of-the-art DFT calculations. The regions of well defined localization of the two-neutron drip-line are encircled.

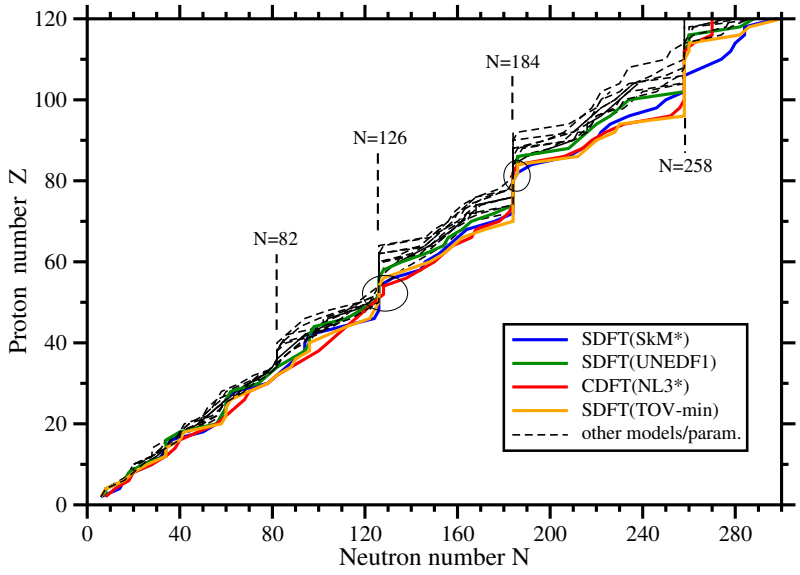

Figure 3.10

The same as in Fig. 3.9 but with the four most neutron-rich two-neutron drip lines shown in color and the rest in black.

The question whether there exist correlations between the position of the two-neutron drip line and its nuclear matter properties for a given EDF could be asked. With that goal Fig. 3.10 shows the four most neutron-rich two-neutron drip lines amongst the 14 compiled lines. The nuclear matter properties of the corresponding EDF's are shown in Table 3.2. Considering the EDF's NL3* which leads to the most neutron-rich two-neutron drip lines amongst the relativistic functionals, it is tempting to associate the difference in the position of the two-neutron drip lines with different symmetry energies. But a detailed comparison of the position of the 14 two-neutron drip lines presented in Figs. 3.9, and 3.10 with nuclear matter properties of their EDF's (Table 3.2) does not reveal clear correlations between the location of the two-neutron drip line and the nuclear matter properties of the

corresponding functional. For nuclei close to the neutron drip line the Fermi surface is very small and negative close to the continuum limit and it changes only slowly with the neutron number. The precise position of the drip line therefore depends very much on the behavior of the tail of the neutron density. At these very low densities the properties J and L of the nuclear matter at saturation in not really relevant.

The possible sources of the uncertainties in the position of the two-neutron drip line have been discussed in Ref. [84]. They include the isovector properties of the EDF's [5] and the underlying shell structure connected with inevitable inaccuracies of the single particle energies in the DFT description [84].

The isovector properties of an EDF define the depth of the nucleonic potential with respect to the continuum and may affect the location of two-neutron drip line. However, such uncertainties in the depth of the nucleonic potential exist also in known nuclei (see discussion in Sect. IVC of Ref. [103]). They cannot describe the observed features completely.

The shell structure effects are clearly visible in the fact that for some combinations of Z and N there is basically no (or very little) dependence of the predicted location of the two-neutron drip line on the CEDF. Such a weak dependence, seen in all model calculations, is especially pronounced at spherical neutron shell closures with $N = 126$ and 184 around the proton numbers $Z = 54$ and 80, respectively. In addition, a similar situation is seen in the CDFT calculations at $N = 258$ and $Z \sim 110$. This fact is easy to understand because of the large neutron shell gap at the magic neutron numbers in all DFT's.

Inaccuracies in the DFT description of single particle energies [53, 103] also contribute to increasing uncertainties in the prediction of two-neutron drip line position on moving away from these spherical shell closures. The comparison of Figs. 3.9 and 3.11, shows that there is a close correlation between the nuclear deformation at the neutron-drip line and the uncertainties in their prediction. The regions of large uncertainties corresponds to transitional and deformed nuclei. Again this is caused by the underlying level densities of the single-particle states. The spherical nuclei under discussion are characterized by large shell gaps and a clustering of highly degenerate single-particle states around them. Deformation removes this high degeneracy of single-particle states and leads to a more equal distribution of the single-particle states with energy. Moreover, the density of bound neutron single-particle states close to the neutron continuum is substantially larger than that on the proton-drip line which leads to a small slope of two-neutron separation energies S_{2n} as a function of neutron number in the vicinity of two-neutron drip line for medium and heavy mass nuclei (see Fig. 3.5). The S_{2n} and S_{2p} values are described with a similar accuracy in the various parameterizations (Table 3.1). However, the difference in the slope of S_{2n} and S_{2p} as a function of proton and neutron numbers translates into much larger uncertainties in the definition of the position of two-neutron drip line as compared with two-proton drip line. This also indicates that the predictions for the two-neutron drip line depend more sensitively on the single-particle energies than those for two-proton drip line. The uncertainties in the definition of the two-neutron drip lines obtained with the CDFT and SDFT are shown in Fig. 3.8.

Table 3.2

Properties of symmetric nuclear matter at saturation for the EDFs used in Fig.3.9.

Parameter	ρ_0 [fm^{-3}]	$(E/A)_\infty$ [MeV]	K [MeV]	J [MeV]	L_0 [MeV]	m*/m
four most neutron-rich two-neutron drip lines						
NL3* [33]	0.150	-16.31	258	38.68	122.6	0.67
SkM* [104, 3]	0.160	-15.77	217	30.03	45.8	0.79
UNEDF1 [105]	0.159	-15.80	220	28.99	40.0	0.99
TOV-min [102]	0.161	-15.93	222	32.30	76.0	0.94
remaining parametrizations (drip-lines in the middle)						
mic+mac [FRDM] [6]		-16.25	240	32.73		1.00
DD-ME2 [26]	0.152	-16.14	251	32.40	49.4	0.66
SLy4 [106, 3]	0.160	-15.97	230	32.00	45.9	0.69
D1S [Gogny] [107]	0.160	-15.90	210	32.00		0.70
UNEDF0 [105]	0.161	-16.06	230	30.54	45.1	0.90
DD-MEδ [28]	0.152	-16.12	219	32.35	52.9	0.61
SkP [108, 3]	0.163	-15.95	201	30.00	19.7	1.00
SV-min [109, 3]	0.161	-15.91	222	30.66	44.8	0.95
DD-PC1 [27, 79]	0.152	-16.06	230	33.00	68.4	0.66
HFB-21 [BSk21] [110]	0.158	-16.05	246	30.00	46.6	0.80

In Table 3.2 we list the density ρ_0 , the energy per particle (E/A_∞), the incompressibility K_∞, the symmetry energy J and its slope L_0, and the isoscalar effective masses m^*/m of a nucleon at the Fermi surface for the energy density functionals used in Fig. 3.9. In the relativistic cases we show the Lorentz effective masses [2]. The results of the compilation [3] is used for the Skyrme functionals when possible.

Table 3.3: Two-proton and two-neutron drip lines.

Proton	**Two proton drip-line**			**Two neutron drip-line**		
number Z	NL3*	DD-MEδ	DD-PC1	NL3*	DD-MEδ	DD-PC1
2	2	2	2	8	6	6
4	4	2	2	12	8	8
6	4	4	4	18	14	16
8	4	4	4	20	20	20
10	8	8	8	28	20	24
12	8	8	8	34	28	28
14	8	10	10	38	34	34
16	10	12	10	40	40	40

Continued on next page

Table 3.3 – Continued from previous page

Proton	**Two proton drip-line**			**Two neutron drip-line**		
number Z	NL3*	DD-MEδ	DD-PC1	NL3*	DD-MEδ	DD-PC1
18	12	14	12	48	40	40
20	14	14	14	56	42	48
22	18	18	18	60	52	52
24	20	20	20	64	56	56
26	20	22	20	68	60	62
28	22	22	22	70	68	68
30	26	26	26	78	70	72
32	28	28	28	82	76	78
34	30	30	30	88	82	82
36	32	32	32	94	82	82
38	34	34	34	100	82	82
40	36	36	36	104	84	86
42	38	40	38	108	96	100
44	42	42	42	112	102	104
46	44	44	44	116	110	114
48	46	46	46	120	114	120
50	48	48	48	124	122	126
52	56	54	54	128	126	126
54	56	56	56	128	126	126
56	58	58	60	138	126	126
58	60	60	60	144	126	126
60	62	64	62	150	126	126
62	66	66	66	154	126*	126*
64	68	70	70	158	146	150
66	70	72	72	166	150	154
68	74	76	76	168	154	158
70	78	78	78	178	160	164
72	80	82	80	182	164	166
74	80	84	84	184	168*	184
76	84	88	86	184	184	184
78	88	90	90	184	184	184
80	90	92	92	184	184	184
82	94	96	94	184	184	184
84	104	104	104	186	184	184
86	106	106	108	206	184	184
88	108	110	110	214	184	184*
90	112	114	116	218	198*	210
92	118	118	120	224	210	216
94	122	126	126	232	216	218

Continued on next page

Table 3.3 – Continued from previous page

Proton	**Two proton drip-line**			**Two neutron drip-line**		
number Z	NL3*	DD-MEδ	DD-PC1	NL3*	DD-MEδ	DD-PC1
96	126	130	130	252	218	220
98	130	132	130	256	222	230
100	132	134	134	258	228	232
102	134	136	136	258	232	246
104	138	140	142	258	236	250
106	142	144	144	258	250	256
108	146	148	150	258	258	258
110	150	152	154	258	258	258
112	154	156	158	258	258	258
114	158	160	162	262	258	258
116	162	164	166	270	262	274
118	166	168	172	270	276	278
120	170	172	172	270	278	286

Table 3.3 list the two-proton and two-neutron drip lines predicted by the NL3*, DD-MEδ, and DD-PC1. An asterisk at a neutron number at the two-neutron drip line indicates isotope chains with additional two-neutron binding at higher N-values (peninsulas).

3.7 Deformations

The solution of the variational equations of density functional theory yields values for the single particle density $\rho(r)$. Therefore, density functional theory not only allows us to derive the binding energies of the system but in addition all quantities depending on $\rho(r)$. In this section we consider the charge quadrupole moment:

$$Q_{20} \quad = \quad \int d^3r \rho(r) \, (2z^2 - r_\perp^2), \tag{3.4}$$

with $r_\perp^2 = x^2 + y^2$. This value can be directly compared with experimental data. However, it is more convenient to transform this quantity into dimensionless deformation parameter β_2:

$$Q_{20} = 2\sqrt{\frac{4\pi}{5}}\frac{3}{4\pi}ZR_0^2\beta_2 \tag{3.5}$$

where $R_0 = 1.2A^{1/3}$. Eq. (3.5) is used also in the extraction of experimental β_2 deformation from measured data [111]. This justifies its application despite the fact that this simple linear expression ignores the contributions of higher power/multipolarity deformations to the charge quadrupole moment.

Fig. 3.11 shows the distribution of proton quadrupole β_2 deformations in the (N, Z) plane for the CEDF DD-PC1. Similar figures has been done for NL3*, DD-MEδ and DD-ME2 (see [40]) and the results are almost the same in all the four CEDF's under consideration.

Direct experimental information on the deformations of nuclei can be obtained from Coulomb excitation and lifetime measurements [111]. An alternative method is to derive a quadrupole moment from the $2^+ \rightarrow 0^+$ transition energy by using the Grodzins relation [112] or its later refinements [113]. However, these prescriptions are applicable only to well deformed nuclei. In general, it is estimated that experimental methods give an accuracy of around 10% [113] for the static charge quadrupole deformation β_2 in the case of well deformed nuclei. The error can be larger in transitional nuclei since in this case the deformation extracted from experimental data will contain also dynamic deformation resulting from zero-point oscillations of the nuclear surface in the ground state [114].

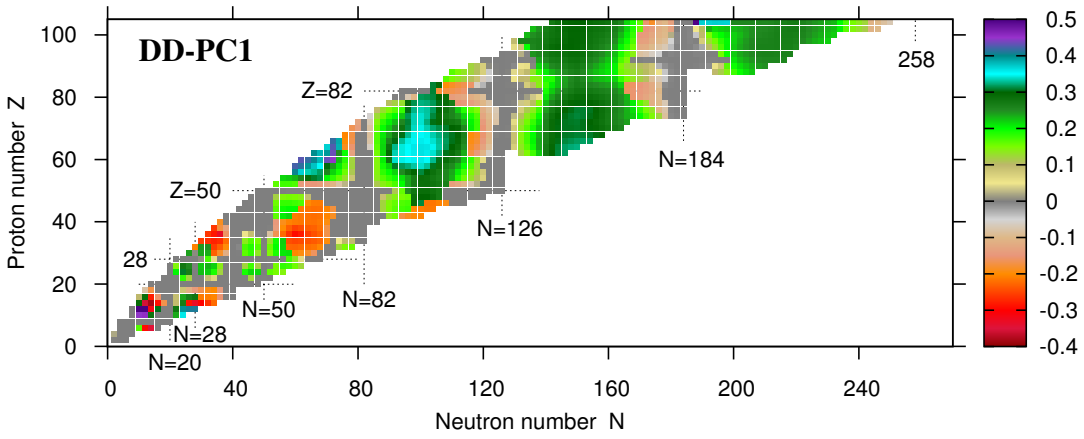

Figure 3.11

Charge quadrupole deformations β_2 obtained in the RHB calculations with DD-PC1.

These considerations limit the possibilities of a comparison between calculated and experimental β_2 deformations to the well-deformed nuclei in the rare-earth and actinide regions. Although deformation exists also in the ground states of nuclei in many other regions, the potential energy surfaces of these nuclei are, in general, soft in β_2 or γ-deformation, leading to the phenomena of shape fluctuations, shape coexistence [115] and quantum phase transitions [116]. For such situations, the mean field description is not completely adequate, and, thus, a comparison between theoretical and experimental deformation properties is not conclusive.

A systematic comparison between calculated and experimental static charge quadrupole deformations β_2 has already been performed in each of these regions (with NL3* [54] in the actinides and DD-PC1 [27] in the rare-earth region). They describe the experimental data well, typically within the experimental uncertainties. Fig. 3.12 shows that in these regions of well deformed nuclei the spread of the theoretical predictions, i.e. the differ-

ence between results obtained with various CEDF's, is rather small for static quadrupole deformations β_2.

The width of the gray region in Fig. 3.11 along a specific magic number corresponding to a shell closure indicates the impact of this shell closure on the structure of the neighboring nuclei. The effect of a single gap is more quantifiable away from these nuclei. One can see in Fig. 3.11 that the neutron $N = 82$, 126 and 184 shell gaps have a more pronounced effect on the nuclear deformations as compared with the proton shell gaps at $Z = 50$ and $Z = 82$.

The comparison of Fig. 3.11 with HFB results based on the Gogny D1S force in Fig. 3a of Ref. [7], with HFB results based on six Skyrme EDF's in Fig. 2 of the Supplement to Ref. [5], and with the microscopic+macroscopic model in Fig. 9 of Ref. [6] shows that the general structure of the distribution of charge quadrupole deformations β_2 in the nuclear chart is similar in all model calculations. Differences between models emerge mostly at the boundaries between the regions of different types of deformation, i.e. in the transitional regions, where the energy surfaces are rather flat and static deformations are not well defined. This comparison also reveals that, similar to our relativistic results, also in non-relativistic calculations the neutron shell gaps with $N = 82$, 126 and 184 have a more pronounced effect on the nuclear deformations than the proton shell gaps with $Z = 50$ and $Z = 82$.

Figure 3.12 shows the spreads $\Delta\beta_2(Z, N)$ among four CEDF's for the predicted charge quadrupole deformations. It can be seen that this spread is either non-existent or very small for spherical or nearly spherical nuclei as well as for well-deformed nuclei in the rare-earth

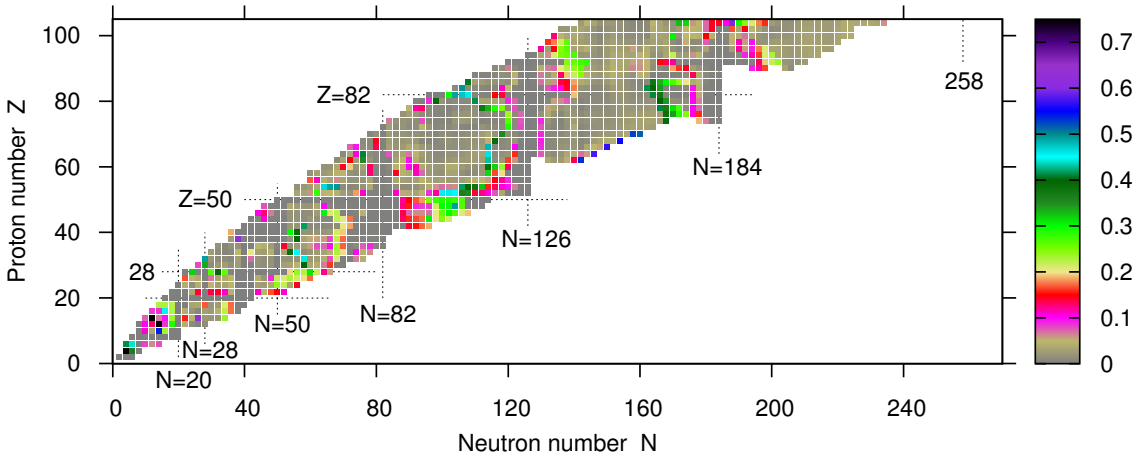

Figure 3.12

Proton quadrupole deformation spreads $\Delta\beta_2(Z,N)$ as a function of proton and neutron number.

and actinide region. The largest uncertainties for predicting the equilibrium quadrupole deformations exist at the boundaries between regions of different deformations. Correlations going beyond mean field have to be taken into account [98, 117, 94, 100] and shape fluctuations do not allow a precise definition of deformation parameters. However, even if such correlations and fluctuations are taken into account properly by methods based on density functional theory and going beyond the mean field, there remain deficiencies of the current generations of the DFT models with respect of the description of single-particle energies [98]. When we compare the profile of the potential energy surface (PES) as a function of the deformation in spherical or well-deformed nuclei with that in transitional nuclei, we find that this profile depends for transitional nuclei much more sensitively on the underlying single-particle structure than in the other two cases. However, it is well known that the single-particle energies (both spherical and deformed) are not very accurately described at

the DFT level (see Refs. [103, 53]). Considering that the PES's obtained at the mean field level form the starting points of many beyond mean field calculations, further improvement in the description of the single-particle energies is needed in order to describe experimental data in transitional and shape-coexistent nuclei reliably and consistently across the nuclear chart.

3.8 Charge radii and neutron skin thickness.

The charge radii were calculated from the corresponding point proton radii as

$$r_{ch} = \sqrt{< r^2 >_p + 0.64} \ \ \mathrm{fm} \tag{3.6}$$

where the factor 0.64 accounts for the finite-size effects of the proton. We neglected the small contributions to the charge radius originating from the electric neutron form factor and the electromagnetic spin-orbit coupling [118, 119] as well as the corrections due to the center of mass motion.

The accuracy of the description of charge radii is illustrated on the example of the CEDF DD-PC1 in Fig. 3.13. Black, red, green, orange and blue colors are used for isotope chains with proton numbers ending with 2, 4, 6, 8 and 0 respectively. The experimental data are taken from Ref. [8]. Panels (b), (c) and (d) show the comparison in an enlarged scale. We do not present such a comparison for the CEDF's NL3* and DD-MEδ because they show very similar results. This similarity is clearly seen from Fig. 3.14, which presents the spreads (Eq. 3.1) in the theoretical results on charge radii, and from Table 3.4, which presents the rms-deviations between calculated and experimental radii. These comparisons

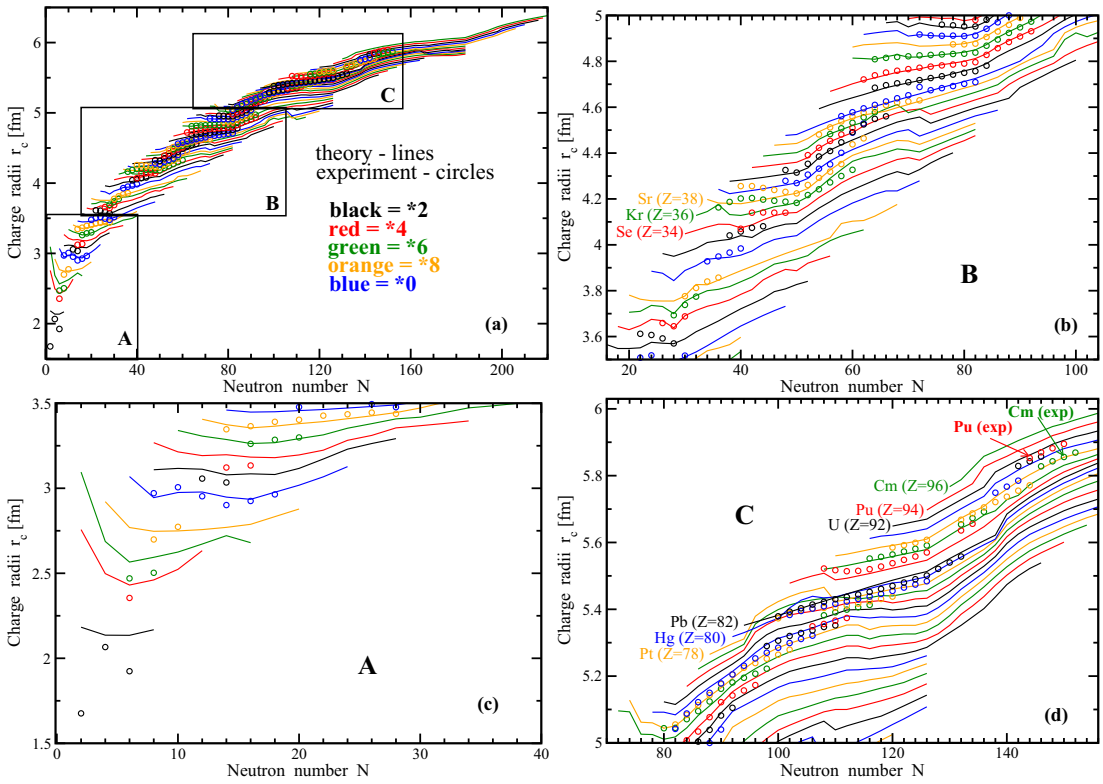

Figure 3.13

Experimental and theoretical charge radii as a function of neutron number.

are based on the latest compilation of experimental charge radii in Ref. [8], which includes charge radii for 351 even-even nuclei.

The calculations provide in general a good description of experimental data. However, there are four exceptions. First, there are very light nuclei He, Be and C (Fig. 3.13b), where the mean field description has obviously limitations. The discrepancy between theory and experiment is especially pronounced in the case of the He nuclei. Then, there is a substantial discrepancy between theory and experiment for charge radii of Se, Kr and Sr isotopes at neutron numbers $N = 38 - 46$ (see Fig. 3.13c). The calculated ground state quadrupole deformations of these nuclei are predicted to be either spherical or near-spherical (see Fig. 3.11). However, the potential energy surfaces are soft. This indicates that a proper description of their structure requires the inclusion of beyond mean field correlations. Next, the ground states of some proton-rich Hg and Pb isotopes are predicted to be oblate (or prolate) in contradiction with experiment. These earlier observed features [120] are in part due to incorrect position of the proton $1h_{9/2}$ spherical subshell [120, 52] and they are present in all the CEDF's used here. When comparing theory with experiment we use for these nuclei the radii from the minimum of the potential energy surface corresponding to the experimental minimum, i.e. the spherical minimum for the $N = 104 - 114$ Pb isotopes and the oblate minimum for the $N = 100 - 108$ Hg isotopes. Finally, the last case is related to the unusual behavior of the charge radii in the U-Pu-Cm isotopes (see Fig. 3.13d). For a fixed neutron number, the increase of proton number leads in these isotopes to an increase of the calculated charge radius. Such a feature is seen not only for the CDFT results, but also for the results of the non-relativistic DFT calculations based on the Gogny D1S force

(see supplement to Ref. [7]). However, in experiment the charge radii of the Cm ($Z = 96$) nuclei are lower than those of Pu ($Z = 94$) and U ($Z = 92$). This is the only case in the nuclear chart where such an inversion exists. Considering that both the ground state quadrupole deformations are very stable in this region, it is impossible based on the current CDFT's and on the Gogny functional D1S to understand this highly unusual behavior of experimental charge radii in the Cm isotopes.

Table 3.4

The rms-deviations $\Delta r_{ch}^{\rm rms}$ between calculated and experimental charge radii.

CEDF	$\Delta r_{ch}^{\rm rms}$ [fm]	$\Delta r_{ch}^{\rm rms}$ [fm]
1	2	3
NL3*	0.0407	0.0283
DD-ME2	0.0376	0.0230
DD-MEδ	0.0412	0.0329
DD-PC1	0.0402	0.0253

Table 3.4 list the rms-deviations $\Delta r_{ch}^{\rm rms}$ between calculated and experimental charge radii. They are given in fm for the indicated CEDF's. For the calculations of the rms-values, all experimental data are used in column 2, while the data on radii of He ($Z = 2$) and Cm ($Z = 96$) isotopes are excluded in column 3. See text for the discussion of these cases.

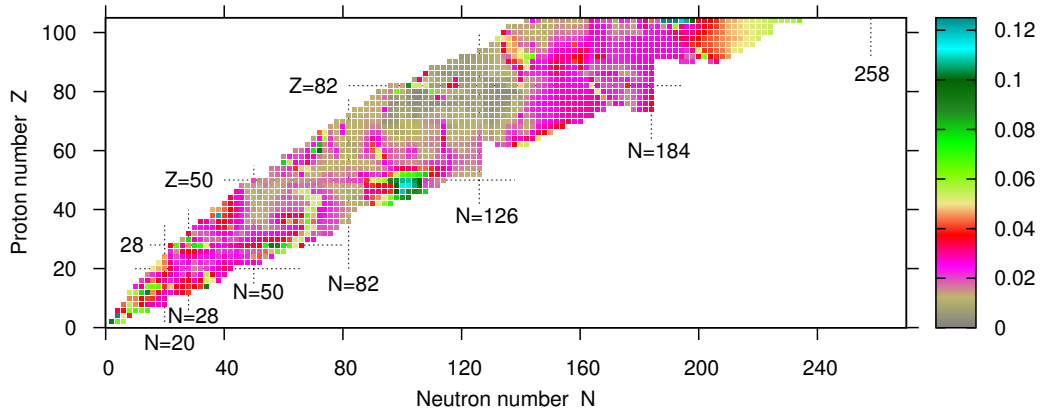

Figure 3.14

Charge radii spread $\Delta r_{\rm ch}(Z,N)$ as a function of proton and neutron number.

In neutron-rich nuclei the excess of neutrons over protons creates a neutron skin. The neutron skin thickness is commonly defined as the difference of proton and neutron root-mean-square (rms) radii

$$r_{\rm skin} = < r_n^2 >^{1/2} - < r_p^2 >^{1/2} . \tag{3.7}$$

The neutron skin thickness is an important indicator of isovector properties. It is closely related with a number of observables in finite nuclei which are sensitive to isovector properties [121, 64, 122] and it affects the physics of neutron stars [123, 124, 64, 125].

The experimental data on the neutron skin thickness in ^{208}Pb is contradictory. There is a large set of experiments which suggests that the neutron skin is around 0.2 fm or slightly smaller (see Table 1 in Ref. [126]). However, these experimental data are extracted in model dependent ways (see Ref. [127] and references quoted therein). The neutron skin thicknesses $r_{\rm skin} = 0.161 \pm 0.042$ [126] and $r_{\rm skin} = 0.190 \pm 0.028$ [128] obtained recently

Table 3.5

Neutron skin thicknesses $r_{\rm skin}$ in ^{48}Ca and ^{208}Pb obtained in calculations with the indicated CEDF's.

CEDF	$r_{skin}(^{48}\text{Ca})$ [fm]	$r_{skin}(^{208}\text{Pb})$ [fm]
NL3*	0.236	0.288
DD-ME2	0.187	0.193
DD-MEδ	0.177	0.186
DD-PC1	0.198	0.201

from the energy of the anti-analogue giant dipole resonance rely on relativistic proton-neutron quasiparticle random-phase approximation calculations based on the RHB model. Another recent value of the neutron skin thickness of $r_{\rm skin} = 0.15 \pm 0.03({\rm stat})^{+0.01}_{-0.03}({\rm sys})$ fm has been extracted from coherent pion photo-production cross sections [129]. However, the extraction of information on the nucleon density distribution depends on the comparison of the measured (γ, π^0) cross sections with model calculations. On the other hand, a measurement using an electro-weak probe has very recently been carried out in parity violating electron scattering on nuclei (PREX) [130]. It utilizes the preferential coupling of the exchanged weak boson to neutrons. The electro-weak probe has the advantage over experiments using hadronic probes that it allows a nearly model-independent extraction of the neutron radius that is independent of most strong interaction uncertainties [131]. However, a first measurement at a single momentum transfer gave $r_{\rm skin} = 0.33 \pm 0.17$ with a relatively large error bar [130]. A central value of 0.33 fm is particularly intriguing since it is around 0.13 fm higher than central values obtained in other experiments (see Table 1 in Ref. [126]). The analysis performed in Ref. [132] has found no compelling reason to rule

out the models with large neutron skin in ^{208}Pb. However, as indicated in Ref. [132], the parameters of these models do not follow from a strict optimization procedure. All systematic fits with density dependent couplings in the isovector channel for DD-ME1 [41], DD-ME2 [26], DD-MEδ [28] and DD-PC1 [27] find for the neutron skin thickness in ^{208}Pb values close to 0.2 fm (see Table 3.5). Only in the first two cases the small neutron skins have been used in the fit. For the CEDF's DD-MEδ and DD-PC1 the density dependence in the isovector channel has been determined from ab-initio calculations of nuclear matter.

It is clear that the already approved follow-up PREX measurement [133] designed to achieve the original 1% error in the neutron radius of ^{208}Pb will provide useful constraints on the selection of the proper CEDF. Table 3.5 also provides the predictions for neutron skin thickness in ^{48}Ca. It will also be measured in the approved CREX experiment at JLab with an accuracy of around 0.02 fm [133].

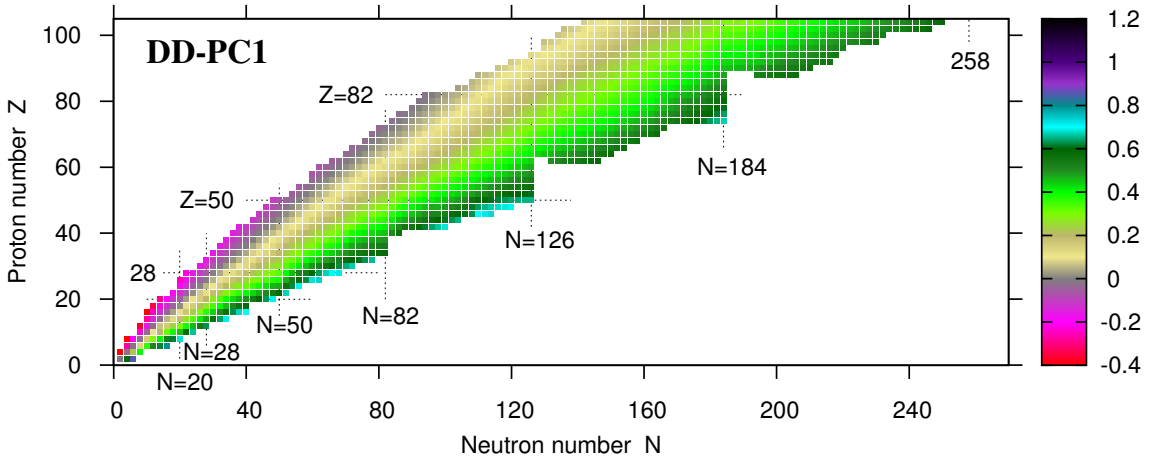

Figure 3.15

Neutron skin thicknesses obtained in RHB calculations with DD-PC1.

On going to the neutron-drip line we observe the same trends which are already seen in ^{48}Ca and ^{208}Pb (see Table 3.5). First, the neutron skin thicknesses obtained with DD CEDF's cluster are around the same value. Second, the neutron skin thickness obtained with NL3* exceeds substantially those found with DD CEDF's. It is interesting that the neutron skin thicknesses obtained with DD CEDF's are very close to those found in Skyrme DFT's calculations with SV-min and UNEDF0 in Ref. [66].

In Fig. 3.15 we present calculated distributions of neutron skin thicknesses in the (Z, N) chart with DD-PC1. Similar distributions are presented for NL3*, DD-ME2 and DD-MEδ in Ref [40]. These results are similar for the DD CEDF's, and on the other side, the neutron skin thickness is larger for NL3*. This is a consequence of two factors. First, the neutron skin is larger for NL3* than for the DD CEDF's already in the valley of beta-stability and the neutron skin thickness increases with isospin. Second, the two-neutron drip line extends to more neutron-rich nuclei in NL3* as compared with DD CEDF's leading to these high values of $r_{\rm skin}$.

As shown in Fig. 3.16 the spreads (Eq. 3.1) of theoretical predictions in the neutron skin thickness increase with isospin and become rather large in neutron-rich nuclei (reaching 0.25 fm in some cases). They are larger than those found in Skyrme calculations in Ref. [66]. This is a consequence of the use of NL3*, which contrary to DD CEDF's and the Skyrme EDF's used in Ref. [66], favors large neutron skins. This again stresses the importance of future PREX-II and CREX experiments. If PREX-II confirms the large neutron skin in ^{208}Pb ($r_{\rm skin} \sim 0.33$ fm) obtained in the first PREX experiment, this would also require to look for density dependent CEDF's and Skyrme EDF's with larger neutron

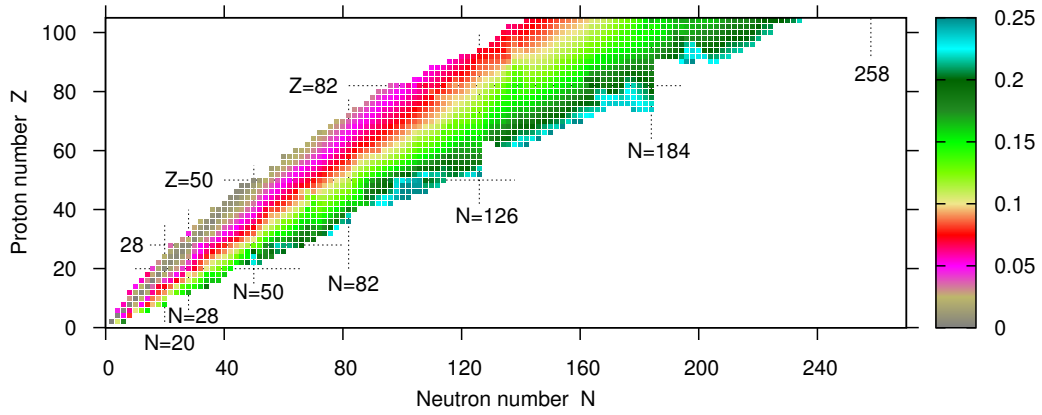

Figure 3.16

Neutron skin thickness spreads $\Delta r_{\rm skin}(Z,N)$ as a function of proton and neutron number.

skins. If this experiment will lead to a smaller neutron skin thickness $r_{\rm skin} \sim 0.2$ fm, then the EDF's with large neutron skins (such as NL3*) should be excluded from further consideration. In either case, this experiment will lead to a reduction of the uncertainty in the prediction of neutron skins in neutron-rich nuclei.

3.9 Concluding remarks.

The global performance of covariant energy density functionals has been assessed investigating the state-of-the-art functionals NL3*, DD-ME2, DD-MEδ, and DD-PC1. They represent three classes of functionals which differ by basic model assumptions and fitting protocols. The available experimental data on ground state properties of even-even nuclei have been confronted with the results of the calculations. For the first time, theoretical systematic uncertainties in the prediction of physical observables (as defined in Eq. (3.1))

have been investigated on a global scale for relativistic functionals. Special attention has been paid to the propagation of these uncertainties towards the neutron-drip line.

The main results can be summarized as follows:

- The current generation of CEDF's investigated in this chapter of the dissertation provides an improved description of masses across the nuclear chart as compared with the previous generation. This leads not only to reduced global rms deviations but also to improved gross trends of the deviations between theory and experiment as a function of the mass number. The spread for binding energies increases on going from the beta-stability valley towards the neutron-drip line. This is a consequence of poorly defined isovector properties of the current generation of CEDF's.

- The analysis of discrepancies between theory and experiment for two-neutron separation energies and their sources leads to a more critical look on the reappearance of two-neutron binding with increasing neutron number beyond the primary two-neutron drip line. This reappearance shows itself in the nuclear chart via peninsulas emerging from the nuclear mainland and it is directly related to the behavior of two-neutron separation S_{2n} energies with neutron number.

- The calculated two-proton drip lines are very close to experiment. The best reproduction of the two-proton drip line is achieved with DD-MEδ, which is characterized by the best residuals for the two-proton separation energies S_{2p}. Since the proton-drip line lies close to the valley of stability, the extrapolation errors towards it are small. In addition, the Coulomb barrier provides a rather steep potential reducing

considerably the coupling to the proton continuum. This leads to a relatively low density of the single-particle states in the vicinity of the Fermi level, which helps to minimize the errors in the prediction of two-proton drip line.

- A detailed analysis of the sources of the spread in the predictions of the two-neutron drip lines existing in non-relativistic and covariant DFT has been performed. Poorly known isovector properties of the EDF's, the underlying shell structure and inevitable inaccuracies in the DFT description of the single-particle energies contribute to these uncertainties.

- The experimental static β_2 deformations of well-deformed nuclei are well described in these calculations. The difference between the four CEDF's is small and within the experimental uncertainties. As a result, such experimental data cannot be used to differentiate between the functionals. Theoretical uncertainties for this physical observable are either non-existent or very small for spherical or nearly spherical nuclei as well as for well-deformed nuclei in the rare-earth and in the actinide regions. The largest spreads for predicting the equilibrium quadrupole deformations exist at the boundaries between regions of different deformations.

- A comparable level of accuracy is achieved by all the functionals under investigation for charge radii. Fig. 3.14 shows that the spread in predicting charge radii are not necessarily larger near the neutron drip line as compared with the valley of beta-stability.

- The experimental data on the neutron skin thickness $r_{\rm skin}$ in ^{208}Pb is somewhat contradictory. Hadronic probes give $r_{\rm skin} \sim 0.2$ fm, whereas in the PREX experiment the electro-weak probe provides a central value of $r_{\rm skin} = 0.3$ fm, however with very large error bars. The NL3* results come close to the central PREX value, while DD-MEδ and DD-PC1 give much smaller neutron skins in the vicinity of $r_{\rm skin} = 0.2$ fm.

The current investigation shows that the biggest uncertainties in theoretical description exist in transitional nuclei. On the one hand, this is expected since these nuclei have usually flat potential energy surfaces, often in the β- and γ-directions. The minima are not well defined in these flat energy surfaces and the fluctuations cannot be neglected. These nuclei have to be treated by the methods going beyond mean field [134, 96, 100]. On the other hand, the mean field is the starting point of these approaches. However, in some specific cases we find a strong dependence of the equilibrium deformations and the potential energy surfaces of transitional and shape-coexistent nuclei on the employed EDF which originates from the deficiencies of mean field methods in the description of single-particle energies.

CHAPTER IV

NEUTRON DRIP LINE: SINGLE-PARTICLE DEGREES OF FREEDOM AND PAIRING PROPERTIES AS SOURCES OF THEORETICAL UNCERTAINTIES

4.1 Introduction

The analysis of theoretical uncertainties in the prediction of the position of the two-neutron and two-proton drip-lines has recently attracted great interest (chapter III and Ref [5, 84, 40]) because of the possibility to estimate the number of nuclei which may exist in nature. Fig. 4.1 shows the theoretical uncertainties in the definition of the position of the two-proton and two-neutron drip lines which emerge from an analysis performed in the framework of covariant density functional theory (CDFT) [43, 29] using four state-of-the-art covariant energy density functionals (CEDF's). The uncertainties in the location of the two-proton and two-neutron drip lines are shown by violet shaded areas. They are defined by the extremes of the predictions of the corresponding drip lines obtained with different functionals. The uncertainties (the range of nuclei) in the location of the neutron chemical potential $\lambda_n = -2.0$ MeV are shown by the blue shaded area. Experimentally known stable and radioactive nuclei (including proton emitters) are shown by black and green squares, respectively. The green solid line shows the limits of the nuclear chart (defined as fission yield greater than 10^{-6}) which may be achieved with dedicated existence measurements at FRIB [9]. Red solid circles show the nuclei near the neutron drip line for

which the single-particle properties are studied in Sect. 4.4. The detailed comparison of these results has already been discussed in chapter III and Refs [84, 40].

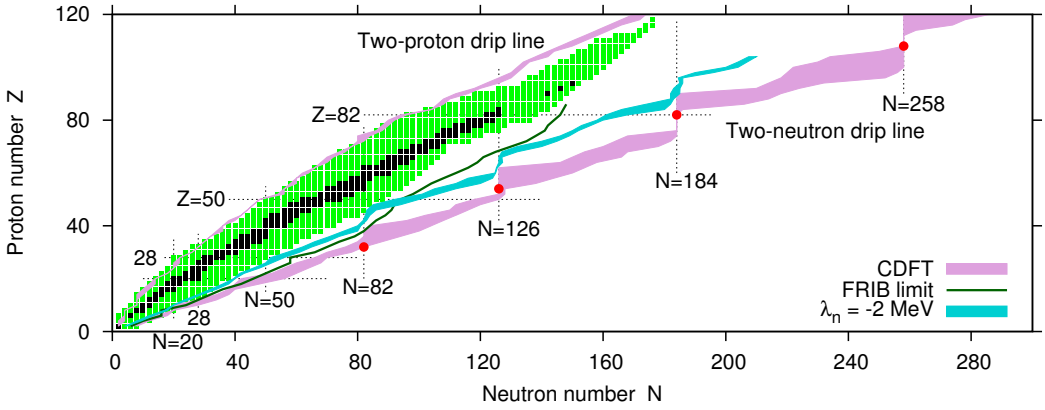

Figure 4.1

The uncertainties in the location of the two-proton and two-neutron drip lines.

As already stated in chapter III, the largest uncertainties exist in the position of the two-neutron drip line. Several sources have been proposed for these uncertainties, but they have not been investigated in detail before our studies. The sources of the uncertainties in the prediction of the neutron drip line are as follows:

- The uncertainties in the definition of the isovector properties of the EDF's (see chapter III and [5]). The isovector properties of an EDF impact the depth of the nucleonic potential with respect to the continuum and, thus, may affect the location of the two-neutron drip line. However, an inaccurate reproduction of the depth of the nucleonic potential exists in modern EDF's also in known nuclei (see the discussion in Sect. IVC of Ref. [103]). Thus, they alone cannot explain the observed features.

- The sensitive of the underlying shell structure and the accuracy of the description of the single-particle energies Ref. [84]. No detailed study has been performed of this aspect of the problem before our studies.

- The impact of pairing and it strength on the position of the two-neutron dripline [135, 136].

The goal of this chapter is to investigate the impact of pairing correlations and the underlying shell structure on the position of the two-neutron drip line and to outline the approaches which will allow in future to decrease theoretical uncertainties in the definition of two-neutron drip lines. Only the *systematic* uncertainties is discuss and not the *statistical errors* which can be calculated from a statistical analysis during the fit [65].

4.2 Pairing properties: a global view

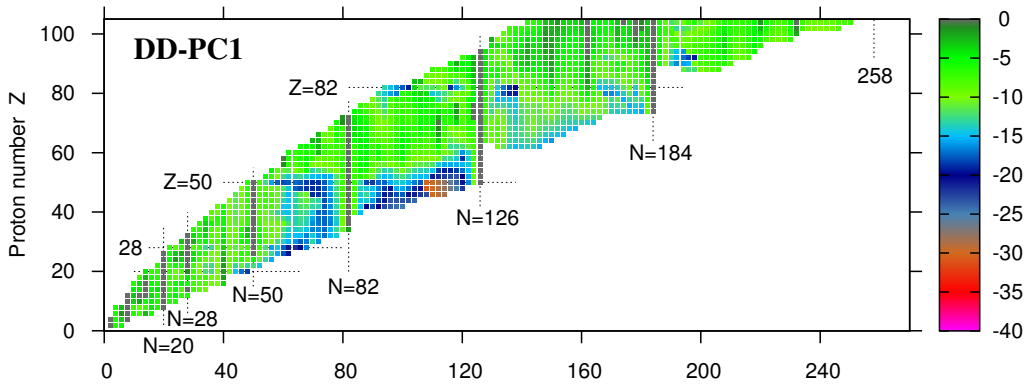

Figure 4.2

Neutron pairing energies E_{pairing} obtained in the RHB calculations with DD-PC1 CEDF.

Fig. 4.2 shows the neutron pairing energies $E_{\rm pairing}$ obtained with DD-PC1 CEDF. In the region of known nuclei these energies are, in general comparable. They are very similar in the RHB calculations with the three CEDF's DD-ME2, DD-MEδ and DD-PC1 and slightly higher (in absolute values) with the NL3* CEDF (see [137] for more details). On approaching the two-neutron drip line, substantial differences develop between the pairing energies. The largest increase of neutron pairing energies is seen near the two-neutron drip line between $N = 50$ and $N = 126$, for other nuclei in the vicinity of two-neutron drip line this increase is more modest(see Fig. 4.2).

Fig. 4.3 shows the evolution of the neutron pairing gaps $\Delta_{\rm uv}$ and pairing energies $E_{\rm pairing}$ of the Yb nuclei located between the two-proton and two-neutron drip-lines obtained in the axial RHB calculations with the indicated CEDF's. The shaded yellow area indicates experimentally known nuclei. The 'DD-PC1(scaled)' curves show the results of the calculations in which the pairing strength is increased by 3.5%. It can be seen in this figure that the RHB calculations with the three density dependent sets DD-MEδ, DD-ME2 and DD-PC1 the pairing gaps $\Delta_{\rm uv}$ in neutron-rich $N \geq 126$ nuclei have on average the same magnitude as pairing gaps in known nuclei (Fig. 4.3a). However, the absolute pairing energies are larger by a factor of about 2 in neutron-rich nuclei as compared with the ones in known nuclei (Fig. 4.3b). Both $\Delta_{\rm uv}$ and $E_{\rm pairing}$ are more or less constant in neutron-rich nuclei in the RHB calculations with DD-PC1 and DD-MEδ. On the contrary, a slight increase of the absolute values of these quantities is observed with increasing isospin in DD-ME2.

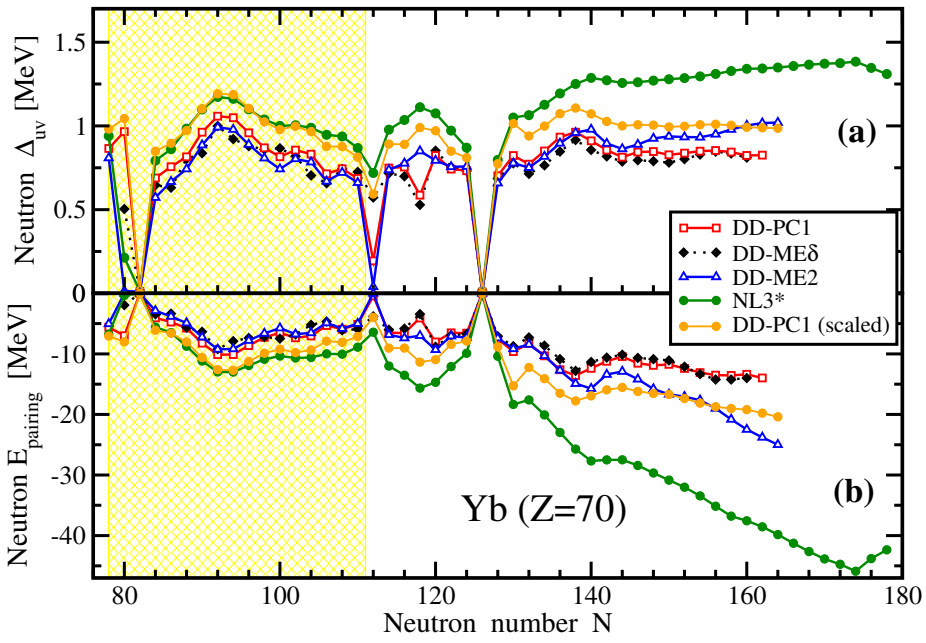

Figure 4.3

Neutron pairing gaps $\Delta_{\rm uv}$ and pairing energies $E_{\rm pairing}$ of Yb nuclei.

The situation is different for the NL3* functional. Its pairing correlations are only slightly stronger in known nuclei as compared with the density dependent CEDF's. However, more pronounced differences are seen when the results in neutron-rich nuclei are compared with the ones in known nuclei. The pairing gaps $\Delta_{\rm uv}$ are on average 25% larger in neutron-rich nuclei as compared with known ones and, in addition, they gradually increase with neutron number. The absolute values of the pairing energies rapidly increase with neutron number in neutron-rich $N \geq 126$ nuclei; near two-neutron drip line these energies are larger by a factor of 4 than average pairing energies in known nuclei.

Considering the existing differences in the $\Delta_{\rm uv}$ and $E_{\rm pairing}$ values obtained in the calculations with different CEDF's in known nuclei (curves in shaded area of Fig. 4.3), it is

important to understand to which extent the minimization of these differences will also remove the differences in these quantities in neutron-rich nuclei. In order to address this question, the calculations with the DD-PC1 CEDF have been performed with a pairing strength increased by 3.5%. In the region of known nuclei, the $\Delta_{\rm uv}$ values obtained in these calculations are on average the same as the ones obtained in the calculations with NL3* CEDF (Fig. 4.3a). The pairing energies are also similar in both calculations (Fig. 4.3b). However, in the region of experimentally known nuclei the isospin dependences of the quantities $\Delta_{\rm uv}$ and $E_{\rm pairing}$ are slightly different in these calculations with NL3* and DD-PC1 CEDF's. These differences increase with isospin; they are especially pronounced near the two-neutron drip line. This effect may be related to different density dependence of these two CEDF's in the isovector channel.

These results have some unpleasant consequences:

- First, even a careful fitting of the pairing force in known nuclei to experimental odd-even mass staggerings will not necessary lead to a pairing force with a reliable predictive power towards the two-neutron drip line. This is because, the $\Delta_{\rm uv}$ and $E_{\rm pairing}$ values obtained in the calculations with the CEDF's NL3* and DD-PC1 (with a scaled pairing strength) differ by $\sim 30\%$ and $\sim 100\%$ in neutron-rich nuclei, respectively, despite the fact that they are more or less similar in known nuclei.

- Secondly, since the form of pairing force is the same in both calculations, the observed differences in the quantities $\Delta_{\rm uv}$ and $E_{\rm pairing}$ have to be traced back to the

underlying shell structure and its evolution with neutron number. As discussed in detail in Sect. 4.4, this is the property most poorly constrained in modern DFT's.

4.3 The impact of pairing properties on the position of two-neutron drip line using Rn isotopes as an example

Knowing that there are differences in the predicted size of pairing correlations for nuclei with large neutron excess, it is important to understand how they affect the physical observables of interest, in particular, the position of the two-neutron drip line. To address this question we analyze the chain of the Rn isotopes with $Z = 86$. The calculations of chapter III and Refs. [84, 40] show that the two-neutron drip line is located in this case at $N = 206$ for NL3* and at $N = 184$ for DD-ME2, DD-MEδ, and DD-PC1 (see Table 3.3 and Table IV in Ref. [40]).

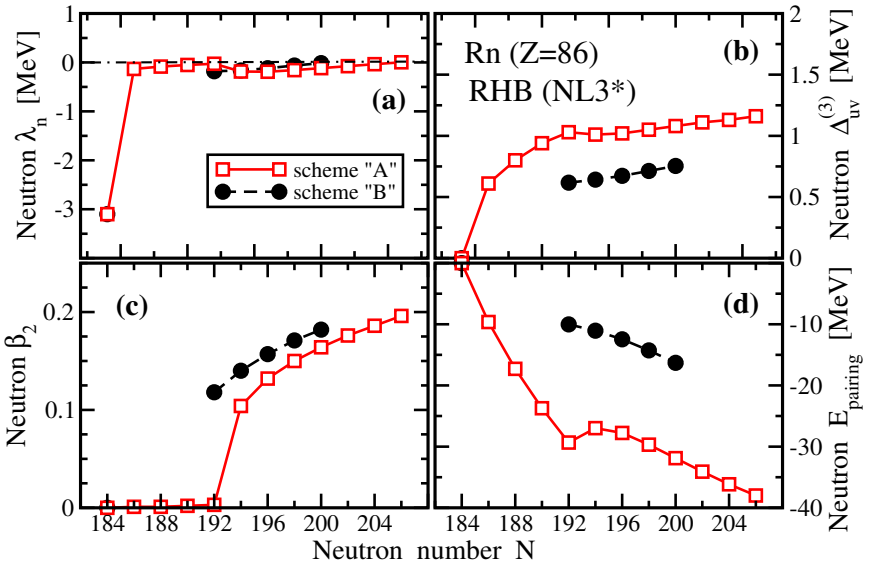

Figure 4.4

The evolution of the λ_n, β_2, $\Delta_{\rm uv}$ and $E_{\rm pairing}$

Figure 4.4 shows the evolution of the neutron chemical potential λ_n (panel (a)), neutron quadrupole deformation β_2 (panel (c)), neutron pairing gap $\Delta_{\rm uv}$ (panel (b)) and neutron pairing energy $E_{\rm pairing}$ (panel (d)) as a function of the neutron number N in the Rn isotopes with $N \geq 184$ obtained in RHB calculations with the CEDF NL3*. Only the results for bound nuclei are shown. The results of the calculations for two values of the strength of the pairing force (Eq. (2.22)) are presented. The calculational scheme labelled "A" corresponds to the pairing force with the scaling factor f defined in Sect. 2.3 of chapter II. The calculational scheme "B" uses a pairing strength reduced by 8% as compared with the scheme "A".

We perform RHB calculations with the CEDF NL3* and with a pairing strength decreased by 8% as compared to the one used in Ref. [40] and chapter III. This brings the calculated pairing energies near the two-neutron drip line close to those obtained in the calculations with DD-ME2, DD-MEδ, and DD-PC1 (Fig. 4.4d). The Rn isotopes with $N = 186$, 188, 190, 202, 204 and 206, which are bound for the original pairing strength (scheme "A"), become unbound for decreased pairing (scheme "B"). Thus, the position of two-neutron drip line located at $N = 206$ is single-valued in calculational scheme A. On the contrary, in the calculational scheme B the creation of the peninsula of stability at $N = 192 - 200$ leads to primary (at $N = 184$) and secondary (at $N = 200$) two-neutron drip lines. In addition, the deformations of the $N = 192 - 200$ isotopes become larger in calculational scheme B (Figs. 4.4c). This reflects the well known fact that pairing typically tries to reduce the nuclear deformation.

However, the situation is more complicated. Larger pairing correlations do not necessarily shift the neutron drip line to larger neutron numbers. When we increase, for instance, in the RHB calculations with DD-ME2 and DD-PC1 the pairing strength by 8%, bringing the calculated pairing energies closer to those for NL3*, this does not affect the position of the two-neutron drip line for the chain of Rn isotopes in these CEDF's because of the details of the underlying shell structure.

The possible impact of pairing correlations on the position of the two-neutron drip line can be understood by the following arguments. The nucleus becomes unbound when the two-neutron separation energy becomes negative. In the majority of the cases it takes place when the neutron chemical potential λ_n becomes positive. In nuclei close to two-neutron drip line pairing correlations scatter neutron pairs from negative energy bound states into positive energy unbound states. As a consequence, the actual position of the neutron chemical potential depends on the energies of the involved levels, their degeneracy and the strength of pairing correlations. In the extreme limit of no pairing, λ_n is equal to the negative energy of last occupied state. For example, this takes place in the Rn isotope with $N = 184$ (Fig. 4.4a and b). For a realistic pairing and for a typical shell structure of nuclei close to the drip line the neutron chemical potential will be close to the zero energy (Fig. 4.4a). The increase of neutron number above $N = 190$ triggers the development of deformation (Fig. 4.4c) which activates a new mechanism. Now the degeneracy of states goes down from $2j + 1$ to 2 and intruder orbitals from above the gap and extruder orbitals from below the gap start to close the spherical $N = 184$ gap; this mechanism is active in the vicinity of any spherical shell gap and clearly seen in the

Nilsson diagram (see, for example, Fig. 15 in Ref. [54]). This mechanism combined with the gradual increase of the deformation and neutron number allows to keep the neutron chemical potential in the vicinity of zero energy for an extended range of neutron numbers (Fig. 4.4a). However, increasing pairing correlations produce additional binding and can shift in some cases the neutron chemical potential below zero energy thus making the nucleus bound. The opposite can happen for decreasing pairing correlations.

4.4 Shell structure and single-particle energies at the two-neutron drip line.

It was suggested in Ref. [84] that the position of the two-neutron drip line sensitively depends on the underlying shell structure and that the uncertainties of the theoretical predictions of the neutron drip-line depend on the accuracy of the description of the single-particle energies. This shell structure effects are clearly visible in the fact that for some combinations of Z and N there is basically no (or very little) dependence of the predicted location of the two-neutron drip line on the EDF [84, 40] (see Fig. 4.1 and Refs. [5, 84, 40]). Such a weak (or vanishing) dependence, seen in all model calculations, is especially pronounced at the spherical neutron shell closures with $N = 126$ and 184 around the proton numbers $Z = 54$ and 80, respectively. In addition, a similar situation is seen in the CDFT calculations at $N = 258$ and $Z \sim 110$ (Fig. 4.1).

Although it has been pointed out in Ref. [84] that these features are due to the large neutron shell gaps at the magic neutron numbers, these gaps and their dependence on the CEDF have not been explored in detail. In order to fill this gap in our knowledge, we performed a detailed investigation of the shell structure of nuclei in the areas where the

spread in the predictions for the position of two-neutron drip line is either non-existent or very small. These are the nuclei $^{114}_{32}\mathrm{Ge}_{82}$, $^{180}_{54}\mathrm{Xe}_{126}$, $^{266}_{82}\mathrm{Pb}_{184}$, and $^{366}_{108}\mathrm{Hs}_{258}$ and their location in the nuclear chart is shown in Fig. 4.1 with red dots. The neutron single-particle orbitals active in the vicinity of the Fermi level of these nuclei are shown in Fig. 4.5. In order to create a more representative statistical ensemble, the calculations have been performed with 10 CEDF's. Amongst those are the CEDF's NL3* [33], DD-ME2 [26], DD-MEδ [28] and DD-PC1 [27] used in chapter III and Ref. [40] for the global study of the performance of the state-of-the-art CEDF's. For these CEDF's, the two-neutron drip lines are defined in model calculations up to $Z = 120$ in chapter III and Refs. [84, 40]. Only these four CEDF's were used in the definition of theoretical uncertainties in the position of two-neutron drip line shown in Fig. 4.1. In addition, we employ now the CEDF's NL3 [38], NL1 [138], FSUGold [76], PC-F1 [139], PC-PK1 [79], and TM1 [78] in a study of the shell structure. The two-neutron drip lines have not been studied with these six CEDF's so far.

The average (among ten used CEDF's) size of the shell gap is shown by a solid circle. Thin and thick vertical lines are used to show the spread of the sizes of the calculated shell gaps; the top and bottom of these lines corresponds to the largest and smallest shell gaps amongst the considered set of CEDF's. Thin lines show this spread for all employed CEDF's, while thick lines are used for the subset of four CEDF's (NL3*, DD-ME2, DD-MEδ and DD-PC1). Neutron numbers corresponding to the shell gaps are indicated.

The results of the calculations with all these CEDF's clearly show the presence of large neutron shell gaps at $N = 126$ in ^{180}Xe, at $N = 184$ in ^{266}Pb and at $N = 258$ in ^{366}Hs and a smaller $N = 82$ gap in ^{114}Ge (see Fig. 4.5). The average sizes of these gaps and

the spreads in their predictions are summarized in Fig. 4.6. The average (among ten used CEDF's) size of the shell gap is shown by a solid circle. Thin and thick vertical lines are used to show the spread of the sizes of the calculated shell gaps; the top and bottom of these lines corresponds to the largest and smallest shell gaps amongst the considered set of CEDF's. Thin lines show this spread for all employed CEDF's, while thick lines are used for the subset of four CEDF's (NL3*, DD-ME2, DD-MEδ and DD-PC1). Neutron numbers corresponding to the shell gaps are indicated. The gaps at $N = 126$ and 184 are around 4 MeV and they are the largest amongst these four gaps. The gap at $N = 258$ is the smallest and it is slightly larger than 2 MeV. Neutron pairing is typically quenched at these gaps (see Fig. 4.2). Definitely, the substantial size of the gap and the quenching of neutron pairing lead to a decrease of the uncertainties in the prediction of the two-neutron drip lines. The largest uncertainties in the position of two-neutron drip line exist around ^{114}Ge (Fig. 4.1), where the neutron $N = 82$ shell gap is the smallest among the above discussed nuclei. It is interesting that the spreads in the prediction of the size of these gaps decrease with the increase of the neutron number.

These gaps are also compared with the calculated gaps in the doubly magic nuclei ^{56}Ni, ^{100}Sn, ^{132}Sn and ^{208}Pb (Fig. 4.6). The experimentally known gaps of these nuclei are reasonably well described in the relativistic calculations with particle-vibration coupling of Ref. [140, 103] with the CEDF NL3*. The general trend of the decrease of the size of the neutron gaps with neutron number is clearly visible. However, the $N = 126$ gap in ^{180}Xe and the $N = 184$ gap in ^{266}Pb are only by one MeV smaller than the $N = 126$ gap in doubly magic ^{208}Pb. It is also important to mention that for the nuclei with $N = 82$

and $N = 126$ the spread of theoretical predictions with respect to the size of the gap only slightly increases on going from known nuclei towards nuclei in the vicinity of two-neutron drip line. On the contrary, this spread decreases appreciably for the nuclei ^{266}Pb and ^{366}Hs as compared with lighter nuclei (Fig. 4.6). These results clearly suggest that the pronounced shell structure at the well known major shells still survives in the nuclei close to the two-neutron drip line (see also an early investigation in this direction in Ref. [141]).

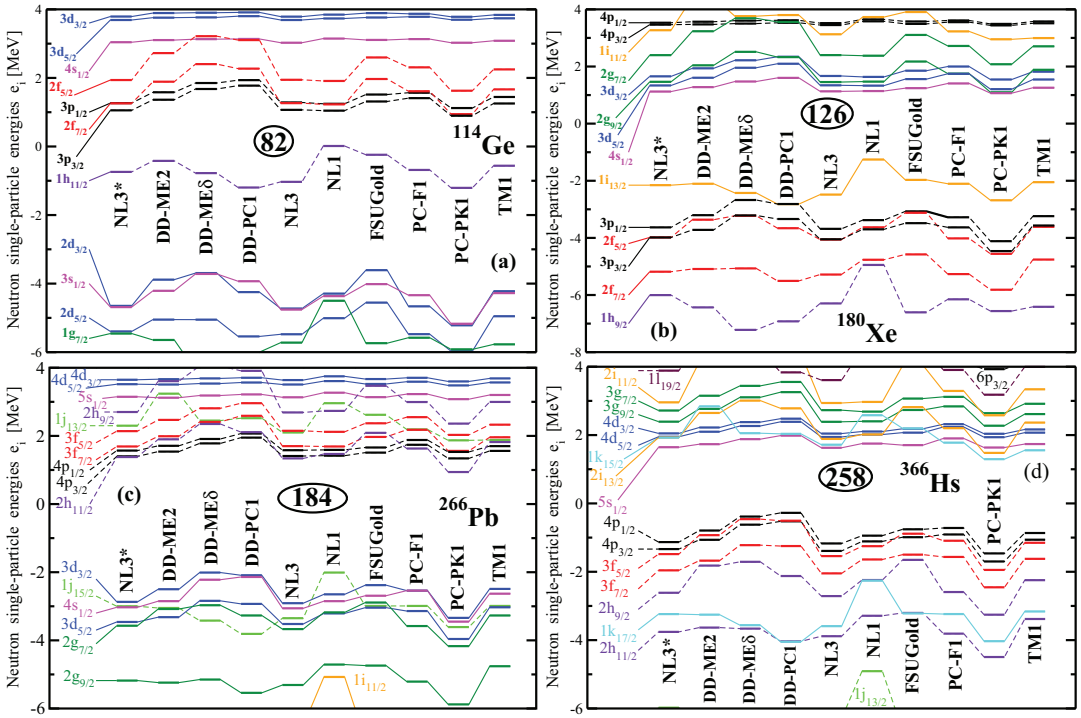

Figure 4.5

Neutron single-particle states at spherical shape in the indicated nuclei.

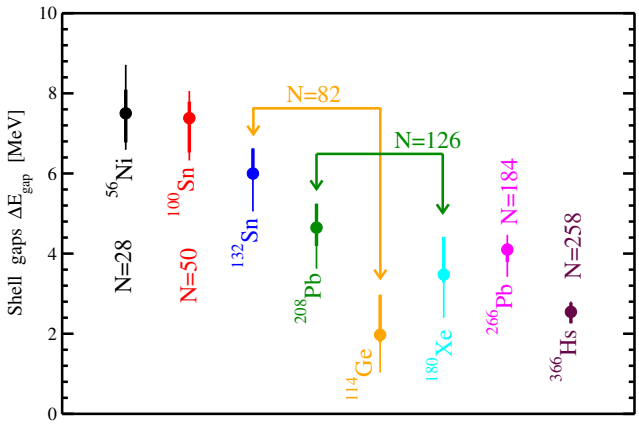

Figure 4.6

Neutron shell gaps $\Delta E_{\rm gap}$ for the nuclei under study.

4.5 Concluding remarks

Covariant density functional theory has been applied to an analysis of sources of uncertainties in the predictions of the two-neutron drip line. The following conclusions have been obtained:

- The differences in the underlying single-particle structure of different covariant energy density functionals represent the major source of uncertainty in the prediction of the position of the two-neutron drip line. In particular, this position depends on the positions of high-j orbitals below the shell gap and of high-j resonances in the continuum above the shell gap.

- The analysis of the present results strongly suggests that the uncertainties in the description of the single-particle energies at the two-neutron drip line are dominated by those which already exist in known nuclei. As a consequence, only an estimated one third of the uncertainty in the description of the single-particle energies at the two-

neutron drip line could be attributed to the uncertainties in the isovector properties of EDF's. This result strongly suggests that the improvement in the DFT description of the energies of the single-particle states in known nuclei will reduce the uncertainties in the prediction of the position of two-neutron drip line.

- The uncertainties in the pairing properties near the two-neutron drip line represent a secondary source of uncertainty in the definition of two-neutron drip line. The pairing properties in neutron rich nuclei depend substantially on the underlying CEDF, even when these properties are similar in experimentally known nuclei. These uncertainties in pairing properties translate into some uncertainties in the position of two-neutron drip line. However, they are substantially smaller than the ones due to the underlying single-particle structure.

Although the present investigation is restricted to covariant energy density functionals, it is reasonable to expect that its results are in many respects also applicable to non-relativistic DFT's. This is because similar problems in the description of single-particle and pairing properties exist also for the Skyrme and Gogny DFT's [142, 105, 143, 144].

CHAPTER V

OCTUPOLE DEFORMATION IN THE GROUND STATES OF EVEN-EVEN NUCLEI: A GLOBAL ANALYSIS WITHIN THE COVARIANT DENSITY FUNCTIONAL THEORY

5.1 Introduction

Reflection asymmetric (or octupole deformed) shapes represent an interesting example of symmetry breaking of the nuclear mean field. The physics of such shapes in the normal deformed minimum (both in non-rotating and rotating systems) has been extensively studied in the 80ies and 90ies of the last century (see the review in Ref. [145]). Reflection asymmetric shapes are also present for large deformations at the outer fission barriers in the actinides, superheavy nuclei and nuclei important in the r-process of nucleosynthesis [145, 70, 146]. At present, there is a revival of the interest to the study of such shapes. It is seen in a substantial number of theoretical [147, 148, 149, 150, 151, 152, 153, 154, 155, 156, 157, 158, 159, 160] and experimental [161, 162, 163, 164, 165, 166, 167, 168, 169] studies of octupole correlations and octupole deformed nuclei in the normal deformed minimum. Moreover, the attempts to understand microscopically the fission process, cluster radioactivity and the stability of superheavy elements [170, 70, 171, 172, 173, 174, 175, 176, 177, 178, 179, 180] as well as renewed interest to experimental studies of fission

[181, 182, 183] created a substantial interest in octupole deformed shapes at large deformations.

The existence of octupole deformed shapes is dictated by the underlying shell structure. Strong octupole coupling exists for particle numbers associated with a large $\Delta N = 1$ interaction between intruder orbitals with (l, j) and normal-parity orbitals with $(l-3, j-3)$ [145]. For normal deformed nuclei not far away from beta stability the tendency towards octupole deformation or strong octupole correlations occurs just above closed shells at particle numbers near 34 (the coupling between the $1g_{9/2}$ and $2p_{3/2}$ orbitals), 56 (the coupling between the $1h_{11/2}$ and $2d_{5/2}$ orbitals), 88 (the coupling between the $1i_{13/2}$ and $2f_{7/2}$ orbitals) and 134 (the coupling between the $1j_{15/2}$ and $2g_{9/2}$ orbitals) [145].

Some of the studies of the octupole shapes have been performed in the framework of covariant density functional theory (CDFT) [29]. The first investigation of the role of octupole deformation in the CDFT framework has been performed in Ref. [184]. In this work, the occurrence of stable octupole deformation in the ground states of the Ra isotopes and the impact of octupole deformation on fission barriers of the ^{226}Ra, ^{232}Th and ^{240}Pu nuclei has been studied with the covariant energy density functionals (CEDFs) NL1, NLSH and PL-40. However, because of some deficiencies these functionals are no longer in use. During the last ten years some extra calculations for the ground states of octupole deformed nuclei have been performed in the Ra [185, 156], Th [155, 156], Ba [186, 156] and Sm [187, 156] isotope chains.

However, a number of questions are left beyond the scope of these investigations. First of all, a global survey of octupole deformed and octupole soft nuclei in the CDFT frame-

work across the full nuclear landscape has not been done. Secondly, the estimate of theoretical uncertainties in the description of octupole deformed nuclei have not been provided. The importance of such estimate become clear in the light of recent publications [64, 65, 40, 137, 188]. Such an estimate is not possible based on the results of previous studies since they were performed either with only one functional or for a given nucleus or isotope chain with different frameworks.

To address these two questions, we have performed a global survey of all even-even $Z \leq 106$ nuclei located between the two-proton and two-neutron drip lines employing the DD-PC1 [27] and NL3* [33] CEDFs. Additional studies was performed with the DD-ME2 [26], PC-PK1 [79] and DD-MEδ [28] functionals in the known regions of octupole deformed nuclei and their vicinity. This allows us to estimate the theoretical uncertainties in the description of physical observables. Also, the results of our investigation are consistently compared with the ones obtained in the HFB approach with the Gogny forces and, in particular, with the microscopic+macroscopic (MM) results presented in Ref. [4]. This investigation is a continuation of our efforts to understand the accuracy and theoretical uncertainties in the description of the ground state observables [40], the extension of the nuclear landscape [84, 40, 137] and the properties of superheavy nuclei [188].

5.2 Details of the theoretical calculations

The calculations were performed in the Relativistic-Hartree-Bogoliubov (RHB) approach for which a new parallel computer code RHB-OCT was developed using as a basis the octupole deformed RMF+BCS code DOZ developed in Ref. [70]. Only axial reflection

asymmetric shapes are considered in the RHB-OCT code. The parallel version allows simultaneous calculations for a significant number of nuclei and deformation points in each nucleus.

The calculations in the RHB-OCT code perform the variation of the function

$$E_{RHB} + \sum_{\lambda=2,3} C_{\lambda 0}(\langle \hat{Q}_{\lambda 0} \rangle - q_{\lambda 0})^2 \tag{5.1}$$

employing the method of quadratic constraints. Here E_{RHB} is the total energy and $\langle \hat{Q}_{\lambda 0} \rangle$ denote the expectation value of the quadrupole ($\hat{Q}_{20}$) moment given by Eq. (3.3) and octupole ($\hat{Q}_{30}$) moment which is defined as

$$\hat{Q}_{30} \;\; = \;\; z(2z^2 - 3x^2 - 3y^2). \tag{5.2}$$

C_{20} and C_{30} in Eq. (5.1) are the corresponding stiffness constants [46] and q_{20} and q_{30} are constrained values of the quadrupole and octupole moments. In order to provide the convergence to the exact value of the desired multipole moment we use the method suggested in Ref. [68]. Here the quantity $q_{\lambda 0}$ is replaced by the parameter $q_{\lambda 0}^{eff}$, which is automatically modified during the iteration in such a way that we obtain $\langle \hat{Q}_{\lambda 0} \rangle = q_{\lambda 0}$ for the converged solution. This method works well in our constrained calculations. We also fix the (average) center-of-mass of the nucleus at the origin with the constraint

$$< \hat{Q}_{10} >= 0 \tag{5.3}$$

on the center-of-mass operator $\hat{Q}_{10}$ in order to avoid a spurious motion of the center-of-mass.

The charge quadrupole moment is given by Eq. (3.4) and the octupole moment is defined as

$$Q_{30} = \int d^3r\rho(r)\, z(2z^2 - 3r_\perp^2) \tag{5.4}$$

which is transform into a dimensionless deformation β_3 using the relations

$$Q_{30} = \sqrt{\frac{16\pi}{7}}\frac{3}{4\pi}ZR_0^3\beta_3. \tag{5.5}$$

In order to avoid the uncertainties connected with the definition of the size of the pairing window [189], we use the separable form of the finite range Gogny pairing interaction introduced by Tian et al [58] which has been discussed in Sec. 2.3 of chapter II. The truncation of the basis is performed in such a way that all states belonging to the major shells up to $N_F = 16$ fermionic shells for the Dirac spinors and up to $N_B = 20$ bosonic shells for the meson fields are taken into account (for details see Ref. [34]). The potential energy surfaces are calculated in constrained calculations in the (β_2, β_3) plane for the β_2 values ranging from -0.2 up to 0.4 and for the β_3 values ranging from 0.0 up to 0.3 with a deformation step of 0.02 in each direction. The energies of the local minima are defined in unconstrained calculations.

The effect of octupole deformation can be quantitatively characterized by the quantity ΔE_{oct} defined as

$$\Delta E_{oct} = E^{oct}(\beta_2, \beta_3) - E^{quad}(\beta_2', \beta_3' = 0) \tag{5.6}$$

where $E^{oct}(\beta_2, \beta_3)$ and $E^{quad}(\beta_2', \beta_3' = 0)$ are the binding energies of the nucleus in two local minima of potential energy surface; the first minimum corresponds to octupole deformed shapes and second one to the shapes with no octupole deformation. The quantity

$|\Delta E_{oct}|$ represents the gain of binding due to octupole deformation. It is also an indicator of how stable the octupole deformed shapes are. Large $|\Delta E_{oct}|$ values are typical for well pronounced octupole minima in the PES; for such systems the stabilization of static octupole deformation is likely. On the contrary, small $|\Delta E_{oct}|$ values are characteristic for soft (in octupole direction) PES typical for octupole vibrations. In such systems, beyond mean field effects can play an important role. They have profound effect on the spectroscopy of the nuclei, in particular, on the E1 and enhanced E3 transition strengths [190, 160, 191], and on the energy splittings of the positive and negative parity branches of alternating parity rotational bands [192, 160]. On the other hand, octupole beyond-mean-field correlations do not affect in a significant way the trends and systematics of binding energies [193].

5.3 Octupole deformation in actinides

Several studies of the octupole deformation in the ground states of actinides and its impact on spectroscopic properties of these nuclei have been performed so far in the CDFT framework. The first relativistic study of octupole shapes in the ground states of atomic nuclei has been performed twenty years ago in Ref. [184]; in this article radium isotopes have been investigated in the RMF+BCS approach using monopole pairing with constant pairing gap and the CEDFs NL1, NL-SH and PL-40. Shape evolution from spherical to octupole-deformed shapes has been studied in even-even Th isotopes in the RMF+BCS framework in Ref. [148] using monopole pairing with constant pairing gap and the NL3* and PK1 functionals. Octupole deformed shapes in ^{226}Ra have been investigated earlier

in Ref. [185] within the same approach but with NL1 and NL3 functionals. The potential energy surfaces and octupole deformations of the ground states of even-even $^{222-232}$Th and $^{218-228}$Ra nuclei have been studied in the RHB framework with the DD-PC1 functional and separable pairing forces in Refs. [155, 156]. In a recent study, the first generator coordinate method taking into account dynamical correlations and quadrupole-octupole shape fluctuations have been undertaken in ^{224}Ra employing the PC-PK1 functional [160]. They reveal rotation-induced octupole shape stabilization.

It is clear that these studies were quite limited in scope and the selection of nuclei was guided by the previous studies in non-relativistic frameworks. A global review of octupole deformed nuclei in this mass region paints a much richer picture. Our RHB calculations indicate that not only Ra and Th nuclei (as suggested by previous studies) can have either stable octupole deformation or be octupole soft, but also U, Pu, Cm, Cf, Fm, No and Sg nuclei possess these properties. Neutron number dependencies of calculated equilibrium quadrupole and octupole deformations as well as the gains in binding due to octupole deformation for these isotope chains were investigated using NL3*, DD-ME2, DD-MEδ, DD-PC1 and PC-PK1 CEDFs.

5.3.1 Discussion: theory versus experiment for Ra isotopes

The potential energy surfaces of the Ra isotopes are shown in Figs. 5.1, 5.2 and 5.3. The white circle indicates the global minimum and the equipotential lines are shown in steps of 0.5 MeV. Weakly deformed minima with $\beta_3 = 0.0$ are the lowest in energy in the ^{218}Ra nucleus with $N = 130$ see Fig 5.1 . The increase of neutron number leads to the

formation of an octupole minimum which becomes pronounced at $N = 136$ (see Fig 5.2). At higher neutron numbers the potential energy surfaces become soft in octupole direction as shown in Fig. 5.3.

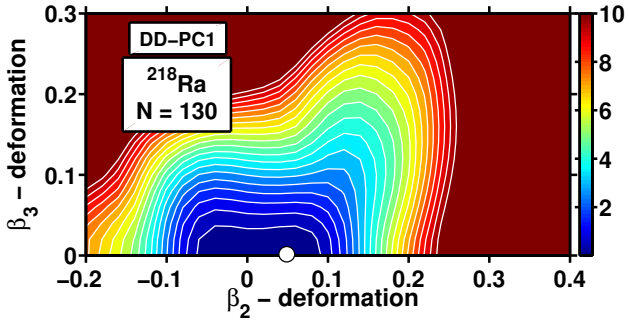

Figure 5.1

Potential energy surfaces of the ^{218}Ra isotopes in the (β_2, β_3) plane calculated with the CEDF DD-PC1.

The maximum gain in binding energy due to octupole deformation $|\Delta E^{oct}|$ is seen at $N \sim 136$ for the CEDFs PC-PK1, DD-ME2 and DD-PC1 and at $N = 138$ for NL3* (Fig. 5.4). For these functionals the maximum $|\Delta E^{oct}|$ values vary from around 1 MeV for NL3* and PC-PK1 up to 2 MeV for DD-ME2. The DD-MEδ functional does not predict octupole deformation for the nuclei of interest which contradicts both experimental data (see Ref. [145]) and the predictions of other models.

Experimental data suggest that in the Ra isotopes the maximum effect of octupole deformation is seen at $N \sim 136$ [145]. There are some differences in the predictions of the various models for the range of nuclei with octupole deformation and for the neutron numbers at which the maximum gain in binding due to octupole deformation takes place.

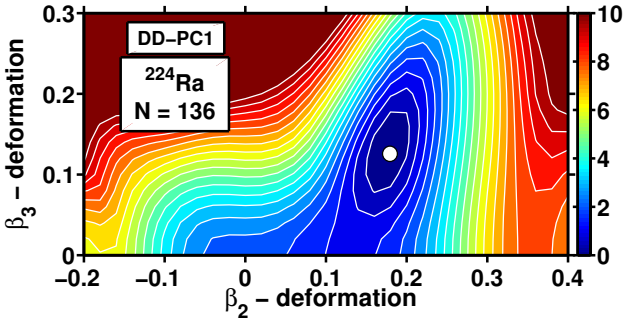

Figure 5.2

The same as in Fig. 5.1 but for ^{224}Ra.

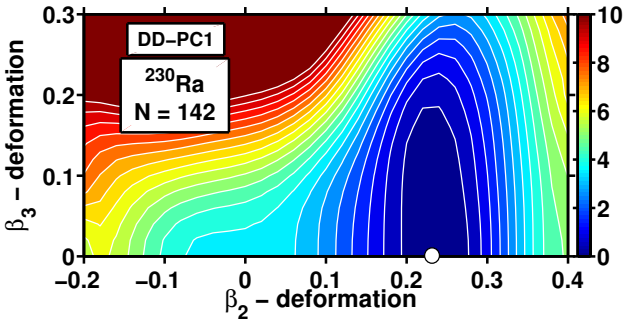

Figure 5.3

The same as in Fig. 5.1 but for ^{230}Ra.

For example, the MM calculations based on folded Yukawa [4] (see also Table 5.1) and Woods-Saxon potentials [194] predict octupole deformation in the $N = 130 - 138$ and $N = 134 - 138$ isotopes, respectively. In these models, the maximum gain in binding due to octupole deformation takes place at $N = 132$ and $N = 136$, respectively. Similar investigations and analysis where done for U, Pu, Cm, Cf, Fm, No, and Sg isotope chains (see Ref [195] for detail).

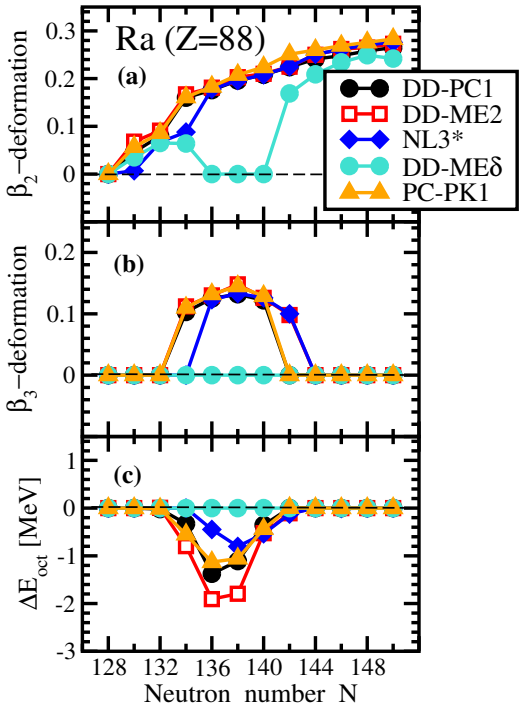

Figure 5.4

The calculated equilibrium β_2 and β_3 deformations as well as the ΔE^{oct} quantities for Ra isotope chain.

Figure 5.4 shows the calculated equilibrium quadrupole β_2(panel (a)) and octupole β_3 (panel (b)) deformations as well as the ΔE^{oct} quantities (panel (c)) for Ra isotope chain.

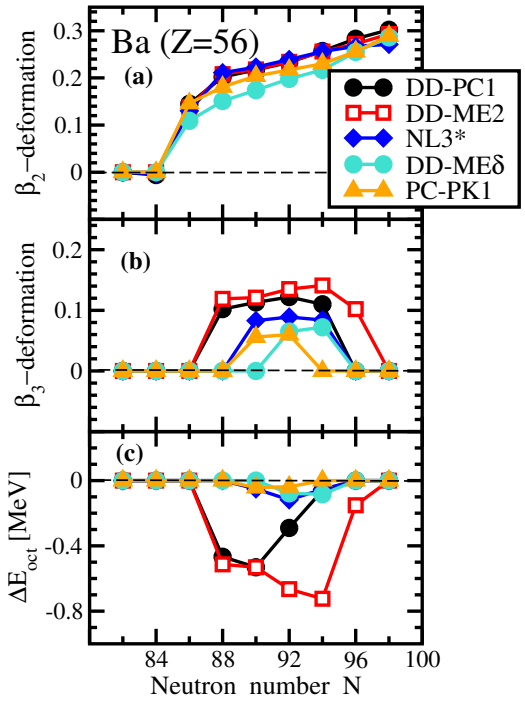

Figure 5.5

The same as in Fig. 5.4 but for Ba isotope chain.

5.4 Octupole deformation in lanthanides

Octupole deformation is predicted also in the ground states of the Ba, Ce, Nd and Sm isotopes. Several features are typical for this mass region.

First, the gain in binding due to octupole deformation is substantially smaller ($|\Delta E^{oct}|$ is typically around 0.5 MeV) than in the actinides. Thus, the stabilization of octupole deformation at the ground state is less likely in this region as compared with actinides.

Secondly, the results obtained with DD-MEδ still differ from the ones obtained with other functionals. However, the differences are less pronounced as compared with the actinides where the RHB results obtained with this functional contradict drastically available experimental data and the results of other functionals.

In general, the island of octupole deformation predicted in the RHB calculations is close to the ones obtained in non-relativistic calculations. It is also close to the one extracted from experimental data indicating either octupole deformation or enhanced octupole correlations (see Ref. [145] for details). However, a detailed interpretation of experimental data in this mass region at the mean field level is complicated by the fact that PES are extremely soft in the octupole direction which favors the fluctuations and vibrations in this degree of freedom.

5.4.1 Ba isotopes.

A non-zero octupole deformation is predicted for the $N = 88 - 94$ $^{144-150}$Ba isotopes in calculations with DD-PC1, for the $N = 88 - 96$ $^{144-152}$Ba isotopes with DD-ME2 and NL3*, and for the $N = 90 - 92$ $^{146-148}$Ba isotopes with PC-PK1 (Fig. 5.5). The maximum

gain in binding due to octupole deformation takes place at $N = 90$ for DD-PC1 and PC-PK1, at $N = 92$ for NL3* and at $N = 94$ for DD-ME2. The RMF+BCS calculations with PK1 CEDF of Ref. [186] predict a finite octupole deformation in the $N = 88 - 98$ Ba isotopes with a maximum octupole deformation around $N = 92 - 94$. On the contrary, in the MM calculations with a folded Yukawa potential (Ref. [4] and Table 5.1) only the $N = 86 - 90$ isotopes possess non-zero octupole deformation. The MM results of Ref. [196] based on a Woods-Saxon potential show non-zero octupole deformation only in the $N = 88-90$ nuclei. The HF+BCS calculations with Gogny D1S force of Ref. [197] predict non-zero octupole deformation in the $N = 88 - 92$ $^{142-148}$Ba nuclei with a maximum gain of binding due to octupole deformation at the nucleus ^{144}Ba with $N = 90$. Also similar investigations and analysis where undertaken for Xe, Ce, Nd and Sm isotope chains (see Ref [195] for details).

5.5 Octupole deformation in superheavy region

To our knowledge no search of octupole deformation in the ground states of superheavy $Z \geq 108$ nuclei has been performed within the CDFT framework so far. To fill this gap in our knowledge we performed such a search in the region of proton numbers $108 \leq Z \leq 126$ and in the region of neutron numbers from the two-proton drip line up to neutron number $N = 210$. For this region ($Z > 106$) the truncation of the basis is performed in such a way that all states belonging to the major shells up $N_F = 18$ fermionic shells for the Dirac spinors and up to $N_B = 20$ bosonic shells for the meson fields in case of meson exchange functionals are taken into account.

Our calculations do not reveal the presence of octupole deformation in the ground states of superheavy nuclei with $Z \geq 110$ similar to the Skyrme DFT calculations of Ref. [146] . Two $Z = 108$ (two $Z = 108$ and one $Z = 110$) nuclei have non-zero octupole deformation in the calculations with CEDF DD-PC1 (DD-ME2). These nuclei are extremely soft in octupole deformation with very small gain in binding energy due to octupole deformation ($|\Delta E^{oct}| < 0.1$ MeV).

On the contrary, the Gogny DFT Ref. [173]) and mic+mac (Ref. [6]) calculations predict the existence of such nuclei. The HFB calculations based on the Gogny D1S force predict octupole deformation in the ground states of the $(Z = 108 - 126, N = 186 - 190)$ even-even nuclei (see Fig. 3 in Ref. [173]). These nuclei either do not have quadrupole deformation (the $N = 186$ and some $N = 188$ nuclei) or this deformation is rather small ($\beta_2 < 0.1$) for $N = 190$ and some $N = 188$ nuclei. The octupole deformation is rather small for most of these nuclei apart of few $N = 188$ nuclei and the majority of the $N = 190$ nuclei which have substantial octupole deformation β_3 exceeding 0.1. Note that these calculations cover only nuclei with $N \leq 190$. More extensive mic+mac calculations of Ref. [6] indicate larger region of octupole deformation in the superheavy nuclei.

Table 5.1 list the calculated effect of reflection asymmetry on nuclear ground state properties. The equilibrium quadrupole (β_2) and octupole (β_3) deformations as well as the gains in binding energy due to octupole deformation $|\Delta E^{oct}|$ are given. The results are presented only in the case when the octupole deformed minimum is the lowest in energy. Note that ϵ_2 and ϵ_3 are the quadrupole and octupole deformations (in the Nilsson perturbed-spheroid parametrization) obtained in the MM approach of Ref. [4].

Table 5.1: Calculated effect of reflection asymmetry on nuclear ground state properties.

Nucleus			**DD-PC1**			**NL3***			**mic+mac**		
Z	N	A	β_2	β_3	$\lvert\Delta E^{oct}\rvert$	β_2	β_3	$\lvert\Delta E^{oct}\rvert$	ϵ_2	ϵ_3	$\lvert\Delta E^{oct}\rvert$
20	36	56							-0.07	0.02	0.04
	40	60							0.00	0.07	0.03
38	40	78	0.005	0.084	0.089	0.005	0.078	0.019			
40	38	78	0.003	0.068	0.043	0.003	0.060	0.005			
	40	80	0.008	0.145	0.439	0.007	0.139	0.149			
	68	108				0.002	0.060	0.009			
	70	110				0.001	0.053	0.004			
	72	112	-0.003	0.094	0.133						
42	40	82	-0.001	0.078	0.070	-0.001	0.064	0.007			
48	42	90							-0.01	0.04	0.04
54	54	108							0.15	0.05	0.05
	56	110							0.16	0.07	0.20
	58	112							0.18	0.07	0.14
	88	142							0.13	0.06	0.11
	90	144							0.15	0.07	0.11
56	52	108							0.13	0.05	0.05
	54	110							0.17	0.09	0.34
	56	112	0.244	0.114	0.284	0.274	0.188	0.792	0.18	0.10	0.48
	58	114	0.252	0.097	0.157	0.267	0.155	0.374	0.20	0.09	0.31
	60	116	0.275	0.074	0.888						
	86	142							0.12	0.06	0.14
	88	144	0.201	0.101	0.467				0.15	0.09	0.49
	90	146	0.216	0.112	0.531	0.202	0.083	0.051	0.16	0.09	0.47
	92	148	0.232	0.122	0.290	0.216	0.089	0.118			
	94	150	0.254	0.114	0.061	0.230	0.084	0.053			
58	56	114	0.254	0.100	0.166	0.286	0.161	0.396	0.21	0.08	0.21

Continued on next page

Table 5.1 – Continued from previous page

Nucleus			**DD-PC1**			**NL3***			**mic+mac**		
Z	N	A	β_2	β_3	$\lvert\Delta E^{oct}\rvert$	β_2	β_3	$\lvert\Delta E^{oct}\rvert$	ϵ_2	ϵ_3	$\lvert\Delta E^{oct}\rvert$
	86	144							0.13	0.07	0.22
	88	146	0.205	0.113	0.631	0.194	0.097	0.224	0.16	0.09	0.46
	90	148	0.222	0.125	0.714	0.215	0.113	0.390	0.19	0.07	0.02
	92	150	0.246	0.134	0.111	0.236	0.120	0.384			
60	86	146							0.14	0.06	0.08
	88	148	0.206	0.114	0.491	0.198	0.105	0.208	0.18	0.06	0.09
	90	150	0.235	0.128	0.044	0.231	0.121	0.261			
62	88	150	0.211	0.098	0.253	0.206	0.091	0.091	0.19	0.04	0.02
64	132	196	0.136	0.062	0.335						
	134	198	0.167	0.090	0.117						
	136	200	0.192	0.119	0.046	0.182	0.003	0.008			
	138	202	0.217	0.142	0.088						
66	134	200	0.176	0.049	0.274						
	136	202	0.202	0.090	0.200						
	138	204	0.231	0.106	0.368						
68	130	198							0.06	0.05	0.10
	132	200							0.11	0.04	0.05
	134	202	0.170	0.004	0.017				0.11	0.06	0.04
	136	204	0.200	0.065	0.265						
70	134								0.11	0.04	0.04
76	134								0.09	0.02	0.02
78	136								0.09	0.03	0.03
80	136								0.06	0.05	0.02
	138								0.08	0.05	0.14
82	98	180							0.00	0.03	0.02
	100	182	0.004	0.041	0.038				0.01	0.02	0.08
	102	184	0.002	0.041	0.038				0.00	0.02	0.04
	134	216							0.01	0.04	0.02
	136	218							0.01	0.06	0.16

Continued on next page

Table 5.1 – Continued from previous page

Nucleus			**DD-PC1**			**NL3***			**mic+mac**		
Z	N	A	β_2	β_3	$\lvert\Delta E^{oct}\rvert$	β_2	β_3	$\lvert\Delta E^{oct}\rvert$	ϵ_2	ϵ_3	$\lvert\Delta E^{oct}\rvert$
	138	220							0.01	0.07	0.23
	140	222							0.01	0.07	0.26
84	134	218							0.05	0.09	0.44
	136	220							0.09	0.09	0.42
	138	222							0.10	0.08	0.16
86	132	218							0.07	0.10	0.67
	134	220							0.10	0.09	0.85
	136	222							0.10	0.09	0.64
	138	224							0.13	0.08	0.29
	140	226							0.15	0.04	0.09
	146	232							0.21	0.02	0.02
88	130	218							0.07	0.09	0.59
	132	220							0.10	0.09	1.20
	134	222	0.160	0.104	0.310				0.11	0.10	1.27
	136	224	0.177	0.125	1.370	0.178	0.124	0.547	0.13	0.10	0.91
	138	226	0.196	0.133	1.110	0.197	0.134	0.874	0.15	0.08	0.40
	140	228	0.208	0.123	0.385	0.208	0.126	0.526	0.16	0.06	0.08
	142	230				0.225	0.098	0.105			
90	130	220							0.08	0.10	1.33
	132	222							0.10	0.10	1.35
	134	224	0.167	0.112	0.491				0.13	0.11	1.22
	136	226	0.186	0.137	1.999	0.187	0.134	0.814	0.14	0.10	0.50
	138	228	0.214	0.154	1.402	0.212	0.150	1.387	0.16	0.08	0.08
	140	230	0.224	0.152	0.642	0.223	0.149	0.770			
	142	232	0.234	0.141	0.025	0.236	0.138	0.231			
	146	236	0.261	0.054	0.039	0.274	0.041	0.002			
	198	288	0.176	0.127	1.084						
	200	290	0.189	0.135	0.716						
	202	292	0.205	0.113	0.216	0.182	0.095	0.102			
	204	294	0.221	0.065	0.051	0.198	0.090	0.126			
92	128	220							0.05	0.08	0.08
	130	222							0.09	0.10	1.21
	132	224							0.12	0.10	1.22

Continued on next page

Table 5.1 – Continued from previous page

Nucleus			**DD-PC1**			**NL3***			**mic+mac**		
Z	N	A	β_2	β_3	$\lvert\Delta E^{oct}\rvert$	β_2	β_3	$\lvert\Delta E^{oct}\rvert$	ϵ_2	ϵ_3	$\lvert\Delta E^{oct}\rvert$
	134	226							0.13	0.10	0.60
	136	228	0.201	0.155	1.724	0.201	0.151	1.813			
	138	230	0.229	0.170	1.399	0.228	0.165	1.264			
	140	232	0.238	0.169	0.659	0.238	0.166	0.721			
	142	234	0.245	0.170	0.067	0.247	0.162	0.217			
	146	238	0.275	0.078	0.094	0.284	0.068	0.019			
	198	290	0.181	0.140	1.378						
	200	292	0.196	0.151	0.969	0.183	0.124	0.664			
	202	294	0.214	0.137	0.319	0.200	0.127	0.416			
	204	296	0.233	0.082	0.074	0.220	0.117	0.133			
94	128	222							0.05	0.08	0.35
	130	224							0.09	0.10	1.09
	132	226							0.12	0.10	0.59
	134	228	0.170	0.134	1.260	0.167	0.129	0.354	0.14	0.10	0.04
	136	230	0.197	0.155	1.535	0.196	0.152	1.251			
	138	232	0.246	0.161	0.622	0.240	0.159	0.501			
	140	234	0.263	0.133	0.125	0.261	0.142	0.121			
	146	240	0.284	0.066	0.099	0.290	0.054	0.010			
	194	288	0.131	0.108	1.156	0.119	0.089	0.132			
	196	290	0.156	0.131	1.774	0.151	0.118	0.780			
	198	292	0.176	0.146	1.419	0.171	0.135	1.046			
	200	294	0.192	0.158	0.965	0.187	0.142	0.770			
	202	296	0.216	0.141	0.162	0.206	0.143	0.327			
96	128	224							0.04	0.08	0.52
	130	226							0.08	0.10	0.84
	132	228	0.134	0.115	0.562	0.130	0.111	0.152	0.14	0.08	0.02
	134	230	0.162	0.135	1.511	0.159	0.132	1.248			
	136	232	0.195	0.158	1.190	0.194	0.154	0.877			
	138	234	0.252	0.142	0.387	0.249	0.145	0.212			
	140	236	0.274	0.098	0.131	0.275	0.096	0.041			
	146	242	0.295	0.063	0.132	0.298	0.044	0.005			
	190	286	0.095	0.105	0.271						
	192	288	0.115	0.116	1.394	0.116	0.102	0.516			
	194	290	0.131	0.126	1.994	0.135	0.119	0.923			
	196	292	0.150	0.137	1.790	0.155	0.136	1.191			

Continued on next page

Table 5.1 – Continued from previous page

Nucleus			**DD-PC1**			**NL3***			**mic+mac**		
Z	N	A	β_2	β_3	$\lvert\Delta E^{oct}\rvert$	β_2	β_3	$\lvert\Delta E^{oct}\rvert$	ϵ_2	ϵ_3	$\lvert\Delta E^{oct}\rvert$
	198	294	0.170	0.151	1.294	0.172	0.147	1.110			
	200	296	0.190	0.164	0.878	0.189	0.154	0.701			
	202	298	0.217	0.142	0.049	0.211	0.153	0.229			
98	126	224	0.008	0.065	0.151				0.00	0.05	0.10
	128	226	0.015	0.049	0.032				0.03	0.08	0.56
	130	228							0.07	0.10	0.06
	132	230	0.146	0.111	0.427	0.142	0.112	0.247			
	134	232	0.172	0.141	1.292	0.170	0.138	0.895			
	136	234	0.198	0.164	1.122	0.198	0.160	0.747			
	138	236	0.245	0.146	0.379	0.244	0.146	0.195			
	140	238	0.266	0.114	0.197	0.266	0.114	0.107			
	190	288	0.106	0.123	0.515	0.102	0.090	0.095			
	192	290	0.131	0.131	1.259	0.132	0.114	0.473			
	194	292	0.146	0.140	1.632	0.153	0.134	0.848			
	196	294	0.164	0.150	1.388	0.171	0.152	1.056			
	198	296	0.180	0.162	1.087	0.185	0.162	0.983			
	200	298	0.196	0.173	0.868	0.199	0.168	0.680			
	202	300	0.218	0.147	0.094	0.217	0.164	0.273			
100	126	226	0.011	0.089	0.490	0.014	0.085	0.207	0.00	0.06	0.12
	128	228	0.014	0.079	0.149	0.023	0.073	0.092	0.02	0.08	0.52
	132	232	0.161	0.085	0.152	0.164	0.095	0.061			
	134	234	0.187	0.146	1.084	0.188	0.145	0.646			
	136	236	0.201	0.172	1.156	0.202	0.166	0.774			
	138	238	0.226	0.158	0.434	0.223	0.160	0.282			
	140	240	0.258	0.110	0.177	0.253	0.122	0.110			
	190	290	0.137	0.129	0.403						
	192	292	0.162	0.149	1.119	0.147	0.124	0.327			
	194	294	0.170	0.159	1.309	0.170	0.151	0.740			
	196	296	0.183	0.169	1.160	0.187	0.167	0.964			
	198	298	0.195	0.177	1.056	0.199	0.176	0.954			
	200	300	0.204	0.184	0.976	0.208	0.180	0.749			
	202	302	0.216	0.157	0.218	0.220	0.174	0.383			
102	134	236				0.197	0.120	0.321			
	136	238	0.205	0.145	0.725	0.206	0.144	0.424			

Continued on next page

Table 5.1 – Continued from previous page

Nucleus			**DD-PC1**			**NL3***			**mic+mac**		
Z	N	A	β_2	β_3	$\lvert\Delta E^{oct}\rvert$	β_2	β_3	$\lvert\Delta E^{oct}\rvert$	ϵ_2	ϵ_3	$\lvert\Delta E^{oct}\rvert$
	138	240				0.227	0.134	0.138			
	140	242				0.251	0.113	0.091			
	182	284	0.014	0.065	0.115						
	184	286	0.007	0.085	0.334						
	186	288	-0.004	0.085	0.257						
	188	290	-0.033	0.082	0.214						
	190	292	0.176	0.122	0.357						
	192	294	0.172	0.139	0.776	0.153	0.110	0.173			
	194	296	0.181	0.145	0.717	0.174	0.136	0.512			
	196	298	0.194	0.152	0.602	0.192	0.148	0.646			
	198	300	0.206	0.156	0.550	0.206	0.156	0.619			
	200	302	0.214	0.159	0.445	0.219	0.157	0.454			
	202	304				0.235	0.138	0.230			
	204	306				0.248	0.105	0.095			
104	138	242				0.241	0.094	0.090			
	140	244				0.254	0.102	0.117			
	142	246				0.264	0.094	0.032			
	184	288	0.002	0.090	0.407						
	186	290	-0.025	0.101	0.513						
	188	292	-0.039	0.100	0.536						
	190	294	0.195	0.105	0.454						
	192	296	0.201	0.116	0.366						
	194	298				0.179	0.115	0.340			
	196	300	0.230	0.126	0.226	0.218	0.134	0.402			
	200	304				0.232	0.131	0.276			
	202	306				0.246	0.111	0.145			
	204	308				0.256	0.086	0.067			
106	142	248				0.264	0.098	0.104			
	144	250	0.266	0.052	0.271	0.272	0.060	0.013			
	182	288	-0.003	0.055	0.076						
	184	290	-0.003	0.084	0.320						
	186	292	-0.032	0.102	0.530						
	188	294	-0.046	0.103	0.660	-0.033	0.060	0.024			
	194	300				0.182	0.097	0.257			

Continued on next page

Table 5.1 – Continued from previous page

Nucleus			DD-PC1			NL3*			mic+mac		
Z	N	A	β_2	β_3	$\lvert\Delta E^{oct}\rvert$	β_2	β_3	$\lvert\Delta E^{oct}\rvert$	ϵ_2	ϵ_3	$\lvert\Delta E^{oct}\rvert$
	196	302				0.211	0.109	0.282			
	198	304				0.230	0.111	0.179			
	200	306				0.246	0.098	0.073			

5.6 Global analysis

We carried out a global search for octupole deformation, which covers all even-even $Z \leq 106$ nuclei between the two-proton and two-neutron drip lines, with CEDFs DD-PC1 and NL3* and for $Z = 88 - 126$ nuclei from two-proton to two-netron drip lines employing CEDFs DD-PC1, NL3*, DD-ME2 and PC-PK1. The DD-MEδ functional was omitted from the global studies since it does not reproduce the experimental situation in octupole deformed actinides (Sec. 5.3) and provides unrealistically low fission barriers in superheavy nuclei (see Ref. [188]). The results of this search for DD-PC1 and NL3* are summarized in Table 5.1 and in Figs. 5.7 and 5.6 and for DD-ME2 and PC-PK1 in Figs. 5.8 and 5.9 respectively.

The results for DD-PC1 and NL3* are compared with the MM results of Ref. [4]. It can seen in Figs. 5.6 and 5.7 that in addition to the lanthanides, actinides, and the superheavy regions discussed above there are several regions of octupole deformed nuclei. These are nuclei around ^{80}Zr, ^{110}Zr and ^{200}Dy which are octupole soft. Since the gain of binding due to octupole deformation is quite small, no stabilization of octupole deformation is expected in these nuclei. Calculations with the Gogny forces also indicate octupole softness of the

nuclei around ^{80}Zr (see Fig. 9 in Ref. [149]). However, in the MM calculations of Ref. [149], these nuclei do not have octupole deformation (Table 5.1).

In the RHB calculations with DD-PC1 there exists a region of octupole soft Gd, Dy, and Er nuclei with $N \sim 136$ and $A \sim 200$ (Fig. 5.6 and Tableřeftable-global). However, in the RHB calculations with NL3* octupole softness is seen only in ^{200}Dy (Fig. 5.7. This difference is quite likely due to the fact that pairing correlations, which counteract octupole deformation, are substantially stronger in neutron-rich nuclei for the NL3* functional as compared with DD-PC1 (Ref. [137]).

In addition, octupole deformation is predicted in the ground states of the actinides and light superheavy nuclei with neutron number around $N \sim 196$ (Table 5.1 and Figs. 5.6, 5.7, 5.8 and 5.9). Most of the functionals predict that this region is substantially larger than the one around $Z \sim 92, N \sim 136$. Moreover, the maximum gain in binding due to octupole deformation is comparable in the $Z \sim 96, N \sim 196$ and $Z \sim 92, N \sim 136$ regions. This strongly suggests the stabilization of octupole deformation in the nuclei belonging to the central part of the $Z \sim 96, N \sim 196$ region. This region of nuclei will not be accessible with future facilities like FRIB since it is located beyond the expected reach of FRIB.

The detailed information on calculated equilibrium quadrupole (β_2) and octupole (β_3) deformations as well as the gains (ΔE^{oct}) in binding due to octupole deformation is summarized in Figs. 5.6, 5.7, 5.8 and 5.9. These results show large similarities between the NL3* and PC-PK1 functionals on the one hand and the DD-ME2 and DD-PC1 functionals on the other hand.

In Figure 5.6 we show octupole deformed nuclei in the nuclear chart. Only nuclei with non vanishing ΔE^{oct} are shown by squares; the colors of the squares represent the values of $|\Delta E^{oct}|$ with the CEDF DD-PC1. The blue dashed line shows the limits of the nuclear chart (defined as fission yield greater than 10^6) which may be achieved with dedicated existence measurements at FRIB [9]. The two-proton and two-neutron drip lines are displayed by solid black lines.

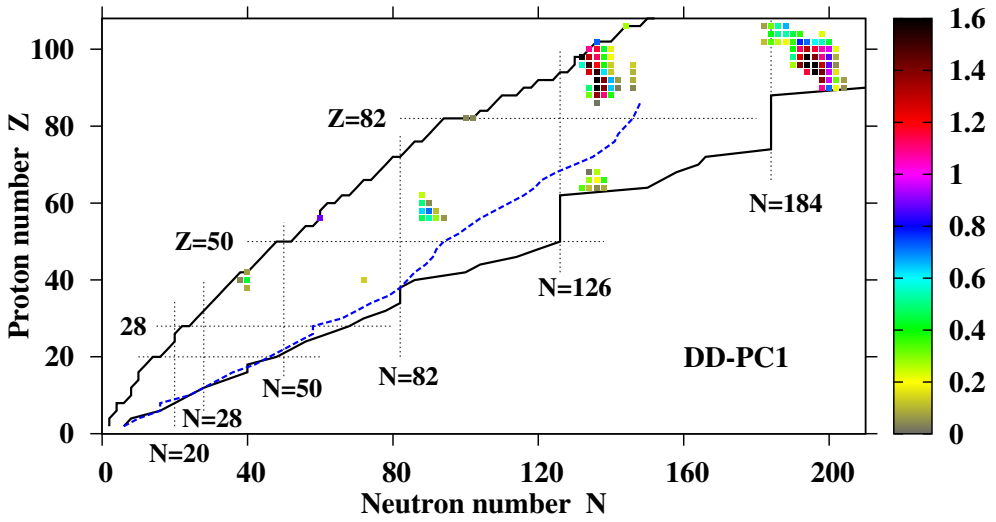

Figure 5.6

Octupole deformed nuclei in the nuclear chart. Only nuclei with non vanishing ΔE^{oct} are shown by squares.

5.7 Concluding remarks

A global search for octupole deformation has been performed within covariant density functional theory employing the DD-PC1 and NL3* functionals; this search covers all even-even nuclei with $Z \leq 106$ located between the two-neutron and two-proton drip

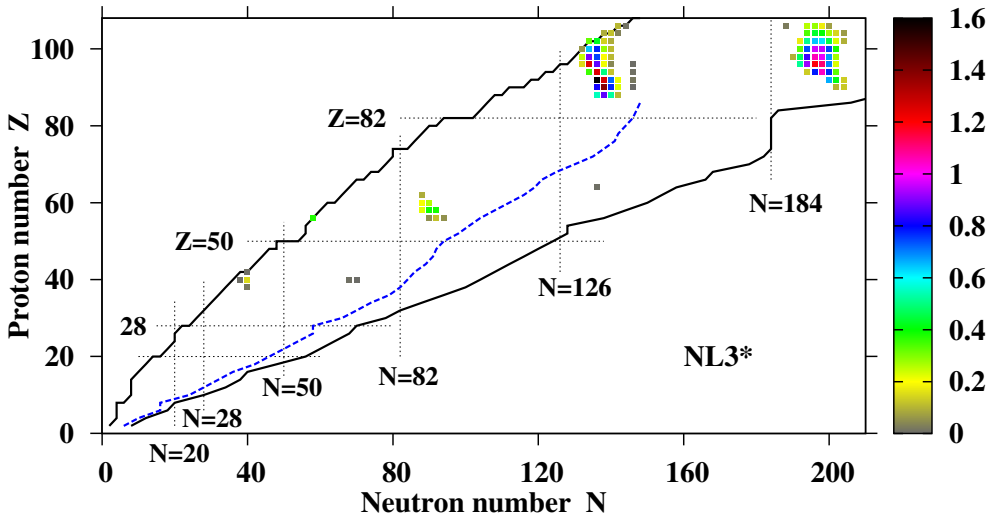

Figure 5.7

The same as in Fig. 5.6 but for NL3* CDFT.

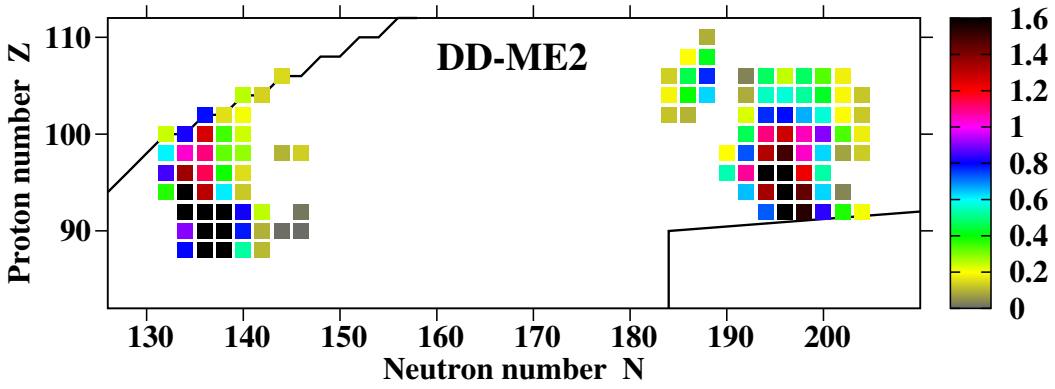

Figure 5.8

The same as in Fig. 5.6 but for $Z = 88 - 110$ with DD-ME2 CDFT.

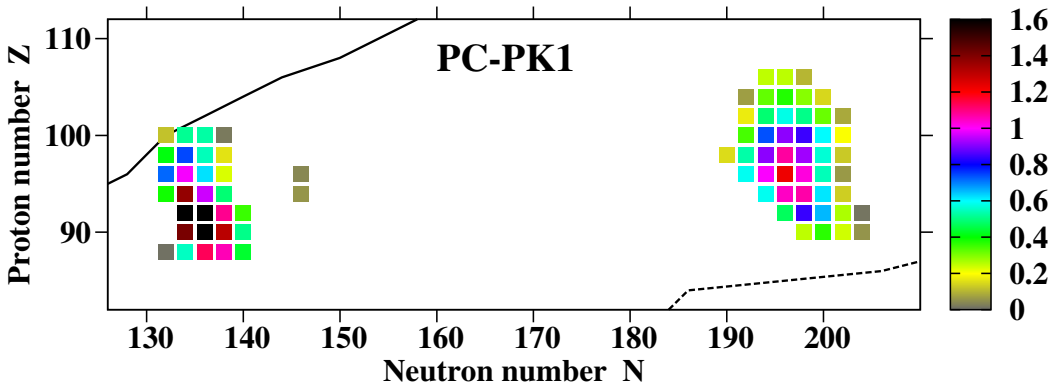

Figure 5.9

The same as in Fig. 5.8 but with PC-PK1 CDFT, and the dash line represent the neutron drip line for NL3*.

lines. Also systematic search for axial octupole deformation has been performed in the actinides and superheavy nuclei for proton numbers $Z = 88 - 126$ and neutron numbers from two-proton drip line up to $N = 210$ using four state-of-the-art covariant energy density functionals. The main results can be summarized as follows:

- The RHB calculations with the DD-PC1, PC-PK1 and DD-ME2 functionals correctly predict the islands of octupole deformation in the light lanthanides, actinides and light superheavy regions which in general agrees with available experimental data. The NL3* tends to place the centers (in the (Z, N) plane) of these three islands by two neutrons higher than in above mentioned functionals. The DD-MEδ functional fails to describe experimental data in the actinides.

- The gain in binding due to octupole deformation $|\Delta E^{oct}|$ is the quantity which defines the location and the extend of the islands of octupole deformation. If one excludes the DD-MEδ functional, theoretical uncertainties in its prediction are typi-

cally around 0.5 MeV; however, in some nuclei they reach 1 MeV. This leads to the differences in the predictions of the islands of octupole deformation. The most important source of these uncertainties is the difference in the prediction of underlying single-particle structure (see Ref. [198] for comparison of different DFTs).

- Comparing different functionals, one can see that the results obtained with the covariant energy density functional DD-MEδ differ substantially from the results of other functionals. The heights of the inner fission barriers in superheavy nuclei with $Z = 112-116$ obtained in this functional are significantly lower than the experimental estimates and the values calculated in all other models [188]. This functional is different from all the other functionals used here, because it has been adjusted in Ref. [28] using only four phenomenological parameters in addition to some input from ab initio calculations [199, 200]. All these facts suggest that either the ab initio input for this functional is not precise enough or the number of only four phenomenological parameters (fitted to masses of spherical nuclei) is too small to provide a proper description of the details of the single-particle structure.

CHAPTER VI

SUPERHEAVY NUCLEI: GROUND STATE PROPERTIES AND FISSION BARRIERS

6.1 Introduction

Science is driven by the efforts to understand unknowns. In low-energy nuclear physics many of such unknowns are located at the extremes of the nuclear landscape (see chapter III and Refs. [5, 84, 40]). The region of superheavy elements (SHE), characterized by the extreme values of proton number Z, is one of such extremes. Contrary to other regions of the nuclear chart, the SHEs are stabilized only by quantum shell effects. Because of this attractive feature and the desire to extend the nuclear landscape to higher Z values, this region is an arena of active experimental and theoretical studies.

Currently available experimental data reach proton number $Z = 118$ [31, 32] and dedicated experimental facilities such as the Dubna Superheavy Element Factory will hopefully allow to extend the region of SHEs up to $Z = 120$ and for a wider range on neutron numbers at lower Z values. But this facility will not be able to reach the predicted centers of the island of stability of SHEs at $(Z = 114, N = 184)$, $(Z = 120, N = 172/184)$ and $(Z = 126, N = 184)$ as given by microscopic+macroscopic (MM) approaches [201, 202, 203, 204, 205] or by covariant [206, 207, 52, 208] and Skyrme [204, 207] density functional theories (DFT), respectively.

Majority of systematic DFT studies of the shell structure of SHEs has been performed in the 90ies of the last century and at the beginning of the last decade. These studies indicate that the physics of SHEs is much richer in the DFT framework than in MM approaches. This is because of the self-consistency effects which are absent in the MM approaches. In the last ten years a new generation of energy density functionals has been developed in covariant [26, 27, 33, 79, 28] framework; they are characterized by an improved global performance (see chapter III and Ref. [40]). In addition, the experimental data on SHEs became much richer [209, 10] in these years.

For the reasons stated above it is necessary to reanalyze the structure of superheavy nuclei using both the full set of available experimental data on SHEs and the new generation of energy density functionals. The goals of this chapter are to (i) investigate the accuracy of the description of the ground state observables of known SHEs with the new generation of CEDF's NL3*, DD-ME2, DD-MEδ, DD-PC1 and PC-PK1 and to find whether the analysis of existing experimental data allows to distinguish the predictions of these CEDF's for nuclei beyond the known region of SHEs, and (ii) to investigate the fission barriers in superheavy nuclei with consideration of both the statistical and systematic theoretical uncertainties.

6.2 Numerical details

The axially symmetric RHB framework is used for systematic studies of all $Z = 96 - 126$ even-even actinides and SHEs from the proton-drip line (see Table 3.3 and Refs. [84, 40, 188]) up to neutron number $N = 196$. The theoretical details of the calculations

are explained in sec. 5.2 of chapter III. For each nucleus the potential energy curve is obtained in a large deformation range from $\beta_2 = -1.0$ up to $\beta_2 = 1.05$ in steps of $\beta_2 = 0.02$ by means of a constraint on the quadrupole moment Q_{20}. The effect of the octupole deformation on the binding energies of the ground states (and thus on the heights of inner fission barriers) is also taken into account according to the results obtained in Ref. [195]. Note that octupole deformation in the ground states affects fission barriers and their spreads only for the $Z \sim 92, N \sim 132$ and $Z \sim 96, N \sim 196$ nuclei.

For the fission barriers, we perform triaxial RHB (TRHB) calculations in a parity conserving cartesian oscillator basis [45, 210] using the same pairing. However, such calculations are enormously time-consuming. Therefore, they cannot be carried out on the same global scale as axial RHB calculations. As a result, we restricted the TRHB studies to a selected set of the $Z = 112 - 120$ nuclei. These nuclei are located mostly in the region where extensive experimental studies have either been already performed or will be performed in a foreseeable future. Even then the calculations of full potential energy surfaces (PES) are numerically prohibitive for the $N_F = 20$ fermionic basis. However, the topology of the PESs obtained in the TRHB calculations with the truncation of the fermionic basis at $N_F = 16$ and $N_F = 20$ is the same. Thus, full PESs have been calculated only with the $N_F = 16$ fermionic basis. These results define the positions in the deformation plane and the energies of axial and triaxial saddles. Afterwards, they are corrected for the $N_F = 20$ fermionic basis by performing the TRHB calculations with the $N_F = 20$ fermionic basis in the spherical/normal deformed minimum and at few grid points near the saddles.

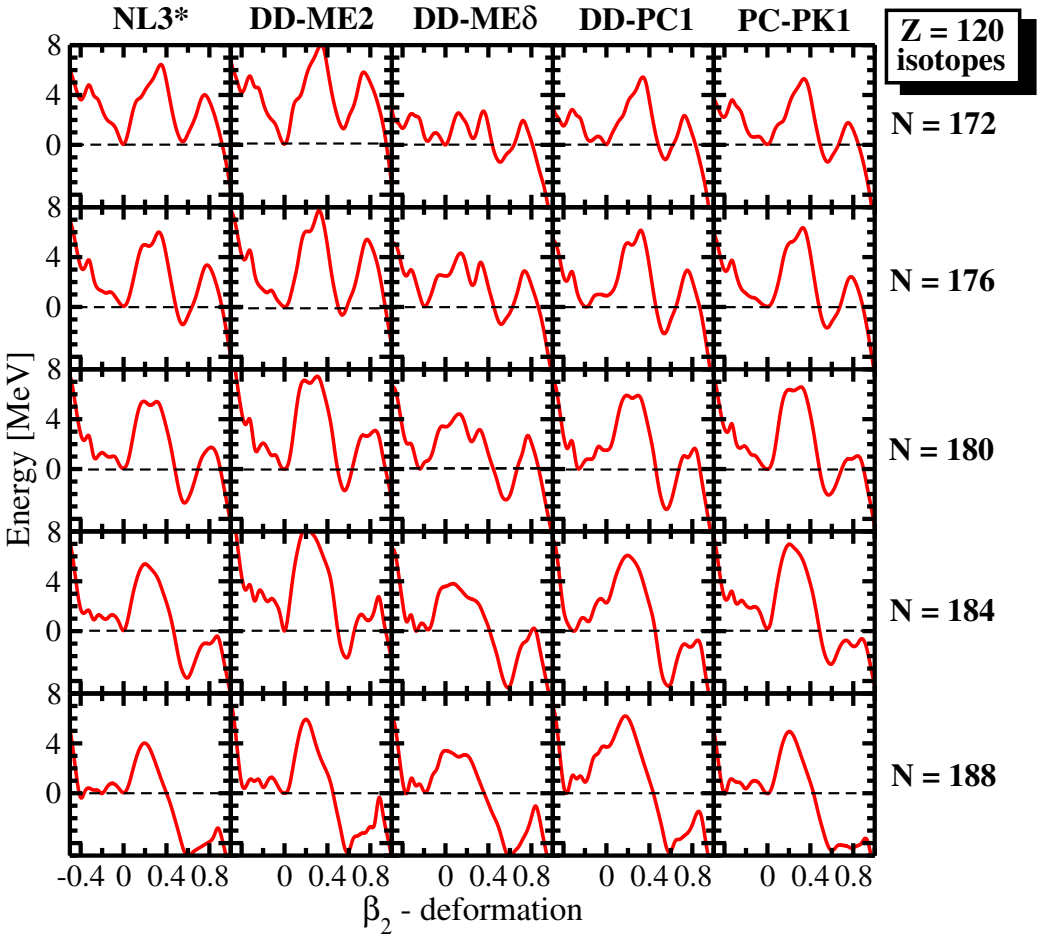

Figure 6.1

Deformation energy curves for the chain of $Z = 120$ isotopes obtained in axial RHB calculations.

6.3 The impact of deformation on the properties of superheavy nuclei

It is commonly accepted that the large spherical shell gaps at $Z = 120$ and $N = 172$ define the center of the island of stability of SHEs for the majority of the covariant functionals [207, 52]. But it is important to note that these conclusions were mostly obtained in investigations restricted to spherical shapes. Some calculations also suggest [211, 212], or do not exclude [52], the existence of a spherical shell gap at the neutron number $N = 184$. However, as discussed below, the inclusion of deformation can change the situation drastically for some functionals.

To illustrate this fact, the deformation energy curves of the $Z = 120$ isotopes are presented in Fig. 6.1. We restrict our considerations to the CEDFs, NL3*, DD-ME2, DD-MEδ, DD-PC1 and PC-PK1, whose global performance is well established in chapters III and V and Refs. [40, 80]. In the following discussion we neglect the prolate superdeformed minimum, which is sometimes even lower than the spherical or oblate minimum, because of discussions in Sec. IV.A of Ref. [188].

In Fig. 6.1 the lowest spherical or oblate minimum is considered as the ground state and indicated by a dashed horizontal line. It can be seen that the ground states of the $Z = 120$ isotopes with $N = 172 - 184$ are spherical for NL3*, DD-ME2, and PC-PK1. This is a consequence of the presence of the large $Z = 120$ spherical shell gap (see Fig. 1 of Ref. [188]). For these three functionals, the increase of neutron number N leads to softer potential energy curves for β_2 values between -0.4 and 0.0. As a result, for $N = 188$ an oblate minimum either becomes lowest in energy (for NL3*) or competes in energy with the spherical solution (for DD-ME2 and PC-PK1). This softness of the

potential energy curves is even more pronounced for the DD-MEδ and DD-PC1, for which the oblate solution is lower in energy than the spherical solution in all displayed nuclei apart from $N = 172$ (Fig. 6.1).

It is tempting to relate this feature to the fact that the size of the $Z = 120$ gap is smallest among the employed functionals for DD-MEδ in the $(Z = 120, N = 172)$ nucleus and for DD-PC1 in the $(Z = 120, N = 184)$ nucleus (see Fig. 1 of Ref. [188]), this explanation is too simplistic. This is because even for the cases when the sizes of the $Z = 120$ gap are very similar, the deformations of their minima in the ground state are different. This strongly suggest that the evolution of the single-particle structure with deformation, which leads to negative shell correction energies at oblate shape, is responsible for the observed features. Thus, not only the size of the spherical shell gaps but also the location of the single-particle states below and above these gaps is responsible for the observed features.

It is important to recognize that contrary to the spherical states with a degeneracy of $2j + 1$, deformed states are only two-fold degenerate. This will also impact the shell correction energy since it depends on the averaged density of the single-particle states in the vicinity of the Fermi surface [213, 214, 215]. As a result, close to the deformed shell gaps the negative shell correction energy can be larger in absolute value than the one at spherical shape even for similar sizes of the respective deformed and spherical shell gaps. This difference can be sufficient to counteract the increase of the energy of the liquid drop with increasing oblate deformation in SHEs [216]. The consequences of this interplay between shell correction and liquid drop energies and the role played by the low level density of the single-particle states in the vicinity of deformed shell gaps are clearly visible

in the potential energy curves of the $^{304}120$ nucleus presented in Fig. 6.1 for DD-PC1 and NL3*. For DD-PC1, the ground state is oblate with deformation $\beta_2 \sim -0.3$. However, two excited minima are also seen at $\beta_2 \sim -0.15$ and $\beta_2 = 0.0$. Although the ground state of the nucleus $^{304}120$ is spherical for NL3*, three minima at $\beta_2 \sim -0.4$, $\beta_2 \sim -0.3$, and $\beta_2 \sim -0.2$ are seen at excitation energies of around 1 MeV. These local minima are the consequence of the fact that the corresponding minima in the proton and neutron shell correction energies correspond to different deformations.

6.4 The systematics of the deformations

The calculated charge quadrupole deformations of the ground states for PC-PK1 and DD-PC1 CEDFs are plotted in Figs. 6.2 and 6.3 respectively. Experimentally known nuclei are shown by open circles.The information on experimentally known nuclei is taken from Refs. [10, 11]. They are shown for the $Z = 96 - 126$ nuclei located between the two-proton drip line (see Table 3.3 and Table IV in Ref. [40]) and $N = 196$. The width of the gray region along a specific particle number corresponding to a shell closure indicates the impact of this shell closure on the structure of neighbouring nuclei. Looking at the PC-PK1 functional, the width of such a band at $Z \approx 120$ is on average two even-even nuclei in the Z direction for $N = 172 - 188$ and the width of a corresponding band at $N \approx 184$ is on average four even-even nuclei in the N direction for $Z = 96 - 122$ (see Fig. 6.2). This is contrary to existing discussions in CDFT which emphasize the impact of the $N = 172$ shell gap over the $N = 184$ gap. Similar features exist in the calculations with NL3* and

DD-ME2 (See Fig. 6a and b of Ref. [188]). However, the impact of the $Z = 120$ and $N = 184$ spherical shell gaps becomes less pronounced for DD-ME2.

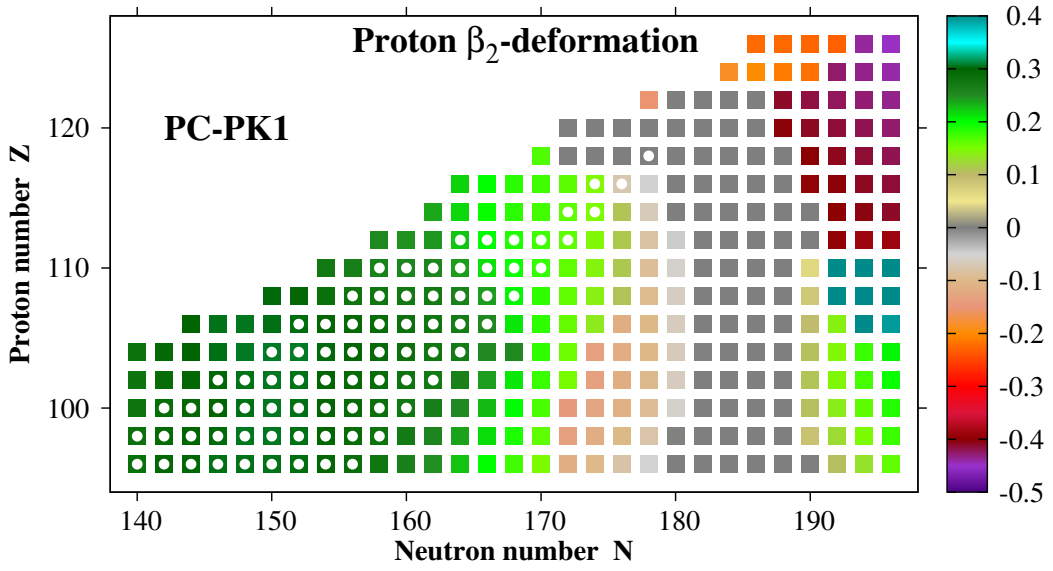

Figure 6.2

Charge quadrupole deformations β_2 obtained with PC-PK1 CEDF.

The impact of the $Z = 120$ spherical shell gap is significantly reduced for DD-PC1 CEDF; only the $N = 172$ nuclei with $Z = 118$ and 120 are spherical for this functional (see Fig. 6.3). The impact of the $N = 184$ shell gap is also considerably decreased; the ground states of the $N = 184$ nuclei are spherical only for $Z \leq 112$. The band of spherical nuclei around $N = 184$ is narrow for DD-PC1. A similar situation exist in the calculation with DD-MEδ (see Fig. 6c of Ref. [188]). These results are in contradiction to the expectation that the large size of the spherical $Z = 120$ gap forces the isotopes with $Z = 120$ to be spherical for a large range of neutron numbers.

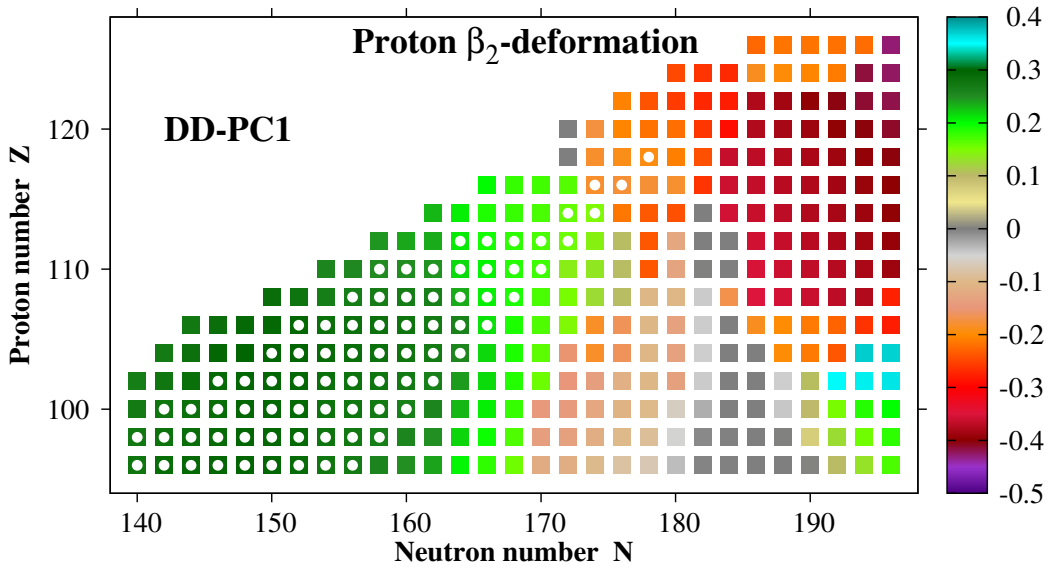

Figure 6.3

Same as Fig. 6.2 but with DD-PC1 CEDF.

Figs. 6.2 and 6.3 also shows experimentally known nuclei indicated by open circles. One can see that, apart from the $Z = 116, 118$ nuclei, the predictions of these two functionals (PC-PK1 and DD-PC1) for the equilibrium deformations of experimentally known even-even nuclei are very similar. For these nuclei, PC-PK1 predicts the gradual transition from prolate to spherical shape on going from $Z = 114$ to $Z = 118$. On the contrary, for DD-PC1 the transition from the prolate to oblate minimum is predicted for experimentally known nuclei on going from $Z = 114$ to $Z = 116$ and all experimentally known $Z \geq 116$ nuclei are expected to be oblate. But because of the limited scope of experimental data these differences in the description of experimentally known $Z = 116$ and 118 nuclei between DD-PC1/DD-MEδ and PC-PK1/NL3*/DD-ME2 cannot be discriminated.

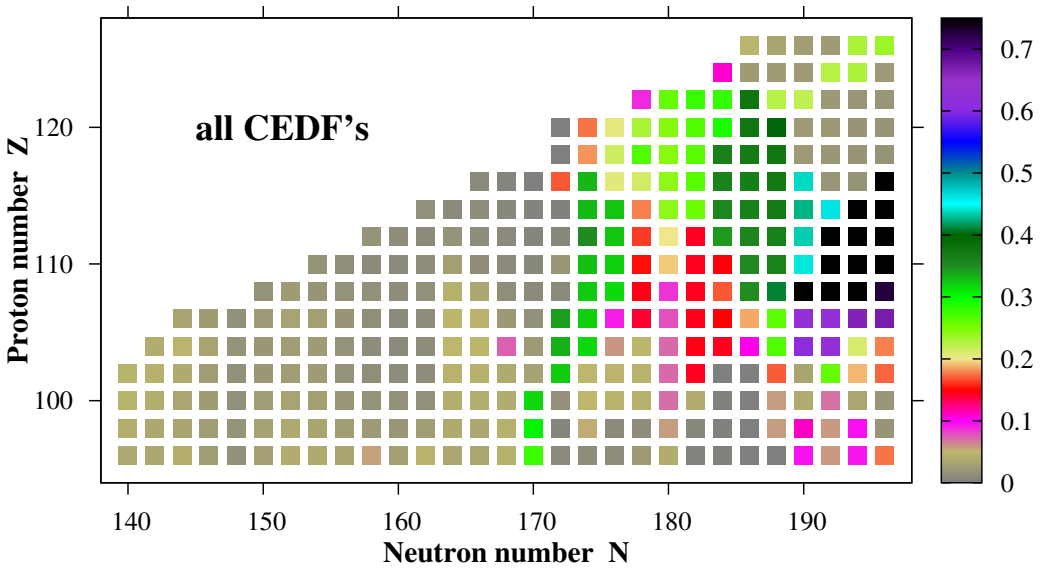

Figure 6.4

Proton quadrupole deformation spreads $\Delta\beta_2$ as a function of proton and neutron number.

Fig. 6.4 shows the spreads in the theoretical predictions of the charge quadrupole deformations. They are very small in the region of known nuclei and for $N < 170$. Only few experimentally known nuclei are located in the region where substantial theoretical spreads exist. However as discussed earlier, available experimental data on these nuclei does not allow to discriminate different predictions. Large spreads exist in the region near the $Z = 120$ and $N = 184$ lines. This is because spherical ground states are predicted in this region by NL3*, DD-ME2 and PC-PK1, while DD-MEδ and DD-PC1 favor oblate shapes in these nuclei. Very large spreads exist in the $Z \sim 110, N \geq 190$ region; this is a region where a transition from prolate to oblate shape is seen in the calculations and it takes place at different positions in the (Z, N) chart for the different functionals (see Figs . 6.2 and 6.3). The theoretical spreads become small again in the upper right corner of the

chart; here they are substantial only in several nuclei (shown by green color) which form a "line" parallel to the two-proton drip line. This "line" is a consequence of the fact that the transition from ground state deformations $\beta_2 \sim -0.2$ to $\beta_2 \sim -0.4$ takes place for different functionals at different positions in the (N, Z) chart.

6.5 Masses and separation energies

Table 6.1

rms-deviations $\Delta E_{\rm rms}$, $\Delta(S_{2n})_{\rm rms}$ and $\Delta(S_{2p})_{\rm rms}$ between calculated and experimental data.

CEDF	ΔE_{rms} [MeV]	$\Delta(S_{2n})_{rms}$ [MeV]	$\Delta(S_{2p})_{rms}$ [MeV]
1	2	3	4
NL3*	3.02/3.39	0.71/0.68	1.33/1.34
DD-ME2	1.39/1.40	0.45/0.54	0.85/0.90
DD-MEδ	2.52/2.45	0.60/0.51	0.45/0.48
DD-PC1	**0.59/0.74**	0.30/0.32	0.41/0.42
PC-PK1	2.82/2.63	**0.25/0.23**	**0.36/0.33**

In Table 6.1 we list the rms-deviations $\Delta E_{\rm rms}$ $\Delta(S_{2n})_{\rm rms}$ and $\Delta(S_{2p})_{\rm rms}$ between calculated and experimental binding energies E, two-neutron and two-proton separation energies S_{2n} and S_{2p}. The values of physical observables in the columns 2-4 are presented in the following format "A/B", where A are the values obtained from only measured masses and B from measured+estimated masses. Only experimental data on even-even nuclei with $Z \geq 96$ is used here. In each column, bold style is used to indicate the functional with the best rms-deviation. For each employed functional the accuracy of the description of

the sets of measured and measured+estimated masses is comparable and does not change substantially when the estimated masses are added to the measured ones.

As compared with the global analysis of Sec .3.3 of chapter III and Refs. [40, 80], the accuracy of the description of masses is better for DD-PC1 and DD-ME2, comparable for DD-MEδ and PC-PK1 and worse for NL3*. The best accuracy is achieved for DD-PC1. This is not surprising considering that this functional has been carefully fitted to the binding energies of deformed rare-earth nuclei and actinides in Ref. [27]. With respect to masses it outperforms other functionals in these regions (see Figs. 6 and 7 in Ref. [40]). The two-neutron S_{2n} and the two-proton S_{2p} separation energies are described with a typical accuracy of 0.5 MeV (Table 6.1). This is better by a factor of two than the global accuracy of around 1 MeV obtained for these functionals in chapter III and Ref .[40]. The accuracy of the description of separation energies depends on the accuracy of the description of mass differences. As a result, not always the functional which provides the best description of masses gives the best description of two-particle separation energies.

6.6 α-decay properties

In superheavy nuclei spontaneous fission and α emission compete and the shortest half-live determines the dominant decay channel and the total half-live. Only in the cases where the spontaneous fission half-live is longer than the half-live of α emission can superheavy nuclei be observed in experiment. In addition, only nuclei with half-lives longer than $\tau = 10\mu$s are observed in experiments.

The α decay half-live depends on the Q_α values which are calculated according to

$$Q_\alpha = E(Z,N) - E(Z-2,N-2) - E(2,2) \tag{6.1}$$

with $E(2,2) = -28.295674$ MeV [12] and Z and N representing the parent nucleus.

The RHB results for the Q_α values are compared with experiment in Fig. 6.5 for DD-PC1 functional. The experimental and calculated values are shown by symbols and lines, respectively. For a given isotope chain, the same color is used for both types of values. Experimental Q_α values are from Ref. [12]. Solid symbols are used for experimentally measured Q_α values [12] which are determined either from measured masses (for low-Z values) or from α-decays (for high-Z values). Open symbols are used for the Q_α values the determination of which involves at least one estimated mass. The rms-deviations for the five functionals used in this chapter are listed in Table 6.2. Based on the results presented in this table, the best agreement is obtained for PC-PK1 closely followed by DD-PC1 and DD-MEδ, and then by DD-ME2 and NL3*. The reproduction of the magnitude of $N = 162$ peak is obtained for DD-PC1, PC-PK1 and DD-ME2 CEDFs whiles NL3* CEDF somewhat underestimate its magnitude. The DD-MEδ CEDF completely misses both the position in neutron number and the magnitude of the peak at $N = 164$ seen in the experimental data for the Rf, Sg, Hs, and Ds isotope chains (see. Fig. 14c of Ref. [188]).

The α-decay half-lives were computed using the phenomenological Viola-Seaborg formula [217]

$$log_{10}\tau_\alpha = \frac{aZ+b}{\sqrt{Q_\alpha}} + cZ + d \tag{6.2}$$

with the parameters $a = 1.64062$, $b = -8.54399$, $c = -0.19430$ and $d = -33.9054$ of Ref. [218].

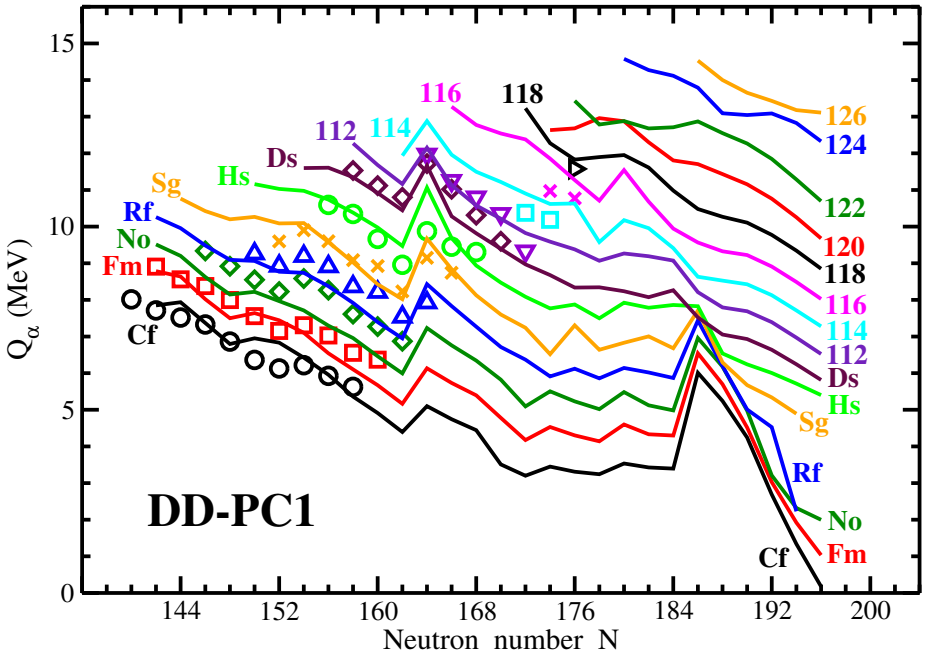

Figure 6.5

The comparison of experimental and calculated Q_α values for even-even superheavy nuclei.

The comparison of calculated and experimental half-lives for the α-decays is presented in Fig. 6.6 for DD-PC1 CEDF. The experimental and calculated values are shown by symbols and lines, respectively. For a given isotope chain, the same color is used for both types of values. The experimental data are from Ref. [13]. It can be seen that there is a reasonable agreement between experimental and theoretical results. However, the local increase above the general trend of the experimental half-lives near $N = 152$ visible in the Cf, Fm and No isotope chains, which is due to deformed $N = 152$ shell gap, is not

reproduced. For higher neutron numbers all functionals predict an increase of the half-lives as a function of neutron number N. This trend is however interrupted in the vicinity of the spherical shell gap with $N = 184$. For some isotope chains a drastic decrease of the half-lives is observed. It is a consequence of the well known fact that for nuclei with two neutrons outside a closed shell α-particle emission is easier than for the other nuclei in the same isotopic chain [219]. However, above $N = 184$ the trend of increasing half-lives with the increase of neutron number is restored. The impact of the $N = 184$ shell gap on the α-decay half-lives clearly correlates with the impact of this gap of the deformations of the ground states. In SHEs with high Z values its impact on the α-decay half lives is either substantially decreased or completely vanishes.

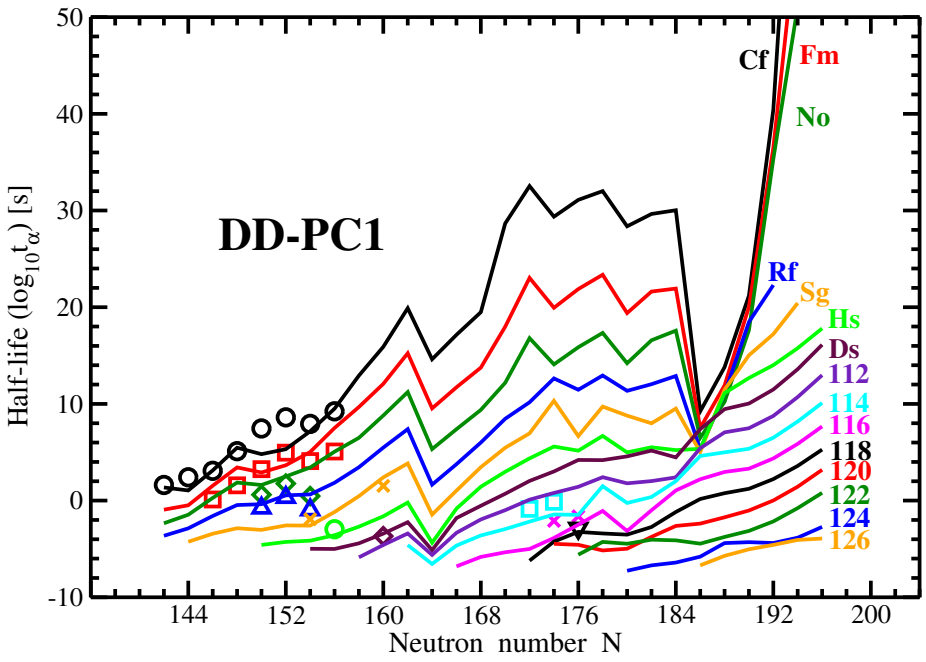

Figure 6.6

Experimental and calculated half-lives for α-decays of even-even superheavy nuclei.

Table 6.2

Same as Table 6.1 but for $\Delta(Q_\alpha)_{rms}$ and $\Delta(\tau_\alpha)_{rms}$. In the last column, the deviations are given in terms of orders of magnitude.

CEDF	$\Delta(Q_\alpha)_{rms}$ [MeV]	$\Delta(\tau_\alpha)_{rms}$ [order]
1	2	3
NL3*	0.68/0.75	2.44
DD-ME2	0.51/0.65	1.95
DD-MEδ	0.39/0.51	1.39
DD-PC1	0.36/0.47	1.40
PC-PK1	**0.32/0.38**	**1.26**

In the region under investigation the magnitude of the α decay half-lives varies in a very wide range from 10^{-8} up to 10^{50} s (or even higher for the Cf, Fm and No nuclei with $N \sim 190$). For some SHEs with high-Z values the calculated half-lives fell below the experimental observation limit of 10^{-5}s.

Despite the fact that the existing experimental data on the α-decay half-lives is described with comparable accuracy by the different functionals, for unknown regions of nuclear chart there are some cases of substantial difference in their predictions. The most extreme difference is seen in the Cf isotopes, where NL3* and DD-ME2 differ from DD-MEδ and DD-PC1 by approximately 20 orders of magnitude at neutron number $N = 184$ and slightly below it. On the other hand, apart from the $N = 184$ region the differences in the predictions of different functionals is smaller for SHEs with $Z \sim 114$ where it reaches only few orders of magnitude (see Fig . 6.6 and Fig. 15 of Ref . [188]). In the $N = 184$ region of these nuclei the differences between predictions of different functionals increase by additional few orders of magnitude. However, above $Z = 120$ these differences decrease

with increasing proton number because of the diminishing role of the $N = 184$ spherical shell gap.

6.7 Fission barriers of superheavy nuclei

As already stated earlier, the stability of SHEs is defined by the fission barriers. In addition, the experimental studies of SHEs are based on the observation of α-decays. But the α-decays properties have been discussed in the previous section. Therefore it is of great importance to study the fission barriers in SHEs to be able to make a solid conclusions on the stability of SHEs in the DFT using CEDFs.

6.7.1 Global investigation of inner fission barriers and related systematic theoretical uncertainties in the axial RHB calculations

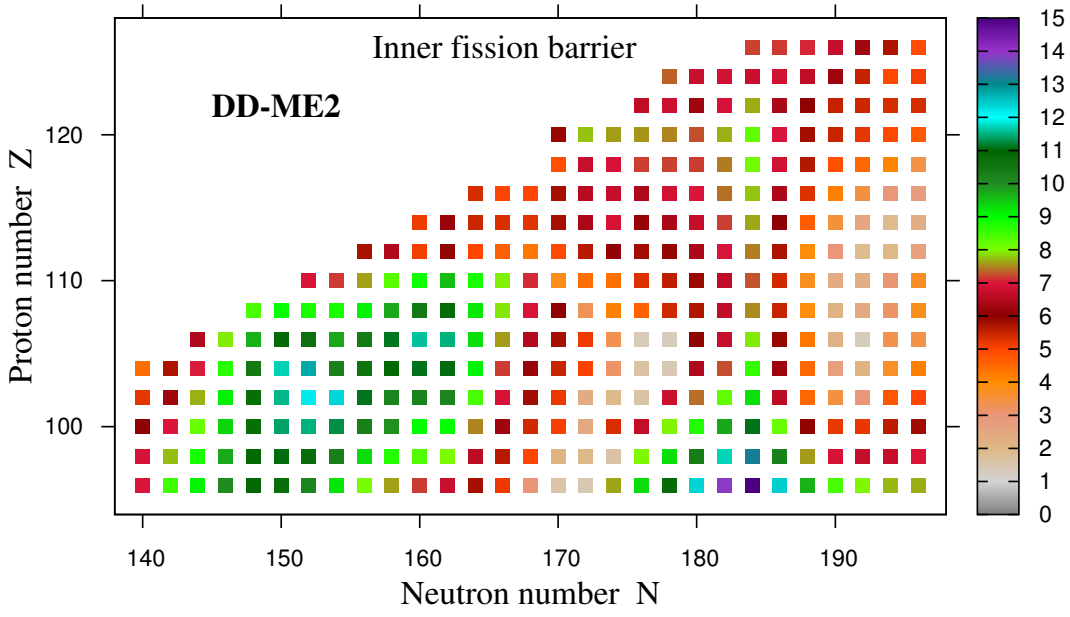

Figure 6.7

The heights of inner fission barriers (in MeV) with DD-ME2 CEDF.

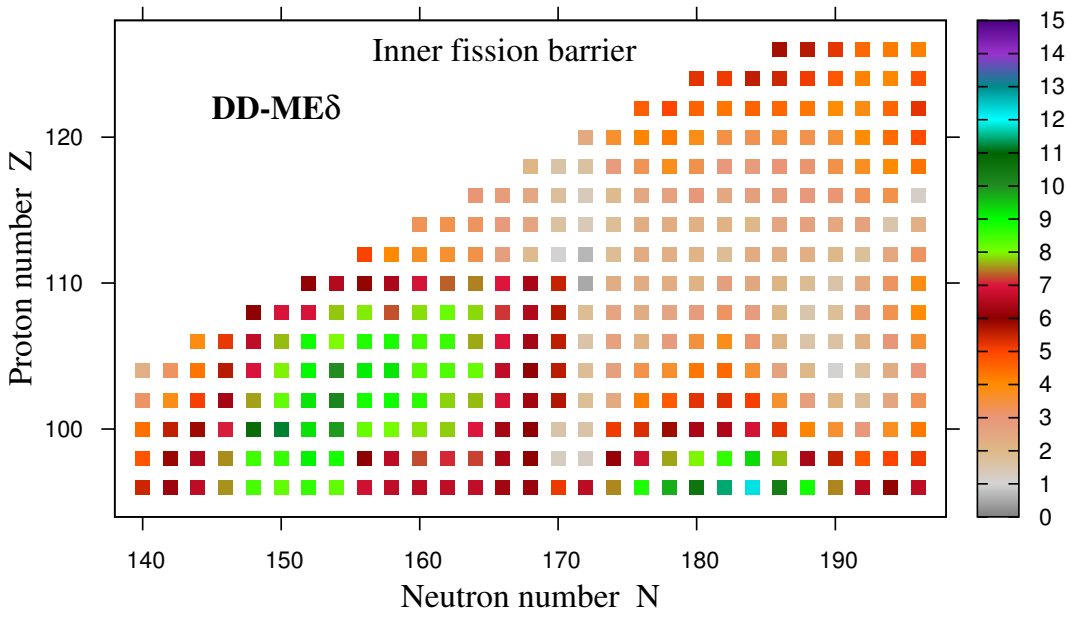

Figure 6.8

Same as Fig. 6.7 but with DD-MEδ CEDF.

The global behavior of the inner fission barrier heights in the region of superheavy nuclei obtained in axially symmetric RHB calculations as a function of proton and neutron number is shown in Figs. 6.7 and 6.8 for the DD-ME2 and DD-MEδ functionals, respectively. These two functionals produce the highest and lowest fission barriers respectively among the five employed CEDFs. The results of the calculations for the DD-ME2 and DD-MEδ CEDFs are shown from the two-proton drip line up to $N = 196$

As already stated the functionals used in this chapter can be split into two group with the first group consisting of NL3*, DD-ME2 and PC-PK1, which predicts bands of spherical SHEs in the (Z, N) plane centered around the $Z = 120$ and $N = 184$ lines. And the second group which is made up of DD-MEδ and DD-PC1 and does not predict spherical SHE in

the vicinity of above mentioned particle numbers. The impact of the proton and neutron spherical shell gaps at $Z = 120$ and $N = 184$ is very visible for DD-ME2 (see Fig .6.7); there is a substantial increase of the inner fission barrier heights around these numbers. In contrast, no such effect is seen in the calculations with DD-MEδ (see Fig .6.8).

The spreads in the predictions of inner fission barrier heights are shown for all five employed functionals in Fig. 6.9. One can see that in the actinides ($Z \leq 100, N \leq 164$) these spreads are typically smaller than 2.5 MeV. Note that in this mass region theoretical uncertainties in the prediction of the ground state deformations are very small (see Fig. 6.4 and Refs. [40, 188]). However, the ΔE^B spreads drastically increase in the $Z = 112-120, N = 170-186$ region where they range from 3.5 MeV up to 5.5 MeV. To a large extent this region coincides with the region where the uncertainties in the predictions of the ground state deformations are substantial (see Fig. 6.4 and Fig. 8 in Ref. [188]). This clearly suggests that in this region the uncertainties in the fission barrier heights are strongly affected by the uncertainties in the ground state deformations. A similar enhancement of the ΔE^B spreads is seen in the nuclei around $Z \sim 98, N \sim 174$. However, the differences in the predictions of the ground state deformations play here a minor role since they are almost the same for all functionals (see Fig. 6.4 and Fig. 8 in Ref. [188]). Theoretical ΔE^B spreads decrease for $N \geq 186$; here they are typically less than 3 MeV with only a few nuclei characterized by higher spreads of around 4 MeV.

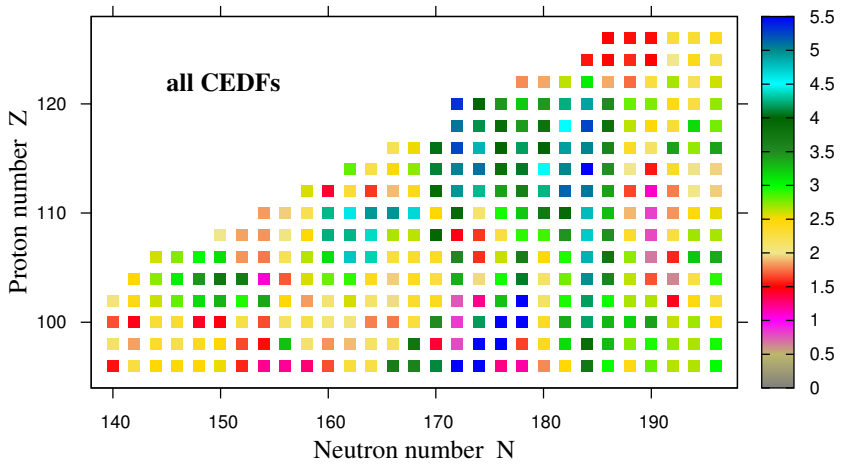

Figure 6.9

The spreads ΔE^B of the heights of inner fission barriers as a function of proton and neutron number.

6.7.2 Systematic theoretical uncertainties in the description of inner fission barriers for triaxial RHB calculations

It is well-known that inner fission barriers in many SHEs are affected by triaxiality; its impact is especially pronounced in the nuclei near the $Z = 120$ and $N = 184$ (see Table V in Ref. [70]). Thus, the axial RHB calculations provide an upper limit for the inner fission barrier heights.

In general, triaxial deformation has to be included into the calculations for a more realistic estimate of the heights of inner fission barriers which can be used for the comparison with experiment. However, such a study requires tremendous computational power. The computational challenge becomes especially large in the case of the analysis of systematic theoretical uncertainties because the same nucleus has to be calculated within the TRHB framework for several CEDFs. Thus, a full global analysis of theoretical uncertain-

ties similar to the one presented in Sec .6.7.1 in the axial RHB framework is, at present, beyond the reach of available computational facilities. As a result, we concentrate here on the selected set of the $Z = 112 - 120$ superheavy nuclei which will be in the focus of experimental studies within the next decades. They are shown in Figs 6.11 and 6.12. In the selection of nuclei we focus on the nuclei in which the triaxial saddle is expected to be the lowest in energy in the region of interest. According to systematic studies in the RMF+BCS framework with the CEDF NL3* of Ref. [70], these are the nuclei in the vicinity of the $Z = 120$ and $N = 184$ lines. On the contrary, the axial saddles are the lowest in energy in the nuclei which are away from these lines. For example, this takes place for $N \leq 174$ in the $Z = 112, 114, 116$ nuclei (see Ref. [70]). Triaxial RHB calculations for the $(Z = 112, N = 164)$, $(Z = 112, N = 172)$, $(Z = 114, N = 166)$ and $(Z = 114, N = 172)$ nuclei (these nuclei are seen on the left side of Fig. 6.11) confirm this observation of Ref. [70] for all CEDFs employed in the present manuscript. We will try to establish (i) how theoretical systematic uncertainties obtained in axial RHB calculations will be modified when triaxiality is included and (ii) to what extent theoretical uncertainties obtained in axial and triaxial RHB calculations are correlated.

The dependence of the potential energy surfaces on the CEDF is illustrated in Fig. 6.10. These PES are characterized by a complicated topology which, however, reveals some typical triaxial saddles. The energy difference between two neighboring equipotential lines is equal to 0.5 MeV. The Ax, Ax-Tr, Tr-A and Tr-B saddles are shown by blue/red circles, diamonds, triangles, and squares, respectively. The PES are shown in the order of decreasing height of inner fission barrier.

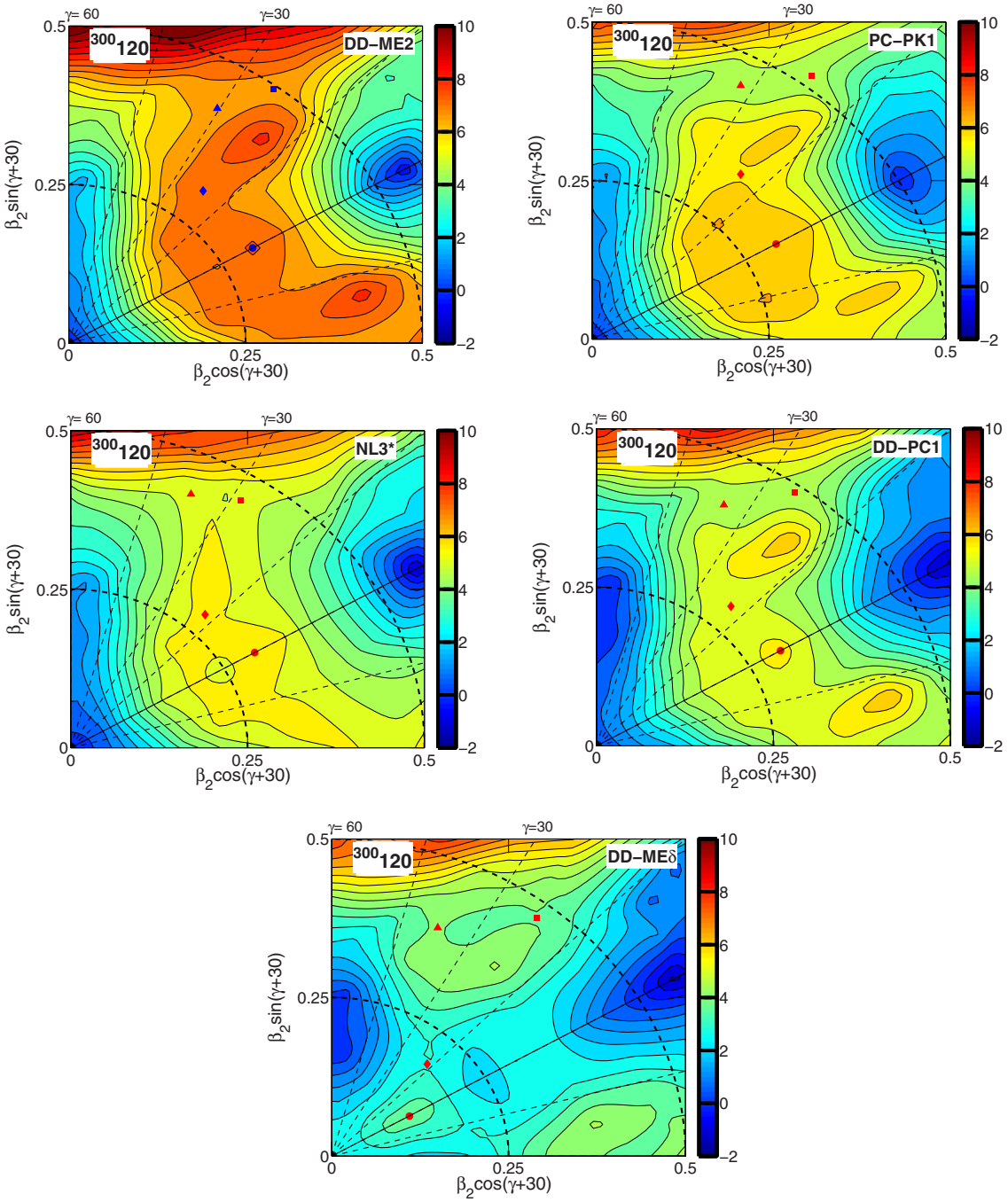

Figure 6.10

Potential energy surfaces of the $^{300}120$ nucleus as obtained in the calculations with indicated CEDFs.

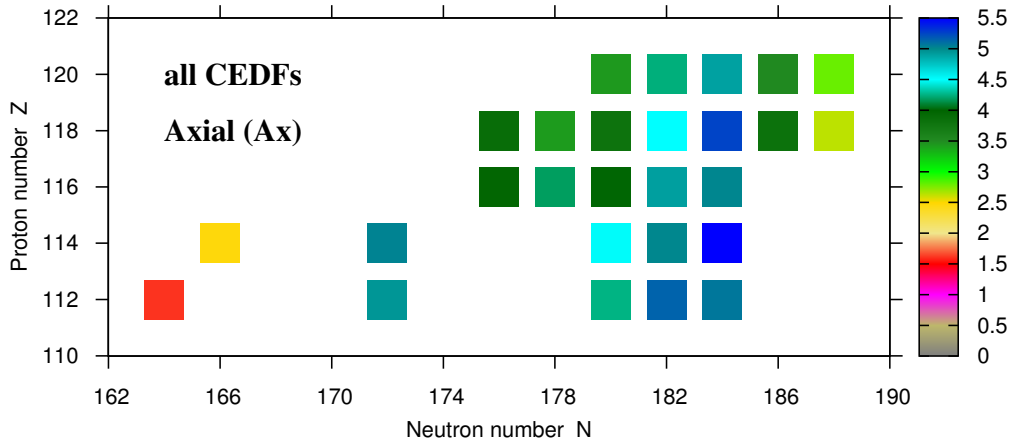

Figure 6.11

The spreads ΔE^S of the energies of axial saddles for a selected set of the $Z = 112 - 120$ nuclei as a function of proton and neutron number.

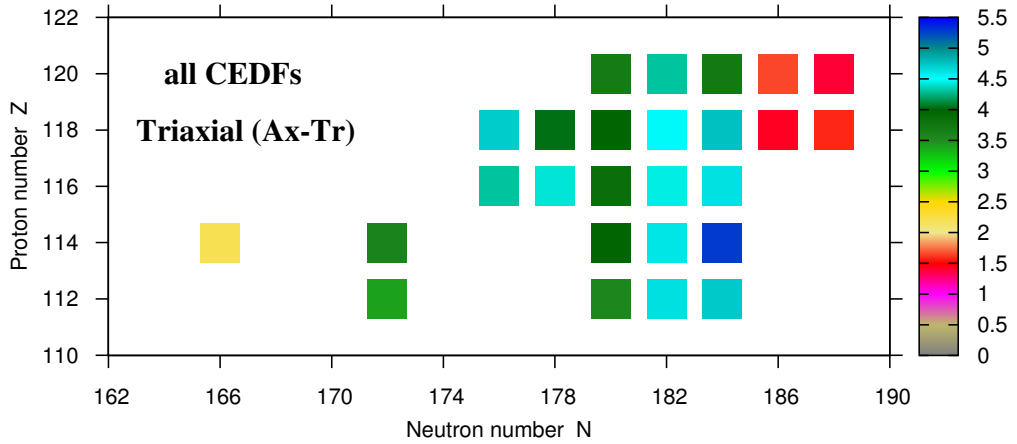

Figure 6.12

Same as Fig .6.11 but for TRHB calculations.

In the nucleus ^{300}120 they are located at $(\beta_2 \sim 0.32, \gamma \sim 21^\circ)$, $(\beta_2 \sim 0.43, \gamma \sim 33^\circ)$, and $(\beta_2 \sim 0.49, \gamma \sim 24^\circ)$ for the functionals DD-ME2, PC-PK1, NL3* and DD-PC1 (see Fig. 6.10). The later two are also visible in the CEDF DD-MEδ. However, the first one is shifted to smaller β_2 and γ deformations, namely, to $(\beta_2 \sim 0.20, \gamma \sim 15^\circ)$.

For all functionals except DD-MEδ the axial saddle is higher in energy by roughly 0.5 MeV than the triaxial saddle at $(\beta_2 \sim 0.32, \gamma \sim 21^\circ)$ and by approximately 1.5 MeV than the triaxial saddles at $(\beta_2 \sim 0.43, \gamma \sim 33^\circ)$ and $(\beta_2 \sim 0.49, \gamma \sim 24^\circ)$ (Fig. 6.10). The PES of the DD-MEδ functional has a completely different topology. Although the $(\beta_2 \sim 0.20, \gamma \sim 15^\circ)$ saddle is lower in energy than the axial saddle by approximately 1 MeV, the axial saddle is located only ~ 0.2 MeV below the triaxial saddles at $(\beta_2 \sim 0.33, \gamma \sim 25^\circ)$ and $(\beta_2 \sim 0.45, \gamma \sim 33^\circ)$.

The presence of these saddles leads to several fission paths which have been discussed in detail in Ref. [70]. Although this discussion is based on RMF+BCS results with NL3*, we found that it is still valid for the TRHB results with DD-ME2, PC-PK1, NL3* and DD-PC1. This is because for a given functional the topology of PES obtained in triaxial RMF+BCS and RHB calculations is similar. The situation is different for DD-MEδ which has an axial saddle located at $\beta_2 \sim 0.13$ (Fig. 6.10). Thus, the fission path will proceed from the oblate minimum via the triaxial saddle at $(\beta_2 \sim 0.20, \gamma \sim 0.15)$ which has a low excitation energy of only 3 MeV.

The accounting of triaxiality in the calculations modifies the spreads in the predictions of the heights of inner fission barriers. This is clearly seen in Figs 6.11 and 6.12 where these spread, obtained in axial and triaxial RHB calculations, are compared. Although,

locally, the two calculations may differ slightly, on average, there are strong correlations in the spreads obtained in the two calculations. This suggests that also for other regions of the nuclear chart, not covered by the present triaxial RHB calculations, the spreads in inner fission barrier heights obtained in the axial RHB calculations (See Fig .6.9) could be used as a reasonable estimate of the spreads which would be obtained in the calculations with triaxiality included.

6.8 Concluding remarks

The performance of covariant energy density functionals in the region of superheavy nuclei has been assessed using the state-of-the-art functionals NL3*, DD-ME2, DD-MEδ, DD-PC1, and PC-PK1. The available experimental data on ground state properties of even-even superheavy nuclei have been confronted with the results of the calculations. Theoretical spreads in the predictions of physical observables and fissions barriers have been investigated in a systematic way in this region of the nuclear chart for covariant density functionals.

The main results of this chapter can be summarized as follows:

- Available experimental data (separation energies, Q_α-values and α-decay half-lives) on SHEs are described with comparable accuracy. Comparing different functionals one can see that the results obtained with the covariant density functional DD-MEδ differ substantially from the results of other functionals. This functional is different from all the other functionals used here, because it has been adjusted in Ref. [28]

using only four phenomenological parameters in addition to some input from ab-inito calculations [199, 200].

- Theoretical uncertainties in the predictions of different observables have been quantified. While the uncertainties in the quadrupole deformation of the ground states of known superheavy nuclei are small, they increase on approaching nuclei with $Z = 120$ and/or $N = 184$. As a result, even the ground state deformations of these nuclei (whether spherical or oblate) cannot be predicted with certainty. Available experimental data do not allow to discriminate between these predictions.

- Systematic theoretical uncertainties in the predictions of inner fission barriers and their propagation towards unknown regions of higher Z values and of more neutron-rich nuclei have been quantified. These uncertainties are substantial in SHEs. It is clear that the differences in the basic model assumptions such as the range of the interaction and the form of the density dependence together with the different fitting protocols based only on nuclear matter and bulk properties data lead to these uncertainties.

CHAPTER VII

COVARIANT ENERGY DENSITY FUNCTIONALS: NUCLEAR MATTER CONSTRAINTS

7.1 Introduction

Bound states of the nucleons manifest themself in two species: finite nuclei and neutron stars. The former system is bound by strong forces, while the latter by gravitational ones. The description of both types of nuclear systems is intimately connected with a concept of nuclear matter which is an idealized infinite system of nucleons (neutrons and protons) interacting by strong forces. Infinite volume implies no surface effects and translational invariance. This concept is well suited for the description of the properties of interior of neutron stars.

However, it also has some important implications for finite nuclei (see Refs. [220, 221, 222, 223, 224] in recent topical review on nuclear symmetry energy). This is because the constraints on nuclear matter properties (NMP) enter into fitting protocols of the energy density functionals (EDF) for non-relativistic and covariant density functional theories [144, 29]. In this way they affect the properties of finite nuclei (both static and dynamic aspects) [144, 29, 220, 221, 222, 223].

Analysis of the 263 covariant energy density functionals with respect of NMP constraints has recently been performed in Ref. [1]. Small portion of these functionals (less

than 10) have been used in a more or less systematic studies of the properties of finite nuclei. The properties of symmetric nuclear matter, pure neutron matter, symmetry energy and its derivatives were constrained based on experimental/empirical data and model calculations in Ref. [1]. This resulted in two sets of constraints called SET2a and SET2b relevant for CDFT models; the part of these constraints is listed in Table 7.2 below.

Among these 263 CEDFs only 4 and 3 satisfy SET2a and SET2b NMP constraints, respectively. However, these functionals have never been used in the studies of finite nuclei. Therefore, it is impossible to verify whether good NMP of these functionals will translate into good global description of binding energies, charge radii, deformations etc. The FSUGold and DD-MEδ CEDFs are among the 263 CEDFs. The global performance of these functionals have been studied in the RMF+BCS and RHB models in Refs. [75, 40], respectively. Additional constraints on the functionals come from the properties of neutron stars [225]. It turns out that FSUGold and DD-MEδ place maximum mass M of neutron star well below and above the measured limit of $1.93 \leq M/M_{\odot} \leq 2.05$ [226, 227] where $M_{\odot}$ is the solar mass. The DD-MEδ functional comes to this limit only when hyperons are included; however, there are substantial uncertainties in the meson-hyperon couplings [225] as well as in the existence of hyperons in the interior of neutron stars [228].

Thus, the number of questions emerge. Firstly, whether strict enforcement of these NMP constraints will inevitably lead to an improvement of the description of the ground state properties of finite nuclei in the CDFT and to a reduction of theoretical uncertainties in the description of the properties of neutron-rich nuclei. The second question is whether there are some physics missing in the current generation of CEDFs which could be re-

sponsible for some mismatch of the results for finite nuclei and neutron stars. Also it is important to understand how the details of the fitting protocols affect these conclusions.

To address these questions we perform the global analysis of the ground state observables such as binding energies and charge radii obtained with the state-of-the-art CEDFs which differ substantially in the NMPs. CEDF DD-MEδ, which is coming very close to satisfying all required NMP constraints, is among them.

7.2 Brief outline of the details of theoretical framework

Table 7.1

Input data for fitting protocols of different CEDFs.

CEDF	E	r_{ch}	r_{skin}	Type of nuclei	EOS
1	2	3	4	5	6
NL3*	12	9	4	S	N
DD-ME2	12	9	3	S	N
DD-MEδ	161	86	0	S	Y
DD-PC1	64	0	0	D	Y
PC-PK1	60	17	0	S	N

Table 7.1 list the input data for fitting protocols of different CEDFs. Columns (2-4) show the number of experimental data points on binding energies E, charge radii r_{ch} and neutron skin thicknesses r_{skin} used in the fitting protocols. Column 5 indicates which type of nuclei (spherical (S) or deformed (D)) were used. Column 6 shows whether microscopic equation of state (EOS) has been used in the fit of the functional or not; here "Y" stands for "yes" and "N" for "no". Only DD-MEδ and DD-PC1 functionals are fitted to the equation

of state (EOS) of neutron matter obtained in microscopic calculations with realistic forces. Although these EOS are similar at saturation densities, they differ substantially in their stiffness at the densities typical to the centre of neutron stars [230, 231, 221]. Note that no reliable data, either observational or experimental, exist for such densities. As a result, there is no way to discriminate these predictions for the EOS.

The results have been obtained in the relativistic Hartree-Bogoliubov (RHB) framework the details of which are discussed in chapter II. These deformed RHB calculations are restricted to axial reflection symmetric shapes. We used four CEDFs (NL3* [33], DD-ME2 [26], DD-PC1[27] and DD-MEδ [28]) in the global studies in chapters III and V. We also include CEDF PC-PK1 [79] has been used with success for the studies of the masses of known nuclei by Peking group in Refs. [80, 229].

These functionals reproduce the binding energies of known nuclei at the mean field level with the rms-deviations of around 2.5 MeV (see Table 3.1 in chapter III). However, they differ substantially in the underlying physics (see discussion in Sec. 2 of Ref. [40] and Ref. [79]) and fitting protocols (see Table 7.1).

7.3 The impact of nuclear matter properties of the functionals on the predictions of binding energies of known and neutron-rich nuclei

Although new experimental data on masses of neutron-rich nuclei generated by future rare isotope facilities will allow to improve the isovector properties of the energy density functionals, it is not likely that such an improvement will either eliminate or substantially reduce all possible uncertainties. Moreover, it is not clear whether the bias towards light and medium mass nuclei generated by future experimental data could be avoided since

very little extension of the nuclear chart will be generated for the $Z \geq 82$ nuclei by these experiments (Fig. 7.1). This is precisely the region where most of unknown $Z \leq 120$ nuclei are located and where the distance (in terms of neutrons) between the region of known nuclei and the two-neutron drip line is the largest (see Fig. 3.4 of chapter III).

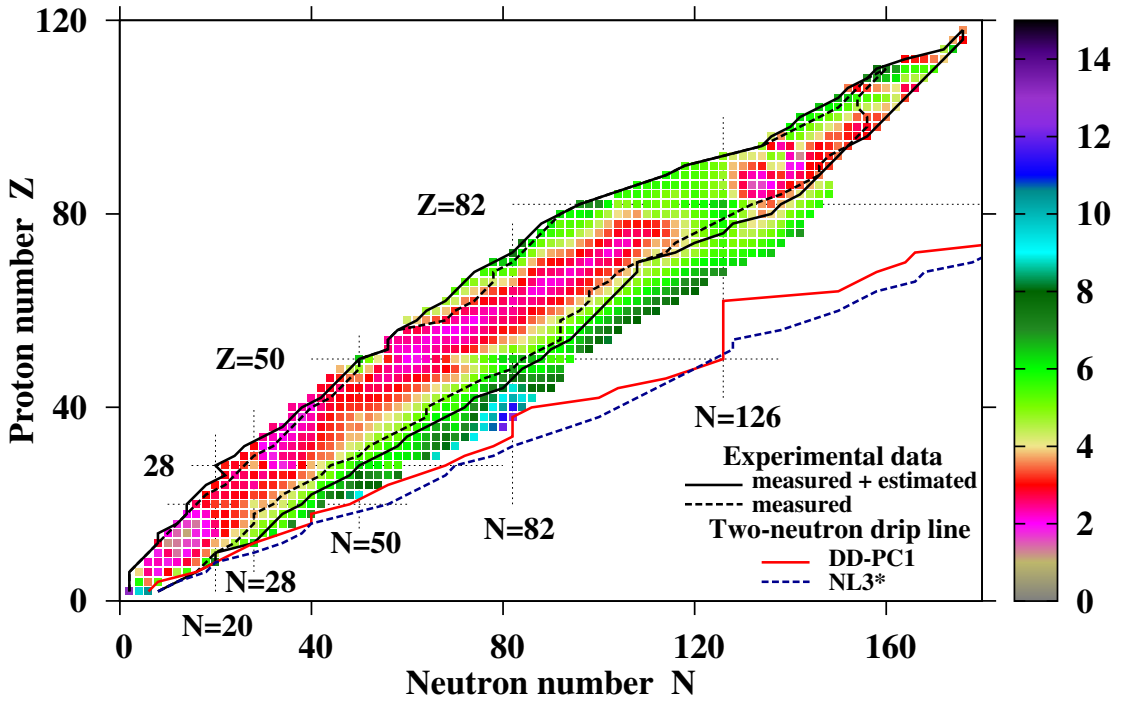

Figure 7.1

The binding energy spread $\Delta E(Z, N)$ as a function of proton and neutron number.

Figure 7.1 show the binding energy spread $\Delta E(Z, N)$ as a function of proton and neutron number. The squares are shown only for the nuclei which are currently known and which will be measured with FRIB. The regions of the nuclei with measured and

measured+estimated masses are enclosed by dashed and solid black lines, respectively. The squares beyond these regions indicate the nuclei which may be measured with FRIB.

The fitting protocols of EDFs always contain data on finite nuclei (typically binding energies, charge radii and occasionally neutron skin thicknesses) and pseudodata on NMP (see Table 7.1). Binding energies and radii show different sensitivity to various terms of the CEDFs and, in addition, there are some important correlations between the NMP and surface properties of the functionals. For example, the calculated binding energies are not very sensitive to the nuclear matter saturation density but are strongly influenced by the choice of the parameters which define the surface energy coefficient a_s in the empirical mass formula [27]. Strong converse relation exists between the nuclear charge radii and the saturation density of symmetric nuclear matter ρ_0 [232]. Also, there is a strong correlation between the slope of symmetry energy L_0 and neutron skins [233, 234, 232] (see Refs. [232, 64, 233, 234, 235] for the discussion of other correlations).

Since available data on binding energies does not allow to fully establish the isovector properties of EDFs and make reliable predictions for masses of neutron-rich nuclei, it is important to have a closer look on NMP in order to see whether strict enforcement of NMP constraints could reduce theoretical uncertainties in isovector properties of EDFs and mass predictions for neutron-rich nuclei.

One way to do that is to see whether there is one-to-one correspondence between the differences in NMP of two functionals and the differences in their description of binding energies. Fig. 7.2 and Table 7.2 are created for such an analysis. The differences of the binding energies of several pairs of CEDFs are compared in Fig. 7.2; they are based on the

results of the RHB calculations obtained in Ref. [40]. Table 7.2 summarizes the NMPs of employed functionals and the experimental/empirical ranges for the quantities of interest obtained in Ref. [1]. The binding energy per particle $E/A \sim -16$ MeV and the saturation density $\rho_0 \sim 0.15$ fm^{-3} represent well established properties of infinite nuclear matter. On the other hand, the incompressibility K_0 of symmetric nuclear matter, its symmetry energy J and the slope L_0 of symmetry energy at saturation density are characterized by substantial uncertainties (see Ref. [1] for details). Effective mass of the nucleon at the Fermi surface m*/m is also poorly defined in experiment.

Table 7.2

Properties of symmetric nuclear matter at saturation.

CEDF	ρ_0 [fm^{-3}]	E/A [MeV]	K_0 [MeV]	J [MeV]	L_0 [MeV]	m*/m
1	2	3	4	5	6	7
NL3* [33]	0.150	-16.31	258	**38.68**	**122.6**	0.67
DD-ME2 [26]	0.152	-16.14	251	32.40	49.4	0.66
DD-MEδ [28]	0.152	-16.12	219	32.35	52.9	0.61
DD-PC1 [27, 79]	0.152	-16.06	230	33.00	68.4	0.66
PC-PK1 [79]	0.154	-16.12	238	**35.6**	**113**	0.65
SET2a	~ 0.15	~ -16	190-270	25-35	25-115	
SET2b	~ 0.15	~ -16	190-270	30-35	30-80	

Table 7.2 list the density ρ_0, the energy per particle E/A, the incompressibility K_0, the symmetry energy J and its slope L_0, and the Lorentz effective mass m*/m [2] of a nucleon at the Fermi surface. Top five lines show the values for indicated covariant energy density functionals, while bottom two lines show two sets (SET2a and SET2b) of the constraints on the experimental/empirical ranges for the quantities of interest defined in Ref. [1]. The

CEDF values which are located beyond the limits of the SET2b constraint set are shown in bold.

The smallest difference in the predictions of binding energies exists for the DD-ME2/DD-MEδ pair of the functionals (Fig. 7.2a); for almost half of the $Z \leq 104$ nuclear landscape their predictions differ by less than 1.5 MeV and only in a few points of nuclear landscape the differences in binding energies of two functionals are close to 5 MeV. The NMPs of these two functionals are similar with some minor differences existing only for the incompressibility K_0 and Lorentz effective mass m*/m (Table 7.2). However, the similarity of NMP does not necessarily lead to similar predictions of binding energies. This is illustrated in Fig. 7.2d on the example of the pair of the DD-ME2 and DD-PC1 functionals for which substantial differences in the predictions exist for quite similar NMP (Table 7.2).

A more striking example is seen in Fig. 7.2b where the NL3*/DD-PC1 pair of the functionals, which are characterized by a substantial differences in the energy per particle (E/A), symmetry energy J and its slope L_0 (Table 7.2), have significantly smaller differences in predicted binding energies as compared with above mentioned DD-ME2/DD-PC1 pair of the functionals. This is a consequence of a peculiar feature of the relative behavior of the binding energies of the NL3* and DD-PC1 functionals with increasing isospin. It should be noted that the J and L_0 values of the NL3* functional are located outside the experimental/empirical ranges for these values defined in Ref. [1] (see Table 7.2).

Although FSUGold and DD-MEδ satisfy the majority of the NMP constraints, they still face significant problems in the description of finite nuclei. FSUGold is designed for neutron star applications in Ref. [76] and it is characterized by the largest rms deviations

(6.5 MeV) from experiment for binding energies among all CEDF's the global performance of which is known [40]. DD-MEδ which is the most microscopic functional among all existing CEDF's, provides quite reasonable description of binding energies (see Table 3.1 of chapter III and Refs. [40, 188]), it generates unrealistically low inner fission barriers in superheavy elements [236] and fails to reproduce octupole deformed nuclei in actinides [195].

From the analysis in chapters III and V it is clearly seen that the CEDFs NL3*, DD-ME2, PC-PK1 and DD-PC1 represent better and well-rounded functionals as compared with FSUGold and DD-MEδ. They are able to describe not only ground state properties but also the properties of excited states [33, 53, 54, 170, 237, 172, 171, 26, 27]. This is despite the fact that the first three functionals definitely fail to describe some of the nuclear matter properties (see Table 7.2 and Ref. [1]). It is not clear whether that is also the case for DD-PC1 since it was not analyzed in Ref. [1]. Therefore, one can conclude that functionals which provide good NMPs, do not necessarily well describe finite nuclei.

As a result one can say that the NMP constraints do not allow to eliminate some of the CEDFs from the consideration and in this way to decrease the uncertainties in the predictions of binding energies of the neutron-rich nuclei and the position of two-neutron drip line.

7.4 Concluding remarks

The question of how strictly nuclear matter constraints have to be imposed and which values have to be used for the definition of covariant energy density functionals still re-

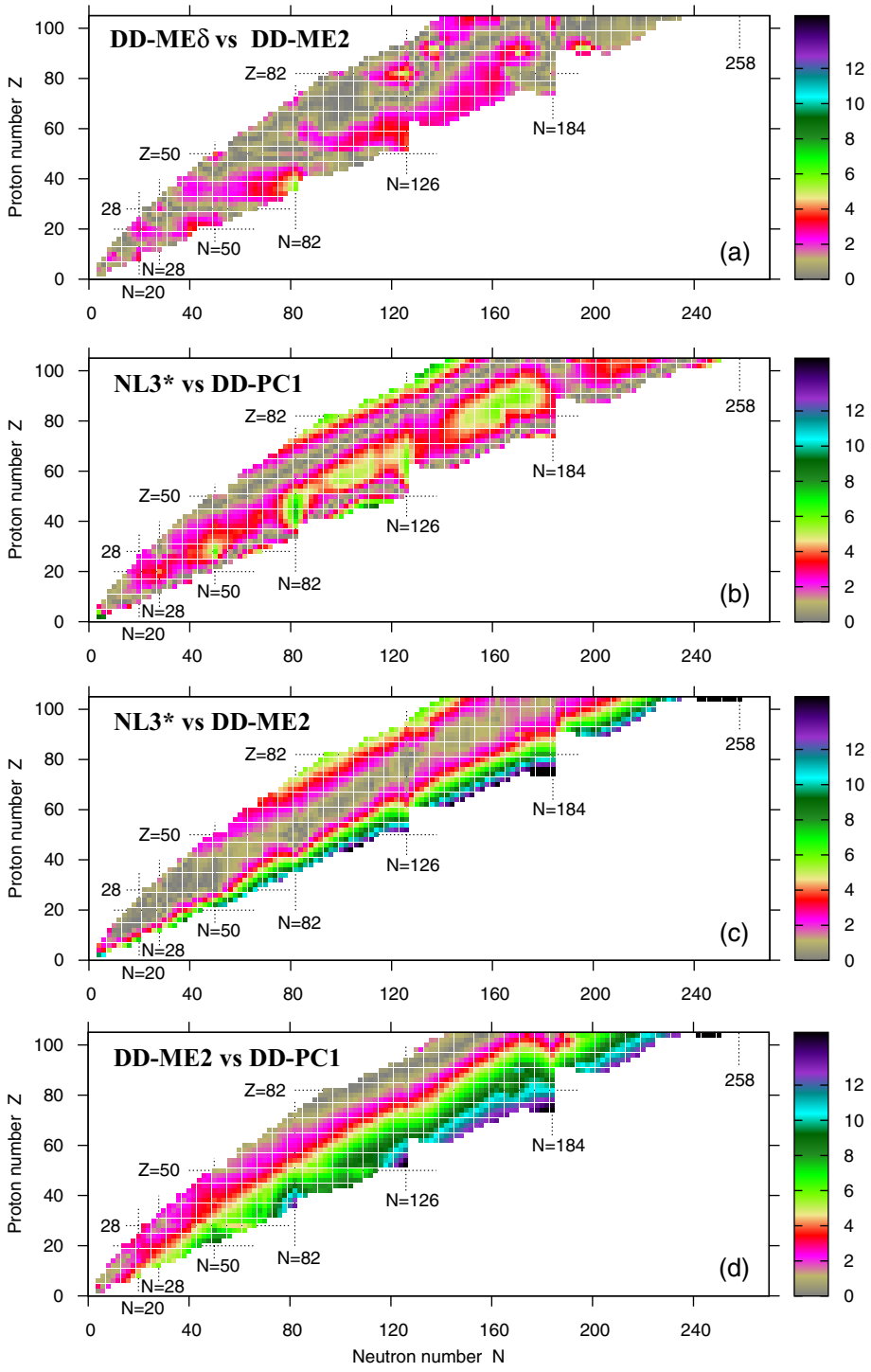

Figure 7.2

Binding energy spreads $\Delta E(Z, N)$ for the pairs of indicated functionals.

mains not fully answered. Definitely, the equation of state relating pressure, energy density, and temperature at a given particle number density is essential for modeling neutron stars, core-collapse supernovae, mergers of neutron stars and the processes (such as nucleosynthesis) taking places in these environments. However, there are substantial experimental/empirical/model uncertainties in the definition of the NMP constraints.

In addition, the properties of finite nuclei are defined by the underlying shell structure which depends sensitively on the single-particle features [144, 29, 188]. As a consequence, we are facing the situation in which the functionals which are coming close to satisfying all NMP constraints perform quite poorly in the description of finite nuclei. This was exemplified by the FSUGold and DD-MEδ functionals. The former provides the worst rms-deviations in global description of binding energies [75, 40], while the latter fails to reproduce octupole deformed actinides [188] and predicts too low fission barriers in superheavy nuclei [236] so that their existence could be questioned. On the other hand, the functionals which fail to reproduce the NMP constraints suggested in Ref. [1] such as NL3* and PC-PK1 are able to reproduce reasonably well the ground state properties of finite nuclei.

CHAPTER VIII

HYPERHEAVY NUCLEI: EXISTENCE AND STABILITY

8.1 Introduction

The investigation of superheavy elements (SHE) remains one of the most important sub-fields of low-energy nuclear physics [10]. The element Og with proton number $Z = 118$ is the highest Z element observed so far [32]. Although future observation of the elements in the vicinity of $Z \sim 120$ seems to be feasible, this is not a case for the elements with Z beyond 122. Considering also that the highest in Z spherical shell closure in SHE is predicted at $Z = 126$ in Skyrme density functional theory (DFT) [207], it is logical to name the nuclei with $Z > 126$ as hyperheavy [238, 212]. The properties of such nuclei are governed by increased Coulomb repulsion and single-particle level density; these factors reduce the localization of shell effects in particle number [212].

Although hyperheavy nuclei have been studied both within DFTs [238, 212, 239, 208, 240, 241] and phenomenological [242, 243, 244] approaches, the majority of these studies have been performed only for spherical shapes of the nuclei. This is a severe limitation which leads to misinterpretation of physical situation in many cases since there is no guarantee that spherical minimum in potential energy surface exist even in the nuclei with relative large spherical shell gaps (see discussion in Ref. [188]). In addition, the stability of hyperheavy nuclei against spontaneous fission could not be established in the calculations

restricted to spherical shape. The effects of axial and triaxial deformations in hyperheavy nuclei are considered only in Refs. [239, 245] and in Ref. [240, 246], respectively. However, only few nuclei are studied in Refs. [239, 245, 246] and according to the present study the deformation range employed in Ref. [240] is not sufficient for $Z \geq 130$ nuclei.

The investigation of hyperheavy nuclei is also intimately connected with the establishments of the limits of both the nuclear landscape and periodic table of elements. The limits of nuclear landscape at the proton and neutron drip lines and related theoretical uncertainties have been extensively investigated in a number of theoretical frameworks but only for the $Z < 120$ nuclei [5, 84, 40]. The atomic relativistic Hartree-Fock [247] and relativistic Multi-Configuration Dirac-Fock [248, 249] calculations indicate that the periodic table of elements terminates at $Z = 172$ and $Z = 173$, respectively. However, at present it is not even clear whether such nuclei are stable against fission. In addition, Refs. [247, 248, 249] employ phenomenological expression for charge radii and its validity for the $Z \sim 172$ nuclei is not clear.

To address these deficiencies in our understanding of hyperheavy nuclei the systematic investigation of even-even nuclei from $Z = 122$ up to $Z = 180$ is performed within the axial relativistic Hartree-Bogoliubov (RHB) framework employing the DD-PC1 covariant energy density functional [27]. This functional provides good description of the ground state and fission properties of known even-even nuclei [40, 250]. To establish the stability of nuclei with respect to triaxial distortions a number of nuclei have been studied within the triaxial RHB [236] and relativistic mean field + BCS (RMF+BCS) [170] frameworks. The main goals of this study are (i) to understand whether the nuclei stable against fission

could be present in the $Z \geq 126$ region and (ii) to define the most important features of such nuclei.

8.2 Axial calculations: general structure of potential energy surfaces.

Majority of the calculations presented in this chapter employ the DD-PC1 functional which is considered to be the best relativistic functional today based on systematic and global studies of different physical observables (see chapter III) and Refs. ([188, 40, 236, 251, 171, 195]). Other functionals are used to assess the systematic theoretical uncertainties in the predictions of the heights of fission barriers around spherical minima.

The truncation of the basis is performed in such a way that all states belonging to the major shells up to N_F fermionic shells for the Dirac spinors (and up to $N_B = 20$ bosonic shells for the meson fields in meson exchange functionals) are taken into account. The comparison of the axial RHB calculations with $N_F = 20$ and $N_F = 30$ shows that in ^{208}Pb the truncation of basis at $N_F = 20$ provides sufficient accuracy for all deformations of interest. However, in hyperheavy nuclei the required size of the basis depends both on the nucleus and deformation range of interest. The $N_F = 20$ basis is sufficient for the description of deformation energy curves in the region of $-1.8 < \beta_2 < 1.8$. The deformation ranges $-3.0 < \beta_2 < -1.8$ and $1.8 < \beta_2 < 3.0$ typically require $N_F = 24$ (low-Z and low-N hyperheavy nuclei) or $N_F = 26$ (high-Z and high-N hyperheavy nuclei). Even more deformed ground states with $\beta_2 \sim -4.0$ are seen in high-Z/high-N hyperheavy nuclei (see Figs. 8.1c and d for the $^{466}156$ and $^{426}176$ results); their description

requires $N_F = 30$. Thus, the truncation of basis is made dependent on the nucleus and typical profile of deformation energy curves or potential energy surfaces.

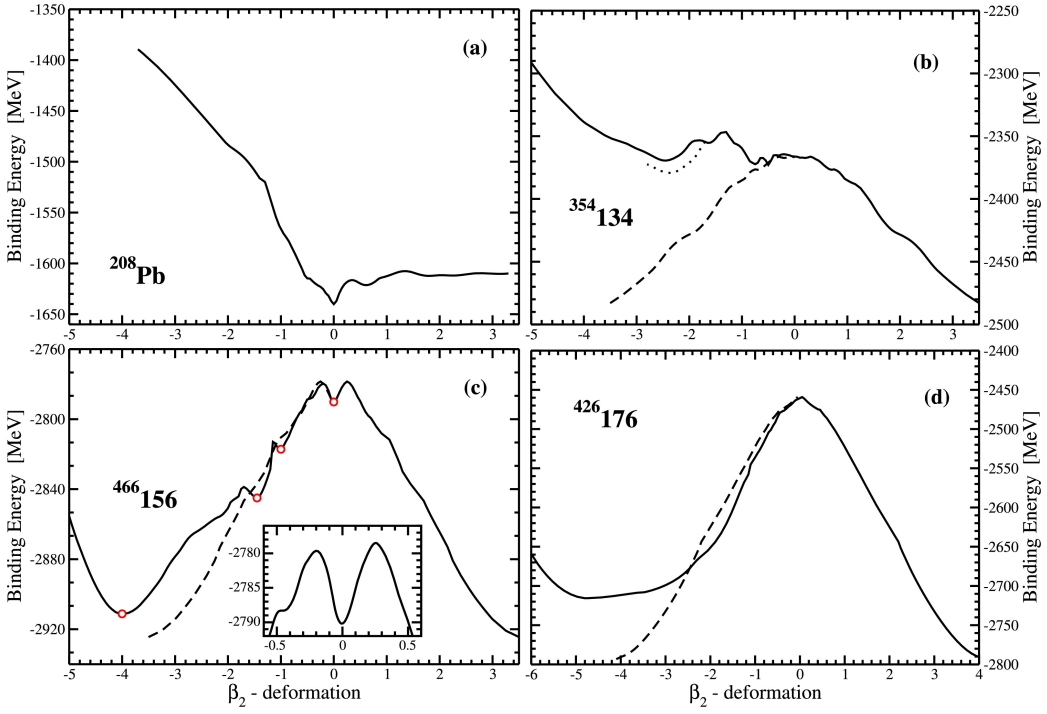

Figure 8.1

Deformation energy curves of ^{208}Pb and selected even-even hyperheavy nuclei.

Fig. 8.1 is the deformation energy curves of ^{208}Pb and selected even-even hyperheavy nuclei obtained in axial RHB calculations with DD-PC1 functional and the $N_F = 30$ basis. The insert in panel (c) shows the fission barriers around spherical state in details. Open circles in panel (c) indicate the deformations at which the density distributions are plotted in Fig. 8.4 below. Dashed lines show mirror reflection of the $\beta_2 > 0$ part of deformation energy curve onto negative β_2 values.

The deformation parameters β_2 and γ are extracted from respective quadrupole moments: Q_{20} (see Eq. 3.4) and

$$Q_{22} = \int d^3r\rho(r)\,(x^2 - y^2), \tag{8.1}$$

via

$$\beta_2 = \sqrt{\frac{5}{16\pi}}\frac{4\pi}{3AR_0^2}\sqrt{Q_{20}^2 + 2Q_{22}^2} \tag{8.2}$$

$$\gamma = \arctan\sqrt{2}\frac{Q_{22}}{Q_{20}} \tag{8.3}$$

where $R_0 = 1.2A^{1/3}$. Note that $Q_{22} = 0$ and $\gamma = 0$ in axially symmetric RHB calculations. The β_2 and γ values have a standard meaning of the deformations of the ellipsoid-like density distributions only for $|\beta_2| < 1.0$ values. At higher $|\beta_2|$ values they should be treated as dimensionless and particle normalized measures of the Q_{20} and Q_{22} moments. This is because of the presence of toroidal shapes at large negative β_2 values and of necking degree of freedom at large positive β_2 values. Note that physical observables are frequently shown as a function of the Q_{20} and Q_{22} moments. However, from our point of view such way of presentation has a disadvantage that the physical observables of different nuclei related to the shape of the density distributions (such as deformations) are difficult to compare because the Q_{20} and Q_{22} moments depend on particle number(s).

For each nucleus under study, the deformation energy curves in the $-5.0 < \beta_2 < 3.0$ range are calculated in the axial reflection symmetric RHB framework [40]; such large range is needed for a reliable definition of the β_2 value of the lowest in energy minimum for axial symmetry (LEMAS). This LEMAS becomes the ground state if the higher order

deformations (triaxial, octupole) do not lead to the instability of these minima. The nuclei up to $Z = 138$ are calculated using the basis with N_F up to 26.

On the contrary, with the exception of the $^{466}156$ and $^{426}176$ nuclei, the $Z = 140 - 180$ nuclei are calculated only with $N_F = 20$. The major goals of the calculations for the $Z = 140 - 180$ nuclei are (i) to define the type of the LEMAS states, (ii) to find whether spherical or normal deformed states could be the LEMAS states of these nuclei and (iii) to calculate the fission barriers around spherical states.

The required size of the basis limits the applicability of triaxial calculations to typically $|\beta_2| < 2$ range. The nuclei with the ground states located at the deformations below $\beta_2 \sim 1.0$ are calculated in triaxial RHB framework [236], while a pair of nuclei with local minima at $\beta \sim 2.4, \gamma \sim 60^\circ$ corresponding to toroidal shapes were calculated in triaxial RMF+BCS framework [170]. The later framework is more numerically stable at very large β_2 values. Because of high computational cost of the calculations with triaxiality included, only limited number of nuclei were studied in these frameworks. The role of octupole deformation in the nuclei shown in Fig. 8.8 has been studied in the axial reflection asymmetric RHB code of Ref. [195]. These calculations are performed with $N_F = 20$

Fig. 8.1 illustrates the dependence of the deformation energy curves, obtained in axial RHB calculations, on the nucleus. The $Z = 82$ ^{208}Pb nucleus is spherical in the ground state. The total energy of the nucleus is increasing rapidly with increasing oblate deformation. On the prolate side, it increases with the increase of quadrupole deformation up to $\beta_2 \sim 1.4$ and then stays more or less constant. This leads to the existence of high (~ 30

MeV) and very broad fission barrier which is responsible for the stable character of this nucleus.

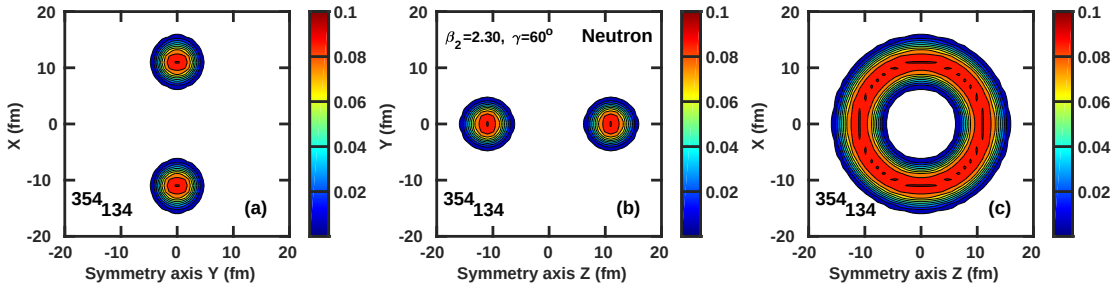

Figure 8.2

Neutron density distributions at the local minimum with $\beta_2 = 2.30, \beta_4 = +1.5, \gamma = 60^\circ$ in the ^{354}134 nucleus.

The ^{354}134 nucleus shows completely different profile of the deformation energy curves (Fig. 8.1b). The LEMAS is located at $\beta_2 \sim -0.5$ and the deformation energy curves on the oblate side are more flat in energy as compared with ^{208}Pb. The fission barrier for the $\beta_2 \sim -0.5$ minimum is rather high ($\sim$ 8.5 MeV) and broad (Fig. 8.1b) which would suggest high stability of this nucleus against fission if the nucleus would stay axially symmetric. Note that at $\beta_2 < -1.5$ values there are two solutions; the one shown by solid line has $\beta_4 \sim +0.67\beta_2$ and another (which appear only in triaxial calculations at $\gamma = 60^\circ$) shown by dotted line has $\beta_4 \sim -1.7\beta_2$. The minima of these two solutions appear at $\beta_2 \sim -2.4$. The former solution is characterized by toroidal shapes (see Fig. 8.2 which is the neutron density distributions at the local minimum with $\beta_2 = 2.30, \beta_4 = +1.5, \gamma = 60^\circ$ in the ^{354}134 nucleus obtained in triaxial RMF+BCS calculations. To give

a full three-dimensional representation of the density distributions, they are plotted in the xy, yz and xz planes at the positions of the Gauss-Hermite integration points in the z, x and y directions closest to zero, respectively. The density colormap starts at $\rho_n = 0.005$ fm^{-3} and shows the densities in fm^{-3}.), while the latter one by double banana shapes connected by low density links (see Fig. 8.3, same as Fig. 8.2 but for the local minimum with $\beta_2 = 2.50, \beta_4 = -4.4, \gamma = 60°$. For better visualization the density colormap starts at $\rho_n = 0.0002$ fm^{-3}.). The $\beta_4 \sim -1.7\beta_2$ solution is lower in energy in a number of nuclei around the $^{354}134$ nucleus but it is unstable with respect to triaxial distortions (see discussion below). Thus, in considering the shapes with $\beta_2 < -1.5$ we focus on toroidal shapes with positive β_4 which are potentially stable with respect to triaxial distortions. In the $^{354}134$ nucleus, the minimum of this solution with $\beta_2 \sim -2.5$ is located at 4.2 MeV excitation energy with respect to the $\beta_2 \sim -0.5$ minimum.

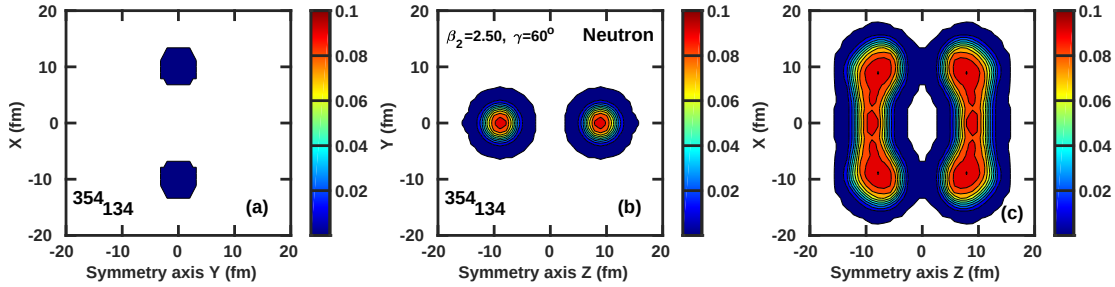

Figure 8.3

The same as Fig. 8.2 but for the local minimum with $\beta_2 = 2.50, \beta_4 = -4.4, \gamma = 60°$.

Further increase of proton number leads to drastic modifications of the deformation energy curves. In the $^{466}156$ and $^{426}176$ nuclei, the minimum appears at extreme $\beta_2 \sim -4.0$

values. However, these minima are potentially unstable with respect to the transition to the prolate shape via γ-plane and subsequent fission since prolate shapes with corresponding quadrupole deformations are located at lower energies (compare dashed lines with solid ones in Figs. 8.1c and d). Note also that in the $^{466}156$ nucleus there are excited local $\beta_2 \sim -1.2$ and spherical minima which could be potentially stable against fission.

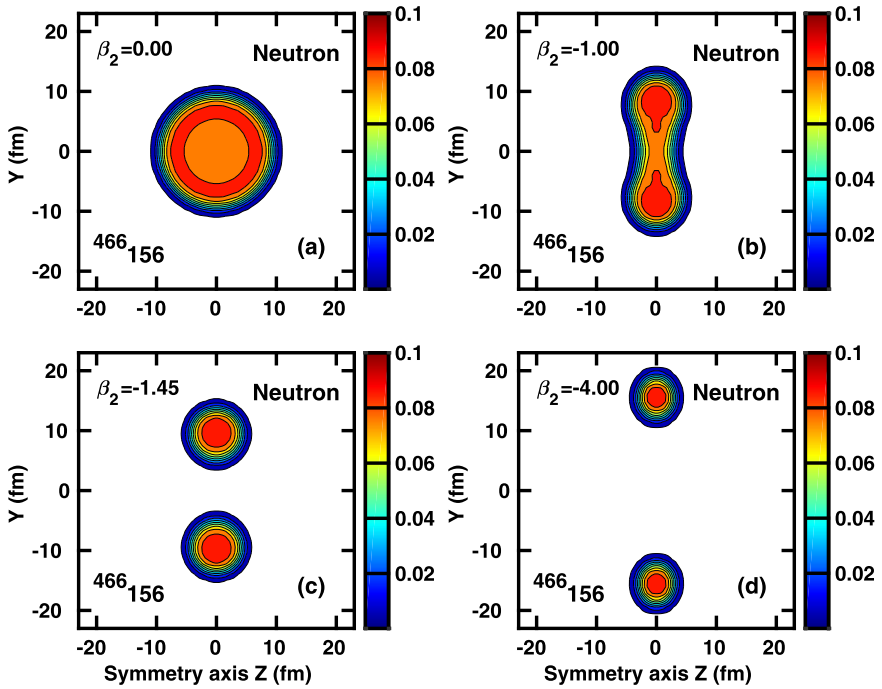

Figure 8.4

Neutron density distributions of the $^{466}156$ nucleus.

The evolution of the neutron density distributions with the change of the β_2 values indicated in Fig. 8.1c are shown for the $^{466}156$ nucleus in Fig. 8.4. They are plotted in the yz plane at the position of the Gauss-Hermite integration points in the x directions

closest to zero. The density colormap starts at $\rho_n = 0.005$ fm^{-3} and shows the densities in fm^{-3}. The nucleus at spherical shape is characterized by the density depression in the central part of the nucleus; the maximum neutron density $\rho = 0.0896$ fm^{-3} is achieved at radial coordinate $r = 6.55$ fm while the density in the center is only $\rho = 0.076$ fm^{-3}. This depression is similar (but less pronounced) to the one predicted for the $^{292}120$ superheavy nucleus in Refs. [207, 252]. Our calculations show neither bubble nor semi-bubble shapes (in the language of Ref. [238]) for the lowest in energy solutions of spherical nuclei shown in Fig. 8.8 below. Note that proton density is roughly half of the neutron one and central density depression is somewhat more pronounced in proton subsystem as compared with neutron one. As illustrated in Fig. 8.4b, biconcave disk density distribution is formed at large oblate deformation of $\beta_2 = -1.0$. Further decrease of the β_2 values leads to the formation of toroidal shapes (Figs. 8.4c and d). It is observed that with the increase of absolute value of β_2 the radius of the toroid increases and the tube radius decreases.

The biconcave disk and toroidal shapes in atomic nuclei have been investigated in a number of the papers [245, 246, 253, 254, 255, 256]. However, in absolute majority of the cases such shapes correspond to highly excited states either at spin zero [246, 255] or at extreme values of angular momentum [253, 254, 257]. The latter substantially exceed the values of angular momentum presently achievable at the state-of-art experimental facilities [258]. The competition of such shapes at spin zero in superheavy even-even $Z = 120$ isotopes with $N = 166 - 190$ and in the even-even $N = 184$ isotones with $Z = 106 - 124$ has been investigated in constrained Skyrme-HFB calculations in Ref. [255]. It was concluded that investigated nuclei in toroidal shapes are unstable against returning to the

shape of sphere-like geometry (Ref. [255]). Similar study for superheavy $^{316}122$, $^{340}130$, $^{352}134$ and $^{364}138$ nuclei has been performed in Skyrme Hartree-Fock calculations of Ref. [246]; only in $^{364}138$ nuclei the toroidal solution is the lowest in energy. The Gogny HFB calculations of Ref. [245] showed that toroidal shapes represent the lowest in energy solutions at axial shape in the $^{416}164$ and $^{476}184$ nuclei.

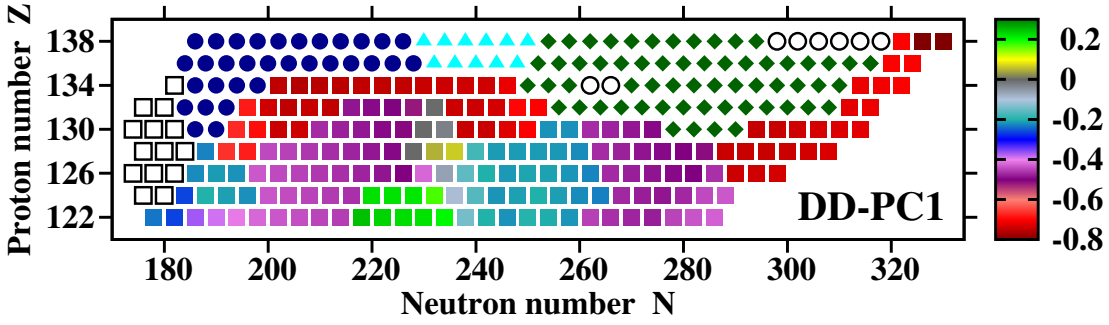

Figure 8.5

Charge quadrupole deformations β_2 of the lowest in energy particle bound minima obtained in axial RHB calculations.

Fig. 8.5 presents the systematics of the β_2 values for the lowest in energy minima for axial symmetry obtained in axial RHB calculations for $Z = 122 - 138$ nuclei. The calculations are performed for each second even-even nucleus in the isotopic chain starting at approximately two-proton drip line and ending at approximately two-neutron drip line. The nuclei with quadrupole deformations of $-0.8 < \beta_2 < 0.3$ are shown by squares; colormap provides detailed information on their deformations. The nuclei with toroidal shapes in the lowest in energy minima are shown by open black squares ($-2.0 < \beta_2 < -1.5$), solid dark blue circles ($-2.5 < \beta_2 < -2.0$), solid cyan triangles ($-3.0 < \beta_2 <$

-2.5), solid dark green diamonds ($-3.5 < \beta_2 < -3.0$) and open black circles ($\beta_2 < -3.5$).

Only few spherical nuclei located around $Z \sim 130, N \sim 230$ are found in the calculations. Prolate deformed nuclei are seen only at $Z = 122, 124$ and $N = 218 - 236$. The rest of the nuclear chart is dominated by oblate or toroidal shapes in the LEMAS. The β_2 values of these states depend on the combination of proton and neutron numbers. However, the general trend is that they increase with proton number. The calculations for nuclei beyond $Z = 138$ are extremely time-consuming due to required increase of the fermionic basis up to $N_F = 30$. The scan of the deformation energy curves in axial RHB calculations with $N_F = 20$ for the $Z = 140 - 180$ nuclei located between two-proton and two-neutron drip lines does not show the presence of either prolate or spherical LEMAS states; the LEMAS states in all $Z = 140 - 180$ nuclei have toroidal shapes with $\beta_2 < -1.4$. However, because of the limited size of the basis these values have to be considered as lower limits (in absolute sense). Thus, for the first time, our systematic calculations show that toroidal shapes should represent the lowest in energy minima of almost all hyperheavy $Z > 134$ (and some nuclei with lower Z, see Fig. 8.5) if axially symmetric solutions are stable with respect of triaxial distortions.

8.3 Triaxial calculations: the drop of stability via triaxial plane.

However, it is well known that triaxial deformation lowers the fission barriers in actinides and superheavy nuclei with $Z \leq 120$ and $N \leq 184$ [170, 259, 260, 179, 70, 261]. These nuclei are either prolate or spherical in their ground states and thus the impact of

triaxiality is limited: for example, the lowering of inner fission barriers in actinides due to triaxiality is typically on the level of 1-3 MeV. On the contrary, the impact of triaxiality on fission barriers gets much more pronounced in the nuclei with ground state oblate shapes and it generally increases with the rise of their oblate deformation. Not only the fission through the γ-plane gets more energetically favored, but also the fission path through γ-plane becomes much shorter than the one through the $\gamma = 0^\circ$ axis.

These features are illustrated in Fig. 8.6. The energy difference between two neighboring equipotential lines is equal to 0.5 MeV. The red lines show static fission paths from respective minima. Open white circles show the global (and local) minimum(a). Black crosses indicate the saddle points on these fission paths. The colormap shows the excitation energies (in MeV) with respect to the energy of the deformation point with largest binding energy.

The $^{360}130$ nucleus is an example of the coexistence of spherical ground state and excited (at 0.8 MeV) oblate (with $\beta_2 \sim -0.5$) minimum. The static fission paths from these minima are comparable in length and both of them have reduced (by ~ 2 MeV) inner fission barriers as compared with axial RHB calculations (see Table 8.1). The effect of the reduction of inner fission barrier due to triaxiality becomes much more pronounced in the $^{432}134$ nucleus. As compared with axial calculations, the presence of triaxiality leads to the shift of minimum from ($\beta_2 \sim 0.74, \gamma = 60^\circ$) to ($\beta_2 \sim 0.82, \gamma \sim 37^\circ$) and the reduction of the fission barrier height from 8.16 MeV to 1.30 MeV. The $^{340}122$ nucleus is an example of the coexistence of the ground state oblate $\beta_2 = -0.46$ and slightly excited (by 0.72 MeV) prolate $\beta_2 = 0.25$ minima in axial RHB calculations which have fission

barriers at 5.74 and 3.19 MeV, respectively (see Table 8.1). The triaxiality leads to the γ-softness of potential energy surfaces so that these minima drift in the γ-plane by $10-15^{\circ}$. However, it also leads to substantial reduction of fission barrier heights down to ~ 2 MeV (see Table 8.1). In axial RHB calculations, the $^{392}134$ nucleus has superdeformed oblate ground state with $\beta_2 = -0.79$ and highly excited (at excitation energy of 2.69 MeV) oblate state with $\beta_2 = -0.23$. The fission barriers for these two minima are 10.24 and 7.55 MeV, respectively. The triaxiality substantially affects the position of first minimum so it drifts to $\beta_2 = 0.88, \gamma = 39^{\circ}$ but has almost no effect on the second minimum. However, it has huge impact on the heights of their fission barriers which are reduced to 0.56 and 2.08 MeV, respectively (see Table 8.1).

Table 8.1 summarizes the results of more systematic triaxial RHB calculations. The columns $3-5$ show the results of the axial RHB calculations. Here β_{min}, β_{saddle} and E^B_{ax} are the equilibrium quadrupole deformation of the global (local) minimum, the quadrupole deformation and the energy of the saddle along respective fission path. The excited minima are indicated by asterisks (*). Their excitation energies are shown in brackets in column 3. The results of the triaxial RHB calculations are provided in the columns $6-8$. Note that the allowance of triaxial deformation could shift the position of the local minimum in the deformation plane and in absolute majority of the cases shifts the positions of the saddle points. Thus, $(\beta,\gamma)_{min}$, $(\beta,\gamma)_{saddle}$ and E^B_{triax} show the deformations of the minima, the deformations of saddle points and their energies obtained in triaxial RHB calculations. The word 'no' is used in respective columns in the case when the minimum and fission paths existing in axial RHB calculations disappear in triaxial RHB calculations.

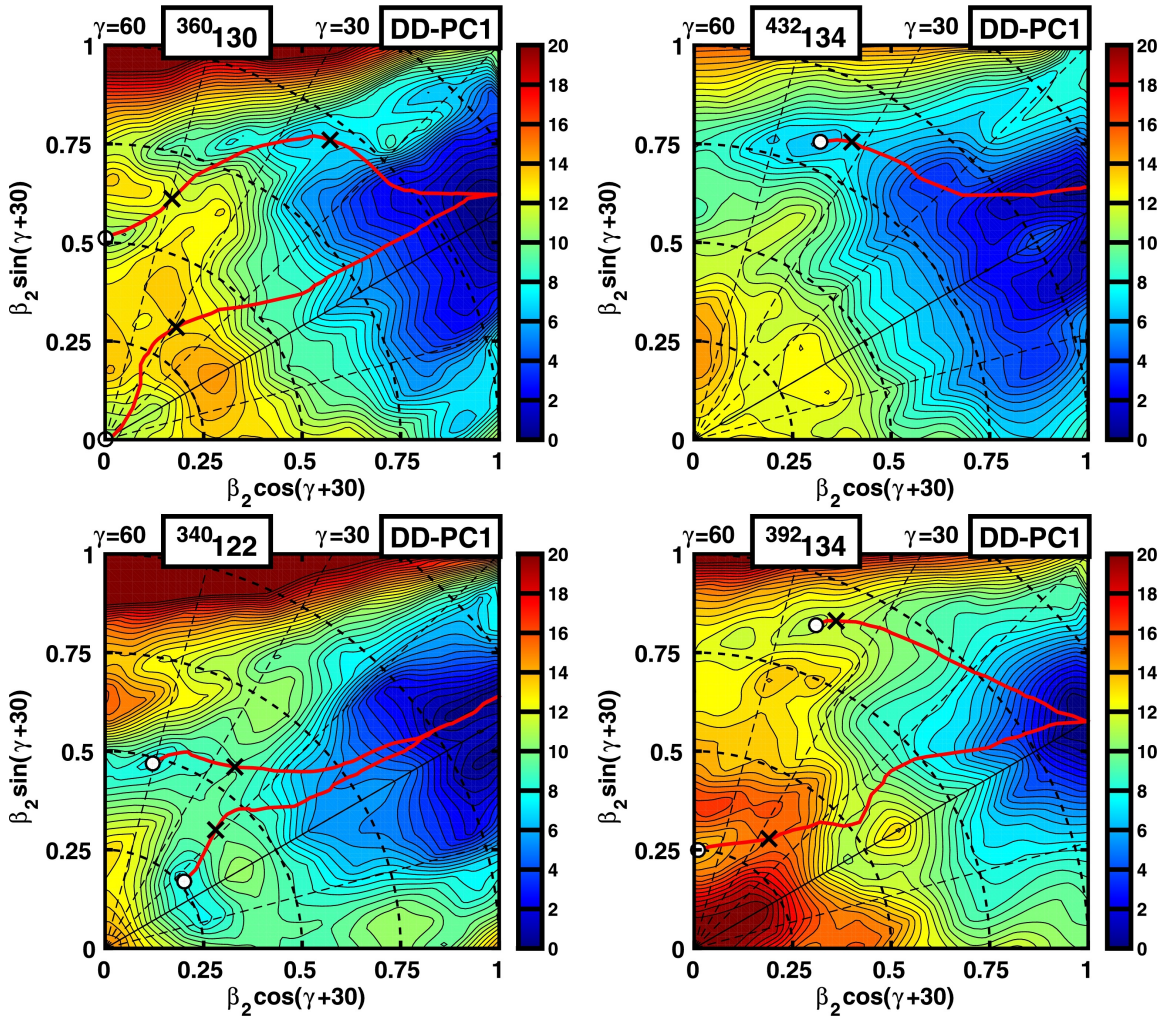

Figure 8.6

Potential energy surfaces (PES) of indicated nuclei obtained in the RHB calculations.

Table 8.1

The heights of the fission barriers along the fission paths from different minima obtained in axial and triaxial RHB calculations.

		Axial RHB			Triaxial RHB		
Z	N	β_{min}	β_{saddle}	E^B_{ax}	$(\beta,\gamma)_{min}$	$(\beta,\gamma)_{saddle}$	E^B_{triax}
1	2	3	4	5	6	7	8
122	182	-0.25	0.20	5.99	0.23,58	0.43,35	3.10
	202	-0.43	0.04	8.18	0.43,56	0.44,46	1.59
	218	-0.46	0.00	5.74	0.49,46	0.57,24	1.75
		0.25* [0.72]	0.39	3.19	0.26,10	0.41,17	2.05
	222	0.24	0.37	4.26	0.25,0	0.39,25	2.62
		-0.48* [2.12]	-0.25	3.79	0.45,60	0.47,36	1.15
	242	-0.19	0.31	4.05	0.18,57	0.48,31	3.07
	262	-0.23*	0.13	5.38	0.25,58	0.33,22	1.07
		-0.45 [0.18]	0.13	5.56	0.45,51	0.47,40	1.09
	282	0.34	0.46	1.84	0.34,0	0.41,24	1.68
		-0.44* [1.64]	0.00	8.11	0.46,38	0.52,29	0.65
126	214	-0.46	0.00	8.29	0.48,47	0.52,37	2.05
	234	-0.05	0.33	3.85	0.15,2	0.31,20	3.04
		-0.39* [1.34]	0.33	2.51	0.40,59	0.40,30	2.09
	254	-0.21	0.22	6.16	0.23,58	0.34,23	2.91
	274	-0.49	-0.02	8.95	0.48,59	0.47,53	1.86
	294	-0.43	0.00	6.17	0.43,56	0.46,44	0.52
		-0.74	0.00	6.18	no	no	no
130	206	-0.74	0.00	8.99	0.82,37	0.84,31)	0.68
		-0.46* [0.19]	0.00	8.80	no	no	no
	226	-0.50	-0.25	5.22	0.50,58	0.56,33	3.02
		0.12* [1.69]	0.33	3.44	0.15,2	0.35,27	1.21
		-0.74* [2.19]	-0.64	3.38	0.82,37	0.83,34	0.70
	230	-0.01	0.32	4.86	0.00,0	0.34,26	2.77
		-0.53* [0.81]	0.32	4.05	0.52,55	0.63,44	2.04
	246	-0.72	0.25	6.68	0.73,59	0.75,50	0.67
		-0.21* [0.28]	0.25	6.40	0.26,58	0.47,35	3.12
	266	-0.47	0.01	9.05	0.48,59	0.48,54	0.56
		-0.78* [0.74]	0.01	8.31	no	no	no
		-0.23* [1.57]	0.01	7.48	0.28,33	0.34,20	0.58
	286	-0.75	0.00	8.19	0.77,40	0.75,35	1.28
		-0.51* [0.27]	0.00	7.92	0.54,51	0.57,38	1.35
134	258	-0.79	0.00	10.24	0.88,39	0.90,37	0.56
		-0.23* [2.69]	0.00	7.55	0.25,58	0.33,25	2.08

Table 8.1

(continued)

		Axial RHB			Triaxial RHB		
Z	N	β_{min}	β_{saddle}	E^B_{ax}	$(\beta,\gamma)_{min}$	$(\beta,\gamma)_{saddle}$	E^B_{triax}
1	2	3	4	5	6	7	8
134	278	-0.50	0.07	10.68	0.51,56	0.52,49	1.54
		-0.79* [0.17]	0.07	10.51	0.79,38	0.79,33	2.56
	298	-0.74	-0.21	8.16	0.82,37	0.85,32	1.30
	318	-0.71	0.28	11.59	0.71,59	0.78,47	1.37

The general conclusion is that the barriers along the fission paths emerging from the oblate minima located within the $-1.0 < \beta_2 \leq 0.0$ range decrease with increasing proton number. As a result, the majority of these nuclei would be unstable with respect to fission. Similar trend of the evolution of fission barriers with proton number has also been seen in microscopic+macroscopic (mic+mac) calculations with Woods-Saxon potential and Skyrme DFT calculations with the SLy4 functional presented in Ref. [240]. Note that these calculations use smaller deformation plane (ranging from $\beta_2 = -0.85$ up to $\beta_2 = 0.45$) as compared with the one shown in Fig. 8.6 . The Skyrme DFT calculations provide higher fission barriers as compared with mic+mac and our RHB results. However, the SLy4 functional substantially overestimates fission barriers in actinides and SHE [240].

The situation however is substantially complicated by the fact that with increasing proton number toroidal shapes correspond to the lowest in energy solutions in axial RHB calculations (Fig. 8.5). Their large β_2 values and high Z and N values require increased basis which makes triaxial RHB and RMF+BCS calculations prohibitively time consuming. A priori we cannot exclude the stability of such shapes against fission or multifragmentation.

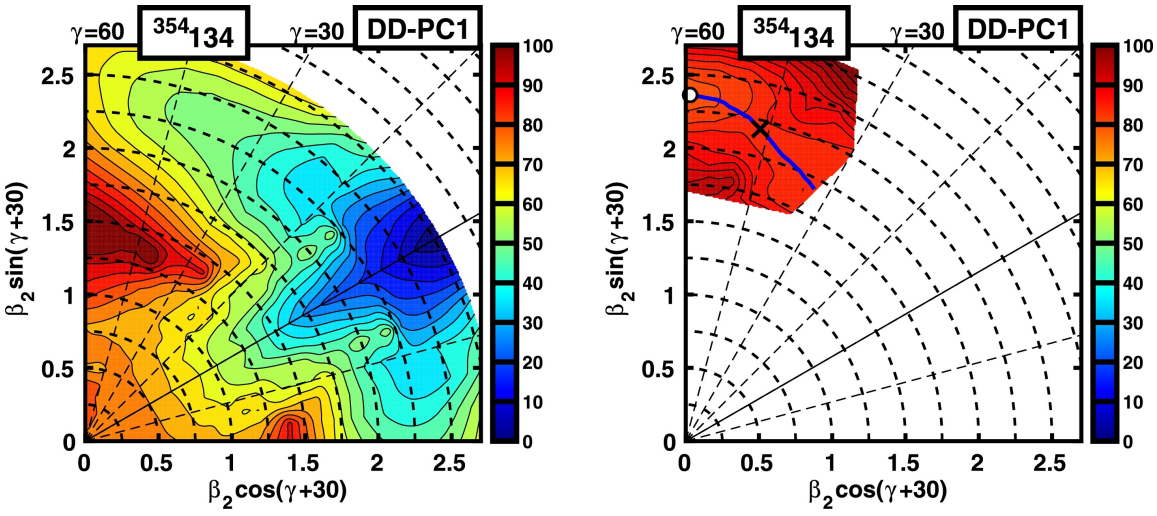

Figure 8.7

Potential energy surfaces of the $^{354}134$ nucleus obtained in the RMF+BCS calculations.

This is illustrated by the calculations of the $^{354}134$ (Fig. 8.7: The blue line shows static fission path from the minimum indicated by the open white circle; the saddle point at 4.4 MeV (with respect to the minimum) is shown by black cross. The energy difference between two neighboring equipotential lines is equal to 5 MeV and 2 MeV in left and right panels, respectively.) nucleus, for which the $N_F = 20$ basis provides acceptable numerical accuracy. In these nuclei, the oblate minimum with $\beta_2 \sim -2.5, \beta_4 \sim -4.4$ is unstable with respect to triaxial distortions (left panel of Fig. 8.7). On the contrary, the excited $\beta_2 \sim -2.3, \beta_4 \sim +1.5$ minimum is stable with respect to triaxial distortions (see right panel of Fig. 8.7).

8.4 Metastable spherical shapes: fission barriers and their dependence on the functionals.

The triaxial RHB calculations for the $|\beta_2| \leq 1.0$ part of the deformation plane clearly indicate the general trend of the reduction of the stability of the minima located at these deformations with respect to fission with increasing proton number. The triaxial RMF+BCS calculations also indicate the potential stability of toroidal shapes located in the minima with $\beta_2 < -2.0$ with $\beta_4 > 0$. Unfortunately, the systematic triaxial calculations of the stability of such minima are beyond available computational power. Thus, their more detailed investigation is left for future.

Note also that toroidal nuclei are expected to be unstable against multifragmentation [262, 263]. The most detailed investigation of the instabilities of toroidal nuclei with respect of so-called breathing and sausage deformations has been performed in Ref. [263]. The breathing deformation preserves the azimuthal symmetry of the torus and it is defined by the radius of torus and the radius of its tube. In our calculations, this type of deformation is related to the β_2 values (see discussion of Fig. 8.4 above). The results of Ref. [263] clearly indicate the stability of toroidal nuclei with respect of breathing deformation both in liquid-drop model calculations and in Strutinsky type calculations. This is also the case in our calculations which show minima at large negative β_2 values in deformation energy curves presented as a function of β_2 (see Fig. 8.1b,c, and d). The sausage deformations make a torus thicker in one section(s) and thinner in another section(s); they are examplified by the density distributions shown in Fig. 8.3. The analysis of Ref. [263] clearly indicates the instability of toroidal nuclei with respect of sausage deformations in the liquid

drop model. However, it was not excluded in Ref. [263] that the instability in the sausage degree of freedom may be counterbalanced by shell effects at some combinations of proton and neutron numbers and deformations. The situation here is similar to superheavy nuclei which are unstable in liquid drop model. The instability with respect of sausage deformations has not been studied so far in either Strutinsky type models [263] or in density functional theories. However, our results for the $\beta_2 \sim 2.5, \beta_4 \sim -4.4, \gamma = 60^\circ$ solutions in the $^{354}134$ and $^{348}138$ nuclei show for the first time this type of instability also in the framework which takes shell effects into account.

The analysis of the deformation energy curves obtained in axial RHB calculations reveals that hyperheavy nuclei could be stabilized at spherical shapes in some regions (see the insert to Fig. 8.1c). If the toroidal shapes in these nuclei are unstable against triaxial distortions or multifragmentation, these states represent the ground states. From our point of view, this is the most likely scenario. Otherwise, they are excited states frequently located at high excitation energies (Fig. 8.1c). It was verified that these spherical states are stable with respect to triaxial and octupole distortions. The largest island of stability of spherical hyperheavy nuclei is centered around $Z \sim 156, N \sim 310$ (Fig. 8.8a).

The value of the fission barrier height indicated in Fig. 8.8 is defined as the lowest value of the barriers located on the oblate and prolate sides with respect to spherical state in the deformation energy curves (see insert in Fig. 8.1c) obtained in axial RHB calculations. The colormap indicates the height of the fission barrier. Only the nuclei with fission barriers higher than 2 MeV are shown. As verified by the triaxial RHB calculations for a number of nuclei, the inclusion of triaxiality does not lower the value of fission barrier heights in

absolute majority of the cases. In only one case the inclusion of triaxiality has lowered fission barrier by ~ 0.2 MeV; this is very small correction to fission barriers obtained in axial RHB calculations. Solid lines in the top panel show the boundaries of the region in which the systematic calculations with DD-PC1 have been performed; they correspond to two-proton and two-neutron drip lines obtained in the calculations with $N_F = 20$. The same boundaries were used for the calculations shown in panels (b-d); however, these calculations are focused on search of spherical hyperheavy nuclei and thus they cover only $-1.0 < \beta_2 < 1.0$ deformation range.

In the calculations with the DD-PC1 functional the fission barriers reach 11 MeV for the nuclei located in the center of the island of stability. This is substantially larger than the fission barriers predicted in the CDFT for experimentally observed superheavy nuclei with $Z \sim 114, N \sim 174$ for which calculated inner fission barriers are around 4-5 MeV [236]. Smaller islands of stability of spherical hyperheavy nuclei are predicted at $Z \sim 138, N \sim 230$ and $Z \sim 174, N \sim 410$ (Fig. 8.8a). Since nuclei in these three regions have $N/Z \geq 1.64$ they cannot be formed in laboratory conditions. The only possible environment in which they can be produced is the ejecta of the mergers of neutron stars [264].

Additional calculations have been performed with the DD-ME2 [26], PC-PK1 [79] and NL3* [33] functionals in order to evaluate systematic theoretical uncertainties [65] in the predictions of fission barriers for spherical hyperheavy nuclei. The DD-ME2 functional provides predictions comparable with the DD-PC1 one (Fig. 8.8a,b). In contrast, the PC-PK1 and NL3* functionals predict lower fission barriers and smaller regions of

stability (Fig. 8.8c,d). Note that the nuclear matter properties and the density dependence are substantially better defined for density-dependent (DD*) functionals as compared with non-linear NL3* and PC-PK1 ones [251]. As a consequence, they are expected to perform better for large extrapolations from known regions. The large fission barriers obtained in the density-dependent functionals will lead to substantial stability of spherical hyperheavy nuclei against spontaneous fission. This stability is substantially lower for the NL3* and PC-PK1 functionals.

Note that these spherical states are also relatively stable against α-decay (see supplementary Fig. 4). Theoretical uncertainties in the predictions of the α-decay half-lives due to the use of different empirical formulas for their calculations and the CEDFs are evaluated for the $Z \sim 156, N \sim 310$ region of spherical hyperheavy nuclei in supplementary Figs. 5 and 6, respectively. One can see that when combined these uncertainties could reach 10 orders of magnitude in the center of region. However, even with these uncertainties accounted the α-decay half-lives of many nuclei are substantial exceeding seconds, hours and days ranges. Considering empirical nature of the formulas employed more microscopic studies of the α-decay half-lives would be highly desirable. It is also important in future to investigate other competing decay modes such as cluster [265, 266] and β [267, 268] decays to fully establish the potential stability of spherical hyperheavy nuclei.

Existing atomic calculations suggest that the periodic table of elements ends at $Z \sim 172$ [247, 248, 249]; this takes place when the $1s$ electron binding energy dives below $-2mc^2$. However, these calculations employ the empirical formulas for the root-mean-square (RMS) nuclear charge radii. For example, the calculations of Ref. [247] employ the

formula from Ref. [269] which underestimates the RMS nuclear charge radii as compared with the ones obtained in the RHB calculations. This is exemplified by the values of RMS nuclear charge radii in the $^{368}138$, $^{466}156$ and $^{584}174$ nuclei which are 6.52 fm (6.91 fm), 7.10 fm (7.576 fm), 7.62 fm (8.312 fm) in the calculations with empirical formula of Ref. [269] (the RHB calculations with DD-PC1). Note that these nuclei represent the centers of the islands of stability of spherical hyperheavy nuclei (see Fig. 8.8a). Unfortunately, the impact of nuclear size changes on atomic properties and thus on the end of periodic table of elements has not been investigated in Refs. [247, 248, 249]. However, these differences in the RMS nuclear charge radii are substantial and new atomic calculations are needed to see how they can affect the end of periodic table of elements.

8.5 Concluding remarks

In summary, covariant density functional studies have been performed for superheavy and hyperheavy nuclei with proton numbers $Z = 122 - 180$. In axial RHB calculations the nuclear landscape in the $Z = 122 - 130$ region is dominated by oblate shapes with deformation of $-1.0 < \beta_2 < -0.2$, while all $Z > 140$ nuclei have toroidal shapes in the lowest in energy minima. The inclusion of triaxiality leads to the instability against fission via triaxial plane of the absolute majority of the $Z = 122 - 134$ nuclei the ground states deformations of which lie in the range $-1.0 < \beta_2 < -0.2$. The potential stability against triaxial distortions of toroidal shapes located in the minima with $\beta_2 \sim -2.5$ has been exemplified by the $^{354}134$ and $^{348}138$ nuclei. However, systematic triaxial calculations for such nuclei are beyond available computational resources and thus the question

of the stability of toroidal shapes in the $Z > 130$ nuclei remains open. The calculations indicate three regions of potentially stable spherical hyperheavy nuclei centered around ($Z \sim 138, N \sim 230$), ($Z \sim 156, N \sim 310$) and ($Z \sim 174, N \sim 410$). However, theoretical systematic uncertainties in the predictions of their fission barriers are substantial. These results clearly indicate that the boundaries of nuclear landscape in hyperheavy nuclei are defined by spontaneous fission and not by particle emission as in lower Z nuclei. Moreover, the current study suggests that only localized islands of stability can exist in hyperheavy nuclei.

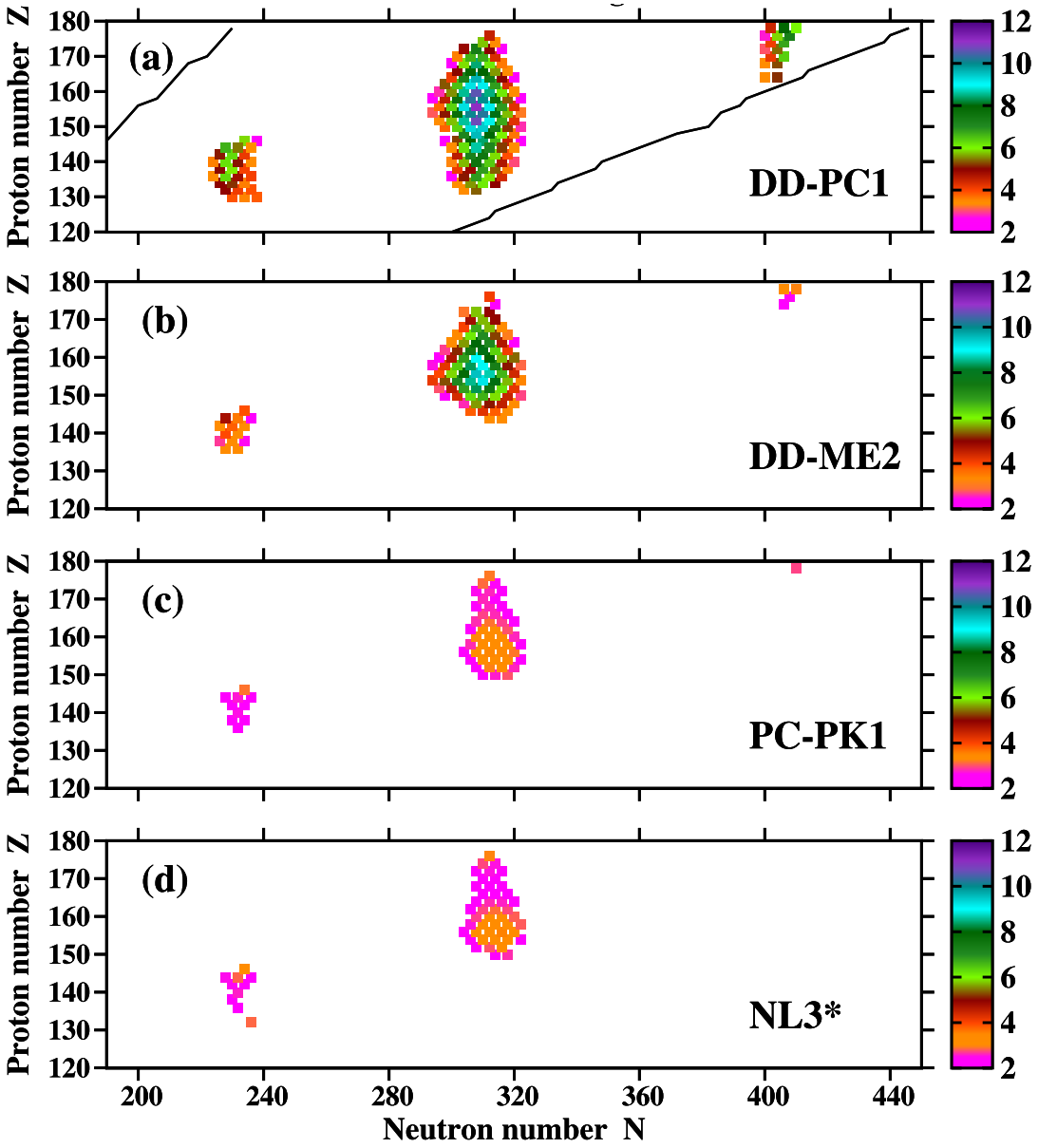

Figure 8.8

The heights of the fission barriers [in MeV] around spherical states.

CHAPTER IX

CONCLUSIONS

In this dissertation we studied the ground state observables of all even-even nuclei from the proton to the neutron drip lines for $Z \leq 106$, the fission properties for superheavy nuclei with $106 \leq Z \leq 126$ from the proton drip line to N = 196 and the existence and stability of hyperheavy nuclei ($Z>126$) using the relativistic variant of the density functional theory (covariant density functional theory, CDFT). The state-of-the-art CEDFs used for these investigations are NL3* [33] and PC-PK1 [79] for the NL (nonlinear) models, DD-ME2 [26] and DD-MEδ [28] for the DD-ME (density dependent - meson exchange) models, and DD-PC1 [27] for the point coupling models. The results obtained within the six projects are summarized as following:

- The aim of the first project was to assess the global performance of the state-of-the art CEDFs and to estimate the differences in the description of various physical observables on a global scale. We developed a parallel version of the axial RHB computer code which allowed us to perform simultaneous calculations for significant number of nuclei and deformation points in each nucleus. The potential energy curves were calculated in a large deformation range from $\beta_2 = -0.4$ up to $\beta_2 = 1.0$ by means of the constraint on the quadrupole moment q_{20}. The CEDFs

NL3*, DD-ME2, DD-MEδ and DD-PC1 were used in this investigation. The ground state observables investigated are the binding energies, two-particle separation energies, charge quadrupole deformations, isovector deformations, charge radii, neutron skin thicknesses and the positions of the two-proton and two-neutron drip lines. A comparison with available experimental data was performed and the predictions for neutron-rich systems for the different CEDFs were quantified. The systematic uncertainties in the predictions of physical observables have been evaluated.

- In the second project, our goal was to investigate the impact of pairing correlations and the underlying shell structure on the position of the two-neutron drip line. Only systematic uncertainties were considered for this investigation. The neutron pairing energies $E_{\rm pairing}$, neutron pairing gaps $\Delta_{\rm uv}$ and the single-particle structure were analyzed. The results strongly suggest that the underlying single-particle structure of different covariant energy density functionals represent the major source of uncertainty in the prediction of the position of the two-neutron drip line.

- For the third project, our goal was to perform a global survey of the octupole deformed nuclei and to estimate the theoretical uncertainties associated with their description. For this project the CEDF PC-PK1 was used together with the ones used in the first and second projects. We performed a global survey of all even-even $Z \leq 106$ nuclei located between the two-proton and two-neutron drip lines and superheavy elements (SHE) with $Z \geq 108, N \sim 190$ employing the DD-PC1 and NL3* CEDFs. For the other CEDFs, a search for octupole deformed nuclei were done around the

regions of octupole deformations predicted with the NL3* and DD-PC1 functionals. The calculations were performed in the Relativistic-Hartree-Bogoliubov (RHB) approach using parallel computer code RHB-OCT developed by us. The investigation confirms the existence of the regions of octupole deformation centered around $Z \sim 92, N \sim 136$, and $Z \sim 96, N \sim 196$ obtained with other models [146, 6]. The search for octupole deformation in the ground states of even-even superheavy $Z = 108 - 126$ nuclei was performed in the CDFT framework for the first time. With exception of two $Z = 108$ (two $Z = 108$ and one $Z = 110$) octupole deformed nuclei in the calculations with CEDF DD-PC1 (DD-ME2), we did not find octupole deformed shapes in the ground states of these nuclei. The systematic theoretical uncertainties in the predictions of quadrupole (β_2) and octupole (β_3) deformations and the gain in binding due to octupole deformation $|\Delta E^{oct}|$ were also quantified.

- The objective of the fourth project was to study the accuracy of the description of the ground state observables and fission barriers of superheavy elements (SHEs) with the new generation of covariant energy density functionals. The RHB framework was used for systematic studies of all $Z = 96 - 126$ even-even actinides and SHEs from the proton-drip line up to neutron number $N = 196$. The ground state observables we investigated are binding energies, two-particle separation energies, charge quadrupole deformations, α-decay properties and fission barrier heights. A comparison with available experimental data was performed. The systematic uncertainties in the predictions of physical observables and fission barrier heights were quantified.

- In the fifth project the goal was to investigate the effects of the nuclear matter properties (NMP) on the description of the ground state properties of finite nuclei. To do this we performed a global analysis of the ground state observables such as binding energies and charge radii. Our investigations revealed that the functionals which are coming close to satisfying all NMP constraints suggested in Ref. [1] perform quite poorly in the description of finite nuclei. On the other hand, the functionals which fail to reproduce the NMP constraints such as NL3* and PC-PK1 are able to reproduce reasonably well the ground state properties of finite nuclei, such as binding energies and charge radii. It was concluded that strict enforcement of the limits on the NMP will not necessary lead to the functionals with good description of ground state properties of neutron-rich systems.

- Finally, in the six project, we investigated different aspects of the existence and stability of hyperheavy nuclei. We found out that beyond $Z = 120$ oblate deformed and toroidal nuclei dominate. The inclusion of triaxiality leads to the instability against fission via triaxial plane of the absolute majority of the $Z = 122 - 134$ nuclei. We concluded that the boundaries of nuclear landscape in hyperheavy nuclei are defined by spontaneous fission and not by particle emission as in lower Z nuclei.

REFERENCES

[1] M. Dutra, O. Lourenco, S. S. Avancini, B. V. Carlson, A. Delfino, D. P. Menezes, C. Providencia, S. Typel, and J. R. Stone. Relativistic mean-field hadronic models under nuclear matter constraints. *Phys. Rev. C*, 90:055203, 2014.

[2] M. Jaminon and C. Mahaux. Effective masses in relativistic approaches to the nucleon-nucleus mean field. *Phys. Rev. C*, 40:354, 1989.

[3] M. Dutra, O. Lourenco, J. S.S̃a Martins, A. Delfino, J.R̃. Stone, and P.D̃. Stevenson. *Phys. Rev. C*, 85:035201, 2012.

[4] P. Möller, R. Bengtsson, B.G. Carlsson, P. Olivius, T. Ichikawa, H. Sagawa, and A. Iwamoto. Axial and reflection asymmetry of the nuclear ground state. *At. Data and Nucl. Data Tables*, 94(5):758–780, 2008.

[5] J. Erler, N. Birge, M. Kortelainen, W. Nazarewicz, E. Olsen, A. M. Perhac, and M. Stoitsov. The limits of the nuclear landscape. *Nature*, 486:509, 2012.

[6] P. Möller, J. R. Nix, W. D. Myers, and W. J. Swiatecki. Nuclear ground-state masses and deformations. *At. Data Nucl. Data Table*, 59:185, 1995.

[7] J.-P. Delaroche, M. Girod, J. Libert, H. Goutte, S. Hilaire, S. Peru, N. Pillet, and G. F. Bertsch.

[8] I. Angeli and K. P. Marinova. Table of experimental nuclear ground state charge radii: An update. *At. Data Nucl. Data Tables*, 99:69, 2013.

[9] H. Schatz. *private communication, see also https://groups.nscl.msu.edu/frib/rates/fribrates.html*, 2014.

[10] Yu.T̃s. Oganessian and V.K̃. Utyonkov. Super-heavy element research. *Rep. Prog. Phys.*, 78:036301, 2015.

[11] *Evaluated Nuclear Structure Data File (ENSDF) located at the website (http://www.nndc.bnl.gov/ensdf/) of Brookhaven National Laboratory. ENSDF is based on the publications presented in Nuclear Data Sheets (NDS) which is a standard for evaluated nuclear data.*, 2015.

[12] M. Wang, G. Audi, A. H. Wapstra, F. G. Kondev, M. MacCormick, X. Xu, and B. Pfeiffer. *Chinese Physics*, C36:1603, 2012.

[13] G. Audi, F.G. Kondev, M. Wang, B. Pfeiffer, X. Sun, J. Blachot, and M. MacCormick. The nubase2012 evaluation of nuclear properties. *Chinese Physics C*, 36(12):1157, 2012.

[14] Bruce R. Barrett, Petr Navrátil, and James P. Vary. Ab initio no core shell model. *Progress in Particle and Nuclear Physics*, 69:131 – 181, 2013.

[15] E. Caurier, G. Martínez-Pinedo, F. Nowacki, A. Poves, and A. P. Zuker. The shell model as a unified view of nuclear structure. *Rev. Mod. Phys.*, 77:427–488, Jun 2005.

[16] W. Kohn and L. J. Sham. Quantum density oscillations in an inhomogeneous electron gas. *Phys. Rev.*, 137:A1697, 1965.

[17] W. Kohn and L. J. Sham. Self-consistent equations including exchange and correlation effects. *Phys. Rev.*, 140:A1133, 1965.

[18] W. Younes and D. Gogny. Microscopic calculation of $^{240}\mathrm{Pu}$ scission with a finite-range effective force. *Phys. Rev. C*, 80:054313, 2009.

[19] G. A. Lalazissis P. Ring and D. Vretenar. Extended density functionals in nuclear structure physics, *lecture notes in physics*, edited by G. A. Lalazissis, P. Ring, and D. Vretenar. *(Springer-Verlag, Heidelberg, 2004)*, Vol. 641, 2004.

[20] T. D. Cohen, R. J. Furnstahl, and K. Griegel. Quark and gluon condensates in nuclear matter. *Phys. Rev. C*, 45:1881, 1992.

[21] J. Dobaczewski and J. Dudek. Time-odd components in the mean field of rotating superdeformed nuclei. *Phys. Rev. C*, 52:1827, 1995.

[22] R. Brockmann and H. Toki. Relativistic density-dependent hartree approach for finite nuclei. *Phys. Rev. Lett.*, 68:3408, 1992.

[23] F. Hofmann, C. M. Keil, and H. Lenske. Density dependent hadron field theory for asymmetric nuclear matter and exotic nuclei. *Phys. Rev. C*, 64:034314, 2001.

[24] M. Serra, T. Otsuka, Y. Akaishi, P. Ring, and S. Hirose. Relativistic mean field models and nucleon-nucleon interactions. *Prog. Theor. Phys.*, 113:1009, 2005.

[25] S. Hirose, M. Serra, P. Ring, T. Otsuka, and Y. Akaishi. Relativistic mean field model based on realistic nuclear forces. *Phys. Rev. C*, 75:024301, 2007.

[26] G. A. Lalazissis, T. Nikšić, D. Vretenar, and P. Ring. New relativistic mean-field interaction with density-dependent meson-nucleon couplings. *Phys. Rev. C*, 71:024312, 2005.

[27] T. Nikšić, D. Vretenar, and P. Ring. Relativistic nuclear energy density functionals: adjusting parameters to binding energies. *Phys. Rev. C*, 78:034318, 2008.

[28] X. Roca-Maza, X. Viñas, M. Centelles, P. Ring, and P. Schuck. Relativistic mean-field interaction with density-dependent meson-nucleon vertices based on microscopical calculations. *Phys. Rev. C*, 84:054309, 2011.

[29] D. Vretenar, A. V. Afanasjev, G. A. Lalazissis, and P. Ring. Relativistic hartree-bogoliubov theory: Static and dynamic aspects of exotic nuclear structure. *Phys. Rep.*, 409:101, 2005.

[30] T. Nikšić, D. Vretenar, and P. Ring. Relativistic nuclear energy density functionals: Mean-field and beyond. *Prog. Part. Nucl. Phys.*, 66:519, 2011.

[31] Yu. Ts. Oganessian, V. K. Utyonkov, Yu. V. Lobanov, F. Sh. Abdullin, A. N. Polyakov, R. N. Sagaidak, I. V. Shirokovsky, Yu. S. Tsyganov, A. A. Voinov, G. G. Gulbekian, S. L. Bogomolov, B. N. Gikal, A. N. Mezentsev, S. Iliev, V. G. Subbotin, A. M. Sukhov, K. Subotic, V. I. Zagrebaev, G. K. Vostokin, M. G. Itkis, K. J. Moody, J. B. Patin, D. A. Shaughnessy, M. A. Stoyer, N. J. Stoyer, P. A. Wilk, J. M. Kenneally, J. H. Landrum, J. F. Wild, and R. W. Lougheed. Synthesis of the isotopes of elements 118 and 116 in the $^{249}\mathrm{Cf}$ and $^{245}\mathrm{Cm}$ $+^{48}\mathrm{Ca}$ fusion reactions. *Phys. Rev. C*, 74:044602, Oct 2006.

[32] Yu. Ts. Oganessian, F. Sh. Abdullin, C. Alexander, J. Binder, R. A. Boll, S. N. Dmitriev, J. Ezold, K. Felker, J. M. Gostic, R. K. Grzywacz, J. H. Hamilton, R. A. Henderson, M. G. Itkis, K. Miernik, D. Miller, K. J. Moody, A. N. Polyakov, A. V. Ramayya, J. B. Roberto, M. A. Ryabinin, K. P. Rykaczewski, R. N. Sagaidak, D. A. Shaughnessy, I. V. Shirokovsky, M. V. Shumeiko, M. A. Stoyer, N. J. Stoyer, V. G. Subbotin, A. M. Sukhov, Yu. S. Tsyganov, V. K. Utyonkov, A. A. Voinov, and G. K. Vostokin. Production and decay of the heaviest nuclei $^{293,294}117$ and $^{294}118$. *Phys. Rev. Lett.*, 109:162501, Oct 2012.

[33] G. A. Lalazissis, S. Karatzikos, R. Fossion, D. Peña Arteaga, A. V. Afanasjev, and P. Ring. The effective force nl3 revisited. *Phys. Lett.*, B671:36, 2009.

[34] Y.K̃. Gambhir, P. Ring, and A. Thimet. *Ann. Phys. (N.Y.)*, 198:132, 1990.

[35] J. D. Walecka. *Ann. Phys. (N.Y.)*, 83:491, 1974.

[36] B. D. Serot and J. D. Walecka. The relativistic nuclear many body problem. *Adv. Nucl. Phys.*, 16:1, 1986.

[37] J. Boguta and R. Bodmer. *Nucl. Phys.*, A292:413, 1977.

[38] G.Ã. Lalazissis, J. König, and P. Ring. *Phys. Rev. C*, 55:540, 1997.

[39] S. Typel and H.H̃. Wolter. *Nucl. Phys.*, A656:331, 1999.

[40] S. E. Agbemava, A. V. Afanasjev, D. Ray, and P. Ring. Global performance of covariant energy density functionals: Ground state observables of even-even nuclei and the estimate of theoretical uncertainties. *Phys. Rev. C*, 89:054320, 2014.

[41] T. Nikšić, D. Vretenar, P. Finelli, and P. Ring. Relativistic hartree-bogoliubov model with density dependent meson-nucleon couplings. *Phys. Rev. C*, 66:024306, 2002.

[42] A.Ã. Nikolaus, T. Hoch, and D. Madland. *Phys. Rev. C*, 46:1757, 1992.

[43] P. Ring. Relativistic mean field theory in finite nuclei. *Prog. Part. Nucl. Phys.*, 37:193, 1996.

[44] H. Kucharek and P. Ring. Relativistic field theory of superfluidity in nuclei. *Z. Phys. A*, 339(1):23–35, March 1991.

[45] A. V. Afanasjev, P. Ring, and J. König. Cranked relativistic hartree-bogoliubov theory: formalism and application to the superdeformed bands in the $a \sim 190$ region. *Nucl. Phys.*, A676:196, 2000.

[46] P. Ring and P. Schuck. The Nuclear Many-Body Problem *(Springer-Verlag, Berlin)*, 1980.

[47] J. Meng and P. Ring. Relativistic hartree-bogoliubov description of the neutron halo in 11li. *Phys. Rev. Lett.*, 77(19):3963–3966, Nov 1996.

[48] Y. N. Zhang, J. C. Pei, and F. R. Xu. Hfb descriptions of deformed weakly bound nuclei in large coordinate spaces. *Phys. Rev. C*, 88:054305, 2013.

[49] Lulu Li, Jie Meng, P. Ring, En-Guang Zhao, and Shan-Gui Zhou. Deformed relativistic hartree-bogoliubov theory in continuum. *Phys. Rev. C*, 85:024312, Feb 2012.

[50] A. V. Afanasjev and H. Abusara. Time-odd mean fields in covariant density functional theory: nonrotating systems. *Phys. Rev. C*, 81:014309, 2010.

[51] W. Koepf and P. Ring. A relativistic description of rotating nuclei: the yrast line of ^{20}ne. *Nucl. Phys. A*, 493:61, 1989.

[52] A. V. Afanasjev, T. L. Khoo, S. Frauendorf, G. A. Lalazissis, and I. Ahmad. Cranked relativistic hartree-bogoliubov theory: Probing the gateway to superheavy nuclei. *Phys. Rev. C*, 67:024309, 2003.

[53] A. V. Afanasjev and S. Shawaqfeh. Deformed one-quasiparticle states in covariant density functional theory. *Phys. Lett. B*, 706:177, 2011.

[54] A. V. Afanasjev and O. Abdurazakov. Pairing and rotational properties of actinides and superheavy nuclei in covariant density functional theory. *Phys. Rev. C*, 88:014320, 2013.

[55] T. Gonzalez-Llarena, J.L̃. Egido, G.Ã. Lalazissis, and P. Ring. *Phys. Lett. B*, 379:13–19, 1996.

[56] J. F. Berger, M. Girod, and D. Gogny. *Comp. Phys. Comm.*, 63:365, 1991.

[57] J.F̃. Berger, M. Girod, and D. Gogny. Microscopic analysis of collective dynamics in low energy fission. *Nucl. Phys.*, A428:23c, 1984.

[58] Y. Tian, Z. Y. Ma, and P. Ring. A finite range pairing force for density functional theory in superfluid nuclei. *Phys. Lett. B*, 676:44, 2009.

[59] J. Dobaczewski, P. Magierski, W. Nazarewicz, W. Satula, and Z. Szymański. *Phys. Rev. C*, 63:024308, 2001.

[60] A.Ṽ. Afanasjev, J. König, P. Ring, L.M̃. Robledo, and J.L̃. Egido. Moments of inertia of nuclei in the rare earth region: A relativistic versus nonrelativistic investigation. *Phys. Rev. C*, 62:054306, 2000.

[61] A. V. Afanasjev. Microscopic description of rotation: From ground states to the extremes of ultra-high spin. *Phys. Scr.*, 89:054001, 2014.

[62] L. J. Wang, B. Y. Sun, J. M. Dong, and W. H. Long. Odd-even staggering of the nuclear binding energy described by covariant density functional theory with calculations for spherical nuclei. *Phys. Rev. C*, 87:054331, 2013.

[63] D. Ray and A.Ṽ. Afanasjev. *in preparation*.

[64] P. G. Reinhard and W. Nazarewicz. Information content of a new observable: The case of the nuclear neutron skin. *Phys. Rev. C*, 81:051303(R), 2010.

[65] J. Dobaczewski, W. Nazarewicz, and P.-G. Reinhard. Error estimates of theoretical models: a guide. *J. Phys. G*, 41:074001, 2014.

[66] M. Kortelainen, J. Erler, W. Nazarewicz, N. Birge, Y. Gao, and E. Olsen. Neutron-skin uncertainties of skyrme energy density functionals. *Phys. Rev. C*, 88:031305(R), 2013.

[67] P. Ring, Y.K̃. Gambhir, and G.Ã. Lalazissis. *Comp. Phys. Comm.*, 105:77, 1997.

[68] P. Bonche, H. Flocard, and P.H̃. Heenen. Solution of the skyrme hf+bcs equation on a 3d mesh. *Comp. Phys. Comm.*, 171:49, 2005.

[69] T. Bürvenich, M. Bender, J. A. Maruhn, and P.-G. Reinhard. Systematics of fission barriers in superheavy elements. *Phys. Rev. C*, 69:014307, 2004.

[70] H. Abusara, A. V. Afanasjev, and P. Ring. Fission barriers in covariant density functional theory: extrapolation to superheavy nuclei. *Phys. Rev. C*, 85:024314, 2012.

[71] D. Hirata, K. Sumiyoshi, I. Tanihata, Y. Sugahara, T. Tachibana, and H. Toki. A systematic study of even-even nuclei up to the drip lines within the relativistic mean field framework. *Nucl. Phys.*, A616:438c, 1997.

[72] G. A. Lalazissis, S. Raman, and P. Ring. Ground-state properties of even-even nuclei in the relativistic mean-field theory. *At. Data Nucl. Data Table*, 71:1, 1999.

[73] L. Geng, H. Toki, and J. Meng. Masses, deformations and charge radii - nuclear ground-state properties in the relativistic mean field model. *Prog. Theor. Phys.*, 113:785, 2005.

[74] J. Dobaczewski, H. Flocard, and J. Treiner. Hartree-fock-bogolyubov description of nuclei near the neutron-drip line. *Nucl. Phys.*, A422:103, 1984.

[75] P.-G. Reinhard and B. K. Agrawal. Energy systematics of heavy nuclei - mean field models in comparison. *Int. Jour. Mod. Phys.*, E20:1379, 2011.

[76] B.G̃. Todd-Rutel and J. Piekarewicz. Neutron-rich nuclei and neutron stars: a new accurately calibrated interaction for the study of neutron-rich matter. *Phys. Rev. Lett.*, 95:122501, 2005.

[77] B. K. Agrawal. Asymmetric nuclear matter and neutron skin in an extended relativistic mean-field model. *Phys. Rev. C*, 81:034323, Mar 2010.

[78] Y. Sugahara and H. Toki. Relativistic mean-field theory for unstable nuclei with non-linear sigma and omega terms. *Nucl. Phys. A*, 579:557 – 572, 1994.

[79] P. W. Zhao, Z. P. Li, J. M. Yao, and J. Meng. New parametrization for the nuclear covariant energy density functional with a point-coupling interaction. *Phys. Rev. C*, 82:054319, 2010.

[80] Q. S. Zhang, Z. M. Niu, Z. P. Li, J. M. Yao, and J. Meng. Global dynamical correlation energies in covariant density functional theory: cranking approximation. *Frontiers of Physics*, 9:529, 2014.

[81] S. Baroni, F. Barranco, P. F. Bortignon, R. A. Broglia, G. Coló, and E. Vigezzi. Medium polarization isotopic effects on nuclear binding energies. *Phys. Rev. C*, 74:024305, 2006.

[82] S. Goriely, N. Chamel, and J. M. Pearson. Skyrme-hartree-fock-bogoliubov nuclear mass formulas: crossing the 0.6 mev accuracy threshold with microscopically deduced pairing. *Phys. Rev. Lett.*, 102:152503, 2009.

[83] S. Goriely, S. Hilaire, M. Girod, and S. Péru. First gogny-hartree-fock-bogoliubov nuclear mass model. *Phys. Rev. Lett.*, 102:242501, 2009.

[84] A. V. Afanasjev, S. E. Agbemava, D. Ray, and P. Ring. Nuclear landscape in covariant density functional theory. *Phys. Lett. B*, 726:680, 2013.

[85] G.Ã. Lalazissis and S. Raman. Proton drip-line in relativistic mean-field theory. *Phys. Rev. C*, 58:1467, 1998.

[86] D. Vretenar, G.Ã. Lalazissis, and P. Ring. Proton drip-line nuclei in relativistic hartree-bogoliubov theory. *Phys. Rev. C*, 57:3071, 1998.

[87] D. Vretenar, G.Ã. Lalazissis, and P. Ring. Relativistic hartree-bogoliubov description of the deformed ground state proton emitters. *Phys. Rev. C*, 57:3071, 1999.

[88] G. A. Lalazissis, D. Vretenar, and P. Ring. Ground-state properties of deformed proton emitters in the relativistic hartree-bogoliubov model. *Nucl. Phys. A*, 650:133–155, 1999.

[89] G. A. Lalazissis, D. Vretenar, and P. Ring. Transitional lu and spherical ta ground-state proton emitters in the relativistic hartree-bogoliubov model. *Phys. Rev. C*, 60:051302R, 1999.

[90] G. A. Lalazissis, D. Vretenar, and P. Ring. Mapping the proton drip line from $z = 31$ to $z = 49$. *Nucl. Phys. A*, 679:481, 2001.

[91] G. A. Lalazissis, D. Vretenar, and P. Ring. Mapping the proton drip line in the suburanium region and for superheavy elements. *Phys. Rev. C*, 69:173011, 2004.

[92] A. Corsi, J.-P. Delaroche, A. Obertelli, T. Baugher, D. Bazin, S. Boissinot, F. Flavigny, A. Gade, M. Girod, T. Glasmacher, G.F̃. Grinyer, W. Korten, J. Libert, J. Ljungvall, S. McDaniel, A. Ratkiewicz, A. Signoracci, R. Stroberg, B. Sulignano, and D. Weisshaar. Collectivity of light ge and as isotopes. *Phys. Rev. C*, 88:044311, 2013.

[93] J. Ljungvall, A. Görgen, M. Girod, J.-P. Delaroche, A. Dewald, C. Dossat, E. Farnea, W. Korten, B. Melon, R. Menegazzo, A. Obertelli, R. Orlandi, P. Petkov, T. Pissulla, S. Siem, R.P̃. Singh, J. Srebrny, Ch. Theisen, C. A.Ũr andÂ J. J. Valiente-Dobon, K.Õ. Zell, and M. Zielińska. Shape coexistence in light se isotopes: Evidence for oblate shapes. *Phys. Rev. Lett.*, 100:102502, 2008.

[94] N. Hinohara, T. Nakatsukasa, M. Matsuo, and K. Matsuyanagi. Microscopic description of oblate-prolate shape mixing in proton-rich se isotopes. *Phys. Rev. C*, 80:014305, 2009.

[95] E. Clément, A. Görgen, W. Korten, E. Bouchez, A. Chatillon, J.-P. Delaroche, M. Girod, H. Goutte, A. Hörstel, Y.L̃e Coz, A. Obertelli, S. Péru, Ch. Theisen, J.Ñ. Wilson, M. Zielińska, C. Andreoiu, F. Becker, P.Ã. Butler, J.M̃. Casandjian, W.Ñ. Catford, T. Czosnyka, G. de France, J. Gerl, R.-D. Herzberg, J̇wanicki, D.G̃. Jenkins, G.D̃. Jones, P.J̃. Napiorkowski, G. Sletten, and C.Ñ. Timis. Shape coexistence in neutron-deficient krypton isotopes. *Phys. Rev. C*, 75:054313, 2007.

[96] Y. Fu, H. Mei, J. Xiang, Z.P̃. Li, J.M̃. Yao, and J. Meng. Beyond relativistic mean-field studies of low-lying states in neutron-deficient krypton isotopes. *Phys. Rev. C*, 87:054305, 2013.

[97] A. V. Afanasjev and S. Frauendorf. Description of rotating $n = z$ nuclei in terms of isovector pairing. *Phys. Rev. C*, 71:064318, 2005.

[98] M. Bender, G. F. Bertsch, and P.-H. Heenen. Global study of quadrupole correlation effects. *Phys. Rev. C*, 73:034322, 2006.

[99] C.D̃. O'Leary, C.Ẽ. Svensson, S.G̃. Frauendorf, A.Ṽ. Afanasjev, D.Ẽ. Appelbe, R. A.Ẽ. Austin, G.C̃. Ball, J.Ã. Cameron, R.M̃. Clark, M. Cromaz, P. Fallon, D.F̃. Hodgson, N.S̃. Kelsall, A.Õ. Macchiavelli, I. Ragnarsson, D. Sarantites, J.C̃. Waddington, and R. Wadsworth. Evidence for isovector neutron-proton pairing from high-spin states in $n = z$ ^{74}rb. *Phys. Rev. C*, 67:021301(R), 2003.

[100] J.M̃. Yao, M. Bender, and P.-H. Heenen. Systematics of low-lying states of even-even nuclei in the neutron-deficient lead region from a beyond-mean-field calculation. *Phys. Rev. C*, 87:034322, 2013.

[101] P. Rahkila, D.G̃. Jenkins, J. Pakarinen, C. Gray-Jones, P.T̃. Greenlees, U. Jakobsson, P. Jones, R. Julin, S. Juutinen, S. Ketelhut, H. Koivisto, M. Leino, P. Nieminen, M. Nyman, P. Papadakis, S. Paschalis, M. Petri, P. Peura, O.J̃. Roberts, T. Ropponen, P. Ruotsalainen, J. Sarén, C. Scholey, J. Sorri, A.G̃. Tuff, J. Uusitalo, R. Wadsworth, M. Bender, and P.-H. Heenen. Shape coexistence at the proton drip-line: First identification of excited states in ^{180}pb. *Phys. Rev. C*, 82:011303(R), 2010.

[102] J. Erler, C.J̃. Horowitz, W. Nazarewicz, M. Rafalski, and P.-G. Reinhard. *Phys. Rev. C*, 87:044320, 2013.

[103] E. V. Litvinova and A. V. Afanasjev. Dynamics of nuclear single-particle structure in covariant theory of particle-vibration coupling: From light to superheavy nuclei. *Phys. Rev. C*, 84:014305, 2011.

[104] J. Bartel, P. Quentin, M. Brack, C. Guet, and H.-B. Hakansson. Towards a better parametrisation of skyrme-like effective forces: A critical study of the skm force. *Nucl. Phys.*, A386:79, 1982.

[105] M. Kortelainen, J. McDonnell, W. Nazarewicz, E. Olsen, P.-G. Reinhard, J. Sarich, N. Schunck, S. M. Wild, D. Davesne, J. Erler, and A. Pastore. Nuclear energy density optimization: Shell structure. *Phys. Rev. C*, 89:054314, May 2014.

[106] E. Chabanat, P. Bonche, P. Haensel, J. Meyer, and R. Schaeffer. *Nucl. Phys.*, A635:231, 1998.

[107] F. Chappert, M. Girod, and S. Hilaire. Towards a new gogny force parametrization: impact of the neutron matter equation of state. *Phys. Lett. B*, 668:420, 2008.

[108] J. Dobaczewski, H. Flocard, and J. Treiner. *Nucl. Phys.*, A422:103, 1984.

[109] P. Klüpfel, P.-G. Reinhard, T.J̃. Bürvenich, and J.Ã. Maruhn. *Phys. Rev. C*, 79:034310, 2009.

[110] S. Goriely, N. Chamel, and J. M. Pearson. Further exploration of skyrme hfb mass formulas. xii. stiffness and stability of neutron-star matter. *Phys. Rev. C*, 82:035804, 2010.

[111] S. Raman, C.H̃. Malarkey, W.T̃. Milner, C.W̃. Nestor, Jr., and P.H̃. Stelson. *At. Data Nucl. Data Tables*, 36, 1987.

[112] L. Grodzins. *Phys. Lett.*, 2:88, 1962.

[113] R.-D. Herzberg, N. Amzal, F. Becker, P.Ã. Butler, A. J.C̃. Chewter, J. F.C̃. Cocks, O. Dorvaux, K. Eskola, J. Gerl, P.T̃. Greenlees, N.J̃. Hammond, K. Hauschild, K. Helariutta, F. Heβberger, M. Houry, G.D̃. Jones, P.M̃. Jones, R. Julin, S. Juutinen, H. Kankaanpää, H. Kettunen, T.L̃. Khoo, W. Korten, P. Kuusiniemi, Y.L̃e Coz, M. Leino, C.J̃. Lister, R. Lucas, M. Muikku, P. Nieminen, R.D̃. Page, P. Rahkila, P. Reiter, Ch. Schlegel, C. Scholey, O. Stezowski, Ch. Theisen, W.H̃. Trzaska, J. Uusitalo, and H.J̃. Wollersheim. *Phys. Rev. C*, 65:014303, 2001.

[114] I.Ñ. Boboshin, V.Ṽ. Varlamov, B.S̃. Ishkhanov, S.Ỹu. Komarov, and V.N. Orlin. Quadrupole deformation of nucleus and dynamic vibrations of its surface. *Bulletin of the Russian Academy of Sciences: Physics*, 71(3):320, 2007.

[115] K. Heyde and J.L̃. Wood. Shape coexistence in atomic nuclei. *Rev. Mod. Phys.*, 83:467, 2011.

[116] T. Nikšić, D. Vretenar, G. A. Lalazissis, and P. Ring. Microscopic description of nuclear quantum phase transitions. *Phys. Rev. Lett.*, 99:092502, 2007.

[117] Z.P̃. Li, T. Nikšić, D. Vretenar, J. Meng, G.Ã. Lalazissis, and P. Ring. Microscopic analysis of nuclear quantum phase transitions in the $n \approx 90$ region. *Phys. Rev. C*, 79:054301, 2009.

[118] W. Bertozzi, J. Friar, J. Heisenberg, and J.W̃. Negele. *Phys. Lett. B*, 41:408, 1972.

[119] M. Nishimura and D. W.L̃. Sprung. *Prog. Theor. Phys.*, 77:781, 1987.

[120] T. Nikšić, D. Vretenar, P. Ring, and G.Ã. Lalazissis. Shape coexistence in the rhb approach. *Phys. Rev. C*, 65:054320, 2002.

[121] A. Brown. Neutron radii in nuclei and the neutron equation of state. *Phys. Rev. Lett.*, 85:5296, 2000.

[122] X. Roca-Maza, M. Centelles, X. Viñas, and M. Warda. Neutron skin in ^{208}pb, nuclear symmetry energy and the parity radius experiment. *Phys. Rev. Lett.*, 106:252501, 2011.

[123] C. J. Horowitz and J. Piekarewicz. Neutron star structure and the neutron radius of ^{208}pb. *Phys. Rev. Lett.*, 86:5647, 2001.

[124] A.W̃. Steiner, M. Prakash, J.M̃. Lattimer, and P.J̃. Ellis. Isospin asymmetry in nuclei and neutron stars. *Phys. Rep.*, 411:325, 2005.

[125] F. J. Fattoyev and J. Piekarewicz. Neutron skin and neutron stars. *Phys. Rev. C*, 86:015802, 2013.

[126] A. Krasznahorkay, N. Paar, D. Vretenar, and M. N. Harakeh. Neutron-skin thickness of 208pb from the energy of the anti-analogue giant dipole resonance. *Phys. Scripta*, T154:014018, 2013.

[127] M.B̃. Tsang, J.R̃. Stone, F. Camera, P. Danielewicz, S. Gandolfi, K. Hebeler, C.J̃. Horowitz, Jenny Lee, W.G̃. Lynch, Z. Kohley, R. Lemmon, P. Möller, T. Murakami, S. Riordan, X. Roca-Maza, F. Sammarruca, A.W̃. Steiner, I. Vidaña, and S.J̃. Yennello. Constraints on the symmetry energy and neutron skins from experiments and theory. *Phys. Rev. C*, 86:015803, 2012.

[128] A. Krasznahorkay, M. Csatlós, L. Csige, T.K̃. Eriksen, F. Giacoppo, A. Görgen, T.W̃. Hagen, M.Ñ. Harakeh, R. Julin, P. Koehler, N. Paar, S. Siem, L. Stuhl, T. Tornyi, and D. Vretenar. Neutron-skin thickness of 208pb, and symmetry-energy constraints from the study of the anti-analog giant dipole resonance. *arXiv:1311.1456v2 [nucl-ex]*, 2013.

[129] C. M. Tarbert, D.P̃. Watts, D.Ĩ. Glazier, P. Aguar, J. Ahrens, J. R.M̃. Annand, H.J̃. Arends, R. Beck, V. Bekrenev, B. Boillat, A. Braghieri, D. Branford, W.J̃. Briscoe, J. Brudvik, S. Cherepnya, R. Codling, E.J̃. Downie, K. Foehl, P. Grabmayr, R. Gregor, E. Heid, D. Hornidge, O. Jahn, V.L̃. Kashevarov, A. Knezevic, R. Kondratiev, M. Korolija, M. Kotulla, D. Krambrich, B. Krusche, M. Lang, V. Lisin, K. Livingston, S. Lugert, I. J.D̃. MacGregor, D.M̃. Manley, M. Martinez, J.C̃. McGeorge, D. Mekterovic, V. Metag, B. M.K̃. Nefkens, A. Nikolaev, R. Novotny, R.Õ. Owens, P. Pedroni, A. Polonski, S.Ñ. Prakhov, J.W̃. Price, G. Rosner, M. Rost, T. Rostomyan, S. Schadmand, S. Schumann, D. Sober, A. Starostin, I. Supek, A. Thomas, M. Unverzagt, Th. Walcher, and F. Zehr. The neutron skin of 208pb from coherent pion photoproduction. *arXiv:1311.0168v2 [nucl-ex]*, 2013.

[130] S. Abrahamyan et al. Measurement of the neutron radius of ^{208}pb through parity violation in electron scattering. *Phys. Rev. Lett.*, 108:112502, 2012.

[131] C. J. Horowitz. Parity violating elastic electron scattering and coulomb distortions. *Phys. Rev. C*, 57:3430, 1998.

[132] F. J. Fattoyev and J. Piekarewicz. Has a thick neutron skin in ^{208}pb been ruled out? *Phys. Rev. Lett.*, 111:162501, 2013.

[133] The prex-ii proposal, unpublished, available at hallaweb.jlab.org/parity/prex. *The PREX-II proposal, unpublished, available at hallaweb.jlab.org/parity/prex.*

[134] T. Niksic, D. Vretenar, and P. Ring. Relativistic nuclear energy density functionals: Mean-field and beyond. *Prog. Part. Nucl. Phys.*, 66(3):519 – 548, 2011.

[135] G. F. Bertsch and H. Esbensen. Pair correlations near the neutron drip line. *Ann. Phys. (N.Y.)*, 209(2):327 – 363, 1991.

[136] A. Pastore, J. Margueron, P. Schuck, and X. Viñas. Pairing in exotic neutron rich nuclei around the drip line and in the crust of neutron stars. *Phys. Rev. C*, 88:034314, Sep 2013.

[137] A. V. Afanasjev, S. E. Agbemava, D. Ray, and P. Ring. Neutron drip line: Single-particle degrees of freedom and pairing properties as sources of theoretical uncertainties. *Phys. Rev. C*, 91:014324, 2015.

[138] P.-G. Reinhard, M. Rufa, J. Maruhn, W. Greiner, and J. Friedrich. Nuclear ground state properties in a relativistic meson field model. *Z. Phys. A*, 323:13, 1986.

[139] T. Bürvenich, D. G. Madland, J. A. Maruhn, and P.-G. Reinhard. Nuclear ground state observables and qcd scaling in a refined relativistic point coupling model. *Phys. Rev. C*, 65:044308, 2002.

[140] E. Litvinova and P. Ring. Covariant theory of particle-vibrational coupling and its effect on the single-particle spectrum. *Phys. Rev. C*, 73:044328, 2006.

[141] M. M. Sharma, G. A. Lalazissis, W. Hillebrandt, and P. Ring. Shell effects in nuclei near the neutron-drip line. *Phys. Rev. Lett.*, 72:1431–1434, Mar 1994.

[142] M. Kortelainen, J. Dobaczewski, K. Mizuyama, and J. Toivanen. Dependence of single-particle energies on coupling constants of the nuclear energy density functional. *Phys. Rev. C*, 77:064307, 2008.

[143] M. Bender, K. Rutz, P.-G. Reinhard, and J. A. Maruhn. Pairing gaps from nuclear mean-field models. *Eur. Phys. J. A*, 8:59, 2000.

[144] M. Bender, P.-H. Heenen, and P.-G. Reinhard. Self-consistent mean-field models for nuclear structure. *Rev. Mod. Phys.*, 75:121, 2003.

[145] P. A. Butler and W. Nazarewicz. Intrinsic reflection asymmetry in atomic nuclei. *Rev. Mod. Phys.*, 68:349, 1996.

[146] J. Erler, K. Langanke, H. P. Loens, G. Martinez-Pinedo, and P.-G. Reinhard. Fission properties for $r-$process nuclei. *Phys. Rev. C*, 85:025802, 2012.

[147] Nan Wang, Jie Meng, and En-Guang Zhao. Octupole deformations of even-even rn, th, and u nuclei in relativistic mean field theory. *Comm. Th. Phys.*, 53(6):1145, 2010.

[148] Jian-You Guo, Peng Jiao, and Xiang-Zheng Fang. Microscopic description of nuclear shape evolution from spherical to octupole-deformed shapes in relativistic mean-field theory. *Phys. Rev. C*, 82:047301, Oct 2010.

[149] L. M. Robledo and G. F. Bertsch. Global systematics of octupole excitations in even-even nuclei. *Phys. Rev. C*, 84:054302, Nov 2011.

[150] N. Minkov, S. Drenska, M. Strecker, W. Scheid, and H. Lenske. Non-yrast nuclear spectra in a model of coherent quadrupole-octupole motion. *Phys. Rev. C*, 85:034306, 2012.

[151] R. V. Jolos, P. von Brentano, and J. Jolie. Second order phase transitions from octupole-nondeformed to octupole-deformed shape in the alternating parity bands of nuclei around ^{240}pu based on data. *Phys. Rev. C*, 86:024319, 2012.

[152] Hua-Lei Wang, Hong-Liang Liu, and Fu-Rong Xu. Total routhian surface calculations of octupole properties in neutron-deficient u isotopes. *Phys. Scripta*, 86(3):035201, 2012.

[153] L M Robledo and R R Rodríguez-Guzmán. Octupole deformation properties of actinide isotopes within a mean-field approach. *J. Phys. G*, 39(10):105103, 2012.

[154] Jie Zhao, Bing-Nan Lu, En-Guang Zhao, and Shan-Gui Zhou. Nonaxial-octupole Y_{32} correlations in $n = 150$ isotones from multidimensional constrained covariant density functional theories. *Phys. Rev. C*, 86:057304, Nov 2012.

[155] K. Nomura, D. Vretenar, and B.-N. Lu. Microscopic analysis of the octupole phase transition in th isotopes. *Phys. Rev. C*, 88:021303, Aug 2013.

[156] K. Nomura, D. Vretenar, T. Nikšić, and Bing-Nan Lu. Microscopic description of octupole shape-phase transitions in light actinide and rare-earth nuclei. *Phys. Rev. C*, 89:024312, Feb 2014.

[157] Yong-Jing Chen, Zao-Chun Gao, Yong-Shou Chen, and Ya Tu. Octupole bands and simplex inversion in the neutron-rich nucleus ^{145}Ba. *Phys. Rev. C*, 91:014317, Jan 2015.

[158] K. Nomura, R. Rodríguez-Guzmán, and L. M. Robledo. Spectroscopy of quadrupole and octupole states in rare-earth nuclei from a gogny force. *Phys. Rev. C*, 92:014312, Jul 2015.

[159] Hua-Lei Wang, Jie Yang, Min-Liang Liu, and Fu-Rong Xu. Evolution of ground-state quadrupole and octupole stiffnesses in even-even barium isotopes. *Phys. Rev. C*, 92:024303, Aug 2015.

[160] J. M. Yao, E. F. Zhou, and Z. P. Li. Beyond relativistic mean-field approach for nuclear octupole excitations. *Phys. Rev. C*, 92:041304, Oct 2015.

[161] T. Rzaca-Urban, W. Urban, J. A. Pinston, G. S. Simpson, A. G. Smith, and I. Ahmad. Reflection symmetry of the near-yrast excitations in ^{145}ba. *Phys. Rev. C*, 86:044324, Oct 2012.

[162] T. Rzaca-Urban, W. Urban, A. G. Smith, I. Ahmad, and A. Syntfeld-Każuch. Unexpected $5/2^-$ spin of the ground state in ^{147}ba: No octupole deformation in ground states of odd-a ba isotopes. *Phys. Rev. C*, 87:031305, Mar 2013.

[163] L. P. Gaffney, P. A. Butler, M. Scheck, A. B. Hayes, F. Wenander, M. Albers, B. Bastin, C. Bauer, A. Blazhev, S. Bönig, N. Bree, J. Cederkäll, T. Chupp, D. Cline T. E. Cocolios, T. Davinson, H. De Witte, J. Diriken, T. Grahn, A. Herzan, M. Huyse, D. G. Jenkins, D. T. Joss, N. Kesteloot J. Konki, M. Kowalczyk, Th. Kröll, E. Kwan, R. Lutter, K. Moschner, P. Napiorkowski, J. Pakarinen, M. Pfeiffer, D. Radeck, P. Reiter, K. Reynders, S. V. Rigby, L. M. Robledo, M. Rudigier, S. Sambi, M. Seidlitz, B. Siebeck, T. Stora, P. Thoele, P. Van Duppen, M. J. Vermeulen, M. von Schmid, D. Voulot, N. Warr, K. Wimmer, K. Wrzosek-Lipska, C. Y. W., and M. Zielinska. Studies of pear-shaped nuclei using accelerated radioactive beams. *Nature*, 497:199–204, 2013.

[164] S. K. Tandel, M. Hemalatha, A. Y. Deo, S. B. Patel, R. Palit, T. Trivedi, J. Sethi, S. Saha, D. C. Biswas, and S. Mukhopadhyay. Evolution of octupole collectivity in ^{221}th. *Phys. Rev. C*, 87:034319, Mar 2013.

[165] M. Spieker, D. Bucurescu, J. Endres, T. Faestermann, R. Hertenberger, S. Pascu, S. Skalacki, S. Weber, H.-F. Wirth, N.-V. Zamfir, and A. Zilges. Possible experimental signature of octupole correlations in the 0_2^+ states of the actinides. *Phys. Rev. C*, 88:041303, Oct 2013.

[166] M Scheck, L P Gaffney, P A Butler, A B Hayes, F Wenander, M Albers, B Bastin, C Bauer, A Blazhev, S Bönig, N Bree, J Cederkäil, T Chupp, D Cline, T E Cocolios, T Davinson, H De Witte, J Diriken, T Grahn, E T Gregor, A Herzan, M Huyse, D G Jenkins, D T Joss, N Kesteloot, J Konki, M Kowalczyk, Th Kröll, E Kwan, R Lutter, K Moschner, P Napiorkowski, J Pakarinen, M Pfeiffer, D Radeck, P Reiter, K Reynders, S V Rigby, L M Robledo, M Rudigier, S Sambi, M Seidlitz, B Siebeck, T Stora, P Thoele, P Van Duppen, M J Vermeulen, M von Schmid, D Voulot, N Warr, K Wimmer, K Wrzosek-Lipska, C Y Wu, and M Zielińska. Determination of the b (e 3, 0 + 3)-excitation strength in octupole-correlated nuclei near a 224 by the means of coulomb excitation at rex-isolde. *J. Phys.: Conf. Series*, 533(1):012007, 2014.

[167] H. J. Li, S. J. Zhu, J. H. Hamilton, E. H. Wang, A. V. Ramayya, Y. J. Chen, J. K. Hwang, J. Ranger, S. H. Liu, Z. G. Xiao, Y. Huang, Z. Zhang, Y. X. Luo, J. O. Rasmussen, I. Y. Lee, G. M. Ter-Akopian, Yu. Ts. Oganessian, and W. C. Ma. Reinvestigation of high spin states and proposed octupole correlations in ^{147}Ce. *Phys. Rev. C*, 90:047303, Oct 2014.

[168] I. Ahmad, R. R. Chasman, J. P. Greene, F. G. Kondev, and S. Zhu. Electron capture decay of 58-min $^{229}_{92}$U and levels in $^{229}_{91}$Pa. *Phys. Rev. C*, 92:024313, Aug 2015.

[169] E. Ruchowska, H. Mach, M. Kowal, J. Skalski, W. A. Płóciennik, and B. Fogelberg. Search for octupole correlations in ^{147}Nd. *Phys. Rev. C*, 92:034328, Sep 2015.

[170] H. Abusara, A. V. Afanasjev, and P. Ring. Fission barriers in actinides in covariant density functional theory: the role of triaxiality. *Phys. Rev. C*, 82:044303, 2010.

[171] V. Prassa, T. Nikšić, G. A. Lalazissis, and D. Vretenar. Relativistic energy density functional description of shape transitions in superheavy nuclei. *Phys. Rev. C*, 86:024317, 2012.

[172] Bing-Nan Lu, Jie Zhao, En-Guang Zhao, and Shan-Gui Zhou. Multidimensionally-constrained relativistic mean-field models and potential-energy surfaces of actinide nuclei. *Phys. Rev. C*, 89:014323, Jan 2014.

[173] M. Warda and J. L. Egido. Fission half-lives of superheavy nuclei in a microscopic approach. *Phys. Rev. C*, 86:014322, Jul 2012.

[174] N. Dubray, H. Goutte, and J.-P. Delaroche. Structure properties of $^{226}\mathrm{Th}$ and $^{256,258,260}\mathrm{Fm}$ fission fragments: Mean-field analysis with the gogny force. *Phys. Rev. C*, 77:014310, 2008.

[175] M. Warda and L. M. Robledo. Microscopic description of cluster radioactivity in actinide nuclei. *Phys. Rev. C*, 84:044608, 2011.

[176] R. Rodríguez-Guzmán and L. M. Robledo. Microscopic description of fission in uranium isotopes with the gogny energy density functional. *Phys. Rev. C*, 89:054310, May 2014.

[177] A. Staszczak, A. Baran, and W. Nazarewicz. Spontaneous fission modes and lifetimes of superheavy elements in the nuclear density functional theory. *Phys. Rev. C*, 87:024320, 2013.

[178] J. Sadhukhan, K. Mazurek, A. Baran, J. Dobaczewski, W. Nazarewicz, and J. A. Sheikh. Spontaneous fission lifetimes from the minimization of self-consistent collective action. *Phys. Rev. C*, 88:064314, 2013.

[179] P. Möller, A. J. Sierk, T. Ichikawa, A. Iwamoto, R. Bengtsson, H. Uhrenholt, and S. Åberg. Heavy-element fission barriers. *Phys. Rev. C*, 79:064304, Jun 2009.

[180] M. Kowal, P. Jachimowicz, and A. Sobiczewski. Fission barriers for even-even superheavy nuclei. *Phys. Rev. C*, 82:014303, 2010.

[181] A. N. Andreyev, J. Elseviers, M. Huyse, P. Van Duppen, S. Antalic, A. Barzakh, N. Bree, T. E. Cocolios, V. F. Comas, J. Diriken, D. Fedorov, V. Fedosseev, S. Franchoo, J. A. Heredia, O. Ivanov, U. Köster, B. A. Marsh, K. Nishio, R. D. Page, N. Patronis, M. Seliverstov, I. Tsekhanovich, P. Van den Bergh, J. Van De Walle, M. Venhart, S. Vermote, M. Veselsky, C. Wagemans, T. Ichikawa, A. Iwamoto, P. Möller, and A. J. Sierk. New type of asymmetric fission in proton-rich nuclei. *Phys. Rev. Lett.*, 105:252502, 2010.

[182] L. Csige, D. M. Filipescu, T. Glodariu, J. Gulyás, M. M. Günther, D. Habs, H. J. Karwowski, A. Krasznahorkay, G. C. Rich, M. Sin, L. Stroe, O. Tesileanu, and P. G. Thirolf. Exploring the multihumped fission barrier of ^{238}u via sub-barrier photofission. *Phys. Rev. C*, 87:044321, Apr 2013.

[183] Andrei N. Andreyev, Mark Huyse, and Piet Van Duppen. Beta delayed fission of atomic nuclei. *Rev. Mod. Phys.*, 85:1541–1559, 2013.

[184] K. Rutz, J. A. Maruhn, P. G. Reinhard, and W. Greiner. Fission barriers and asymmetric ground states in the relativistic mean-field theory. *Nucl. Phys. A*, 590:680, 1995.

[185] L. S. Geng, J. Meng, and H. Toki. Reflection asymmetric relativistic mean field approach and its application to the octupole deformed nucleus ^{226}ra. *Chin. Phys. Lett.*, 24:1865, 2007.

[186] W. Zhang, Z.-P. Li, and S.-Q.Zhang. Octupole deformation for ba isotopes in a reflection asymmetric relativistic mean field approach. *Chi. Ph. C*, 34:1094, 2010.

[187] W. Zhang, Z. P. Li, S. Q. Zhang, and J. Meng. Octupole degree of freedom for the critical-point candidate nucleus $^{152}\mathrm{Sm}$ in a reflection-asymmetric relativistic mean-field approach. *Phys. Rev. C*, 81:034302, Mar 2010.

[188] S. E. Agbemava, A. V. Afanasjev, T. Nakatsukasa, and P. Ring. Covariant density functional theory: Reexamining the structure of superheavy nuclei. *Phys. Rev. C*, 92:054310, 2015.

[189] S. Karatzikos, A. V. Afanasjev, G. A. Lalazissis, and P. Ring. The fission barriers in actinides and superheavy nuclei in covariant density functional theory. *Phys. Lett. B*, 689:72, 2010.

[190] R. Rodríguez-Guzmán, L. M. Robledo, and P. Sarriguren. Microscopic description of quadrupole-octupole coupling in sm and gd isotopes with the gogny energy density functional. *Phys. Rev. C*, 86:034336, Sep 2012.

[191] E. F. Zhou, Jiangming Yao, Zhipan Li, Jie Meng, and Peter Ring. Anatomy of molecular structures in 20ne. *Phys. Lett. B*, 753:227, 2016.

[192] E. Garrote, J. L. Egido, and L. M. Robledo. Fingerprints of reflection asymmetry at high angular momentum in atomic nuclei. *Phys. Rev. Lett.*, 80:4398, 1998.

[193] L. M. Robledo. Ground state octupole correlation energy with effective forces. *J. Phys. G*, 42:055109, 2015.

[194] W. Nazarewicz, P. Olanders, I. Ragnarsson, J. Dudek, G.A. Leander, P. Möller, and E. Ruchowsa. Analysis of octupole instability in medium-mass and heavy nuclei. *Nucl. Phys. A*, 429(2):269 – 295, 1984.

[195] S. E. Agbemava, A. V. Afanasjev, and P. Ring. Octupole deformation in the ground states of even-even nuclei: a global analysis within the covariant density functional theory. *Phys. Rev. C*, 93:044304, 2016.

[196] W. Nazarewicz and S. L. Tabor. Octupole shapes and shape changes at high spins in the *Z* 58, *N* 88 nuclei. *Phys. Rev. C*, 45:2226–2237, May 1992.

[197] J.L. Egido and L.M. Robledo. A systematic study of the octupole correlations in the lanthanides with realistic forces. *Nucl. Phys. A*, 545(3):589 – 607, 1992.

[198] J. Dobaczewski, A. V. Afanasjev, M. Bender, L. M. Robledo, and Yue Shi. Properties of nuclei in the nobelium region studied within the covariant, skyrme, and gogny energy density functionals. *Nucl. Phys. A*, 944:388 – 414, 2015.

[199] M. Baldo, C. Maieron, P. Schuck, and X. Viñas. Low densities in nuclear and neutron matters and in the nuclear surface. *Nucl. Phys. A*, 736(3–4):241 – 254, 2004.

[200] E. N. E. van Dalen, Chr. Fuchs, and A. Faessler. Dirac-brueckner-hartree-fock calculations for isospin asymmetric nuclear matter based on improved approximation schemes. *Eur. Phys. J. A*, 31(1):29–42, 2007.

[201] S.G̃. Nilsson, J.R̃. Nix, A. Sobiczewski, Z. Szymański, S. Wycech, C. Gustafson, and P. Möller. On the spontaneous fission of nuclei with z near 114 and n near 184. *Nucl. Phys. A*, 115(3):545 – 562, 1968.

[202] S.G̃. Nilsson, C.F̃. Tsang, A. Sobiczewski, Z. Szymański, S. Wycech, C. Gustafson, I.-L. Lamm, P. Möller, and B. Nilsson. On the nuclear structure and stability of heavy and superheavy elements. *Nucl. Phys. A*, 131:1 – 66, 1969.

[203] Z. Patyk and A. Sobiczewski. Ground-state properties of the heaviest nuclei analyzed in a multidimensional deformation space. *Nucl. Phys. A*, 533(1):132 – 152, 1991.

[204] S. Ćwiok, J. Dobaczewski, P.-H. Heenen, P. Magierski, and W. Nazarewicz. Shell structure of the superheavy elements. *Nucl. Phys. A*, 611:211 – 246, 1996.

[205] P. Möller and J.R̃. Nix. Stability of heavy and superheavy elements. *J. Phys. G*, 20:1681, 1994.

[206] K. Rutz, M. Bender, T. Bürvenich, T. Schilling, P.-G. Reinhard, J. A. Maruhn, and W. Greiner. Superheavy nuclei in self-consistent nuclear calculations. *Phys. Rev. C*, 56:238–243, Jul 1997.

[207] M. Bender, K. Rutz, P.-G. Reinhard, J. A. Maruhn, and W. Greiner. Shell structure of superheavy nuclei in self-consistent mean-field models. *Phys. Rev. C*, 60:034304, 1999.

[208] W. Zhang, J. Meng, S.Q. Zhang, L.S. Geng, and H. Toki. Magic numbers for superheavy nuclei in relativistic continuum hartree–bogoliubov theory. *Nucl. Phys. A*, 753(1–2):106 – 135, 2005.

[209] R. D. Herzberg and P. T. Greenlees. In-beam and decay spectroscopy of transfermium nuclei. *Prog. Part. Nucl. Phys.*, 61:674, 2008.

[210] T. Nikšić, N. Paar, D. Vretenar, and P. Ring. Dirhb - a relativistic self-consistent mean-field framework for atomic nuclei. *Comp. Phys. Comm.*, 185(6):1808 – 1821, 2014.

[211] J. J. Li, W. H. Long, J. Margueron, and N. V. Giai. Superheavy magic structures in the relativistic hartree-fock-bogoliubov approach. *Physics Letters B*, 732(0):169, 2014.

[212] M. Bender, W. Nazarewicz, and P.-G. Reinhard. Shell stabilization of super- and hyperheavy nuclei without magic gaps. *Phys. Lett. B*, 515(1–2):42 – 48, 2001.

[213] V. M. Strutinsky. Influence of nucleon shells on energy of a nucleus. *Yad. Fiz.*, 3:614–625, 1966.

[214] V. M. Strutinsky. Shell effects in nuclear masses and deformation energies. *Nucl. Phys. A*, 95(2):420 – 442, 1967.

[215] V. M. Strutinsky. Shells in deformed nuclei. *Nucl. Phys. A*, 122(1):1 – 33, 1968.

[216] S. G. Nilsson and I. Ragnarsson. Shapes and shells in nuclear structure. *Shapes and shells in nuclear structure, (Cambridge University Press, 1995).*

[217] Jr. V. E. Viola and G. T. Seaborg. *J. Inorg. Nucl. Chem.*, 28:741, 1966.

[218] T. Dong and Z. Ren. New calculations of -decay half-lives by the viola-seaborg formula. *Eur. Phys. J.*, A26:69 – 72, 2005.

[219] X. Bao, H. Zhang, H. Zhang, G. Royer, and J. Li. Systematical calculation of α-decay half-lives with a generalized liquid drop model. *Nucl. Phys. A*, 921:85–95, 2014.

[220] W. Nazarewicz, P.-G. Reinhard, W. Satula, and D. Vretenar. Symmetry energy in nuclear density functional theory. *Eur. Phys. J. A*, 50:20, 2014.

[221] J.M̃. Pearson, N. Chamel, A.F̃. Fantina, and S. Goriely. Symmetry energy: nuclear masses and neutron stars. *Eur. Phys. J.*, A50:43, 2014.

[222] J. Piekarewicz. Symmetry energy constraints from giant resonances: a relativistic mean-field theory overview. *Eur. Phys. J.*, A50:25, 2014.

[223] G. Colo, U. Gard, and H. Sagawa. Symmetry energy from the nuclear collective motion: constraints from dipole, quadrupole, monopole and spin-dipole resonances. *Eur. Phys. J.*, A50:20, 2014.

[224] C.J̃. Horowitz, K.S̃. Kumar, and R. Michaels. Electroweak measurements of neutron densities in crex and prex at jlab, usa. *Eur. Phys. J.*, A50:48, 2014.

[225] M. Dutra, O. Lourenco, and D.P̃. Menezes. Stellar properties and nuclear matter constraints. *Phys. Rev. C*, 93:025806, 2016.

[226] P. B. Demorest, T. Pennucci, S. M. Ransom, M. S. E. Roberts, and J. W. T. Hessels. *Nature*, 467:1081, 2010.

[227] John Antoniadis, Paulo C. C. Freire, Norbert Wex, Thomas M. Tauris, Ryan S. Lynch, Marten H. van Kerkwijk, Michael Kramer, Cees Bassa, Vik S. Dhillon, Thomas Driebe, Jason W. T. Hessels, Victoria M. Kaspi, Vladislav I. Kondratiev, Norbert Langer, Thomas R. Marsh, Maura A. McLaughlin, Timothy T. Pennucci, Scott M. Ransom, Ingrid H. Stairs, Joeri van Leeuwen, Joris P. W. Verbiest, and David G. Whelan. A massive pulsar in a compact relativistic binary. 340(6131):448, 2013.

[228] D. Chatterjee and I. Vidaña. Do hyperons exist in the interior of neutron stars? *Eur. Phys. J.*, A52:29, 2016.

[229] K. Q. Lu, Z. X. Li, Z. P. Li, J. M. Yao, and J. Meng. Global study of beyond-mean-field correlation energies in covariant energy density functional theory using a collective hamiltonian method. *Phys. Rev. C*, 91:027304, 2015.

[230] A. Akmal, V. R. Pandharipande, and D. G. Ravenhall. Equation of state of nucleon matter and neutron star structure. *Phys. Rev. C*, 58:1804–1828, Sep 1998.

[231] Z. H. Li and H.-J. Schulze. Neutron star structure with modern nucleonic three-body forces. *Phys. Rev. C*, 78:028801, Aug 2008.

[232] P.-G. Reinhard and W. Nazarewicz. Nuclear charge and neutron radii and nuclear matter: trend analysis. *arXiv: nucl-th/1601.06324v1*, 2016.

[233] F. J. Fattoyev and J. Piekarewicz. Accurate calibration of relativistic mean-field models: Correlating observables and providing meaningful theoretical uncertainties. *Phys. Rev. C*, 84:064302, 2011.

[234] X. Roca-Maza, N. Paar, and G. Colò. Covariance analysis for energy density functionals and instabilities. *J. Phys. G*, 42(3):034033, 2015.

[235] J. Piekarewicz, B. K. Agrawal, G. Colò, W. Nazarewicz, N. Paar, P.-G. Reinhard, X. Roca-Maza, and D. Vretenar. Electric dipole polarizability and the neutron skin. *Phys. Rev. C*, 85:041302, Apr 2012.

[236] S. E. Agbemava, A. V. Afanasjev, D. Ray, and P. Ring. Assessing theoretical uncertainties in fission barriers of superheavy nuclei. *Phys. Rev. C*, 95:054324, May 2017.

[237] Jie Meng, Jing Peng, Shuang-Quan Zhang, and Peng-Wei Zhao. Progress on tilted axis cranking covariant density functional theory for nuclear magnetic and antimagnetic rotation. *Front. Phys.*, 8:55–79, 2013.

[238] J. Dechargé, J.-F. Berger, K. Dietrich, and M.S. Weiss. Superheavy and hyperheavy nuclei in the form of bubbles or semi-bubbles. *Phys. Lett. B*, 451(3–4):275 – 282, 1999.

[239] J.F̃. Berger, L. Bitaud, J. Decharg'e, M. Girod, and K. Dietrich. Superheavy, hyperheavy and bubble nuclei. *Nucl. Phys. A*, 685:1c, 2001.

[240] W. Brodziński and J. Skalski. Predictions for superheavy elements beyond $z = 126$. *Phys. Rev. C*, 88:044307, Oct 2013.

[241] Y. K. Gambhir, A. Bhagwat, and M. Gupta. The highest limiting z in the extended periodic table. *J. Phys. G*, 42(12):125105, 2015.

[242] K. Dietrich and K. Pomorski. Stability of bubble nuclei through shell effects. *Phys. Rev. Lett.*, 80:37–40, 1998.

[243] V. Yu. Denisov. Magic numbers of ultraheavy nuclei. *Phys. At. Nuclei*, 68:1133, 2005.

[244] M. Ismail, A. Y. Ellithi, A. Adel, and H. Anwer. On magic numbers for super- and ultraheavy systems and hypothetical spherical double-magic nuclei. *J. Phys. G*, 43:015101, 2016.

[245] M. Warda. Toroidal structure of super-heavy nuclei in the hfb theory. *Int. J. Mod. Phys. E*, 16:452, 2007.

[246] A. Staszczak and C. Y. Wong. Toroidal super-heavy nuclei in skyrme hartree-fock approach. *Acta Phys. Pol.*, 40:753, 2009.

[247] B. Fricke, W. Greiner, and J. T. Waber. The continuation of the periodic table up to z = 172. the chemistry of superheavy elements. *Theor. Chim. Acta*, 21:235, 1971.

[248] P. Pyykko. A suggested periodic table up to $z < 172$, based on dirac-fock calculations on atoms and ions. *Phys. Chem. Chem. Phys.*, 13:161–168, 2011.

[249] P. Indelicato, J. Biero, and P. Jansson. Are mcdf calculations 101% correct in the super-heavy elements range?. *Theor. Chem. Acc.*, 129:495 – 505, 2011.

[250] B.-N. Lu, E.-G. Zhao, and S.-G. Zhou. Potential energy surfaces of actinide nuclei from a multidimensional constrained covariant density functional theory: Barrier heights and saddle point shapes. *Phys. Rev. C*, 85:011301, 2012.

[251] A. V. Afanasjev and S. E. Agbemava. Covariant energy density functionals: Nuclear matter constraints and global ground state properties. *Phys. Rev. C*, 93:054310, 2016.

[252] A. V. Afanasjev and S. Frauendorf. Central depression in nuclear density and its consequences for the shell structure of superheavy nuclei. *Phys. Rev. C*, 71:024308, Feb 2005.

[253] Andrzej Staszczak and Cheuk-Yin Wong. A region of high-spin toroidal isomers. *Physics Letters B*, 738(Supplement C):401 – 404, 2014.

[254] T. Ichikawa, K. Matsuyanagi, J. A. Maruhn, and N. Itagaki. High-spin torus isomers and their precession motions. *Phys. Rev. C*, 90:034314, Sep 2014.

[255] A. Kosior, A. Staszczak, and C.-Y. Wong. Toroidal nuclear matter distributions of superheavy nuclei from constrained skyrme–hfb calculations. *Acta Phys. Pol.*, 10:249, 2017.

[256] S. Cwiok-P. H. Heenen A. T. Kruppa P.-G. Reinhard W. Nazarewicz, M. Bender and T. Vertse. Theoretical description of superheavy elements. *Nucl. Phys. A*, 701:165c, 2002.

[257] A. Staszczak, Cheuk-Yin Wong, and A. Kosior. Toroidal high-spin isomers in the nucleus $^{304}120$. *Phys. Rev. C*, 95:054315, May 2017.

[258] A. V. Afanasjev, D. B. Fossan, G. J. Lane, and I. Ragnarsson. Termination of rotational bands: Disappearance of quantum many-body collectivity. *Phys. Rep.*, 322:1, 1999.

[259] M. Warda, J. L. Egido, L. M. Robledo, and K. Pomorski. Self-consistent calculations of fission barriers in the fm region. *Phys. Rev. C*, 66:014310, Jul 2002.

[260] A. Staszczak, A. Baran, J. Dobaczewski, and W. Nazarewicz. Microscopic description of complex nuclear decay: Multimodal fission. *Phys. Rev. C*, 80:014309, Jul 2009.

[261] N. Schunck and L. M. Robledo. Microscopic theory of nuclear fission: A review. *Rep. Prog. Phys.*, 79:116301, 2016.

[262] N. T. B. Stone, O. Bjarki, E. E. Gualtieri, S. A. Hannuschke, R. Lacey, J. Lauret, W. J. Llope, D. J. Magestro, R. Pak, A. M. Vander Molen, G. D. Westfall, and J. Yee. Evidence for the decay of nuclear matter toroidal geometries in nucleus-nucleus collisions. *Phys. Rev. Lett.*, 78:2084–2087, Mar 1997.

[263] C.Y Wong. Toroidal and spherical bubble nuclei. *Annals of Physics*, 77(1):279 – 353, 1973.

[264] B. P. Abbott et al. Gw170817: Observation of gravitational waves from a binary neutron star inspiral. *Phys. Rev. Lett.*, 119:161101, 2017.

[265] D. N. Poenaru, R. A. Gherghescu, and W. Greiner. Heavy-particle radioactivity of superheavy nuclei. *Phys. Rev. Lett.*, 107:062503, Aug 2011.

[266] D. N. Poenaru, R. A. Gherghescu, and W. Greiner. Cluster decay of superheavy nuclei. *Phys. Rev. C*, 85:034615, Mar 2012.

[267] T. Marketin, L. Huther, and G. Martínez-Pinedo. Large-scale evaluation of β-decay rates of r-process nuclei with the inclusion of first-forbidden transitions. *Phys. Rev. C*, 93:025805, 2016.

[268] T. Shafer, J. Engel, C. Fröhlich, G. C. McLaughlin, M. Mumpower, and R. Surman. β decay of deformed r-process nuclei near $a = 80$ and $a = 160$, including odd-a and odd-odd nuclei, with the skyrme finite-amplitude method. *Phys. Rev. C*, 94:055802, Nov 2016.

[269] I. Angeli. A consistent set of nuclear rms charge radii: properties of the radius surface r(n,z). *Atomic Data and Nuclear Data Tables*, 87(2):185 – 206, 2004.